SIMULATION OF ISOTHERMAL COMBUSTION IN GAS TURBINES

by

Matthew Rice

Thesis submitted to the faculty of the Virginia Polytechnic Institute and State University
in partial fulfillment of the requirements for the degree of

Masters of Sciences
in
Mechanical Engineering

Dr. Peter King, Committee Chairman
Dr. Clint Dancey, Committee Member
Dr. Uri Vandsburger, Committee Member

February 12th, 2004
Blacksburg, Virginia

Keywords: Turbines, Isothermal, Combustion, High-efficiency, Turbine Simulations

Abstract

SIMULATION OF ISOTHERMAL COMBUSTION IN GAS TURBINES

by
Matthew J. Rice
Committee Chair: Dr. Peter King
Dr. Clint Dancey
Dr. Uri Vandsburger

Current improvements in gas turbine engine performance have arisen primarily due to increases in turbine inlet temperature and compressor pressure ratios. However, a maximum possible turbine inlet temperature exits in the form of the adiabatic combustion temperature of the fuel. In addition, thermal limits of turbine blade materials also places an upper bound on turbine inlet temperatures. Thus, the current strategy for improving gas turbine efficiency is inherently limited. Introduction of a new gas turbine, based on an alternative work cycle utilizing isothermal combustion (i.e. combustion within the turbine) affords significant opportunities for improving engine output and/or efficiency. However, implementation of such a scheme presents a number of technological challenges such as holding a flame in high-speed flow. The currect research is aimed at determining whether such a combustion scheme is feasible using computational methods. The geometry, a simple 2-D cascade utilizes surface injection within the stator or rotor boundary layers (including the rotor pressure side recirculation zone (a natural flame holder)). Computational methods utilized both steady and time accurate calculations with transitional flow as well as laminar and turbulent combustion and species transport. It has been determined that burning within a turbine is possible given a variety of injection schemes using "typical" foil geometries under "typical" operating conditions. Specifically, results indicate that combustion is self-igniting and, hence, self-sustaining given the high temperatures and pressures within a high pressure turbine passage. Deterioration of aerodynamic performance is not pronounced regardless of injection scheme. However, increased thermal loading in the form of higher adiabatic surface temperatures or heat transfer is significant given the injection and burning of the fuel within the boundary layer. This increase in thermal loading is, however, minimized when injection takes place in or near a recirculation zone. The effect of injection location on pattern factors indicates that suction side injection minimizes temperature variation downstream of the injection surface (for rotor injection only). In addition, the most uniform temperature profile (in the flow direction) is achieved by injection of fuel and combustion nearest to the source of work extraction. Namely, injection at the rotor produces the most "isothermal" temperature distribution. Finally, a *pseudo direct* simulation of an isothermal machine is conducted by combining simulation data and assumed processes. The results indicate that isothermal combustion results in an increase in turbine specific work and efficiency over the *equivalent* Brayton cycle.

Acknowledgements
I would like to express graditude to my graduate committee: Dr. Peter King, Dr. Clint Dancey and Dr. Uri Vandsburger for their feedback. I also wish to thank Steve Greenfield and Dr. Jan Bøhn for supplying the computing facilities and computing hardware. The Virginia Tech community is also deserving of my gratitude for providing the opportunity to continue my education after a previously "turbulent" graduate school experience. Much appreciation also goes to those "down" in the turbolab for their steady presence. Finally, I wish to express my deepest love for those back home in"little ole" Portland whose support made my success in these last few years possible.

Published in glorious LaTeX

Contents

List of Figures

List of Tables

Chapter 1

INTRODUCTION AND MOTIVATION

1.1 INTRODUCTION AND HISTORICAL BACKGROUND

The need for continual improvements in gas turbine efficiency and power is the driving force behind current engine development. Indeed, the evolution of the gas turbine engine

Figure 1.1: Lockheed Tristar L-1011

used in aerospace applications can be described as a sucession of technological "break-throughs" resulting in enhanced thermal efficiency and power. The principle (historical) advances in gas turbine technology were the development of high-bypass ratio turbofan engines (in the 1960's) and external/internal turbine blade cooling (in the 1960's and 70's). Figure 1.1 shows one of the first civilian aircraft to use high-bypass engines supplied by Rolls-Royce (Figure 1.2). In addition to improvements in efficiency, of concern to engine manufacturers is the power produced (in the form of shaft power and/or thrust) in comparison to engine size. While this comparison is especially important for military

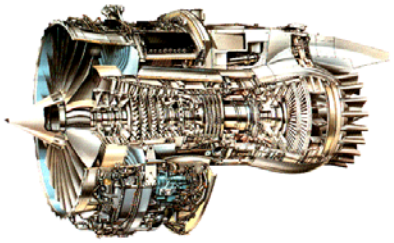

Figure 1.2: Roll-Royce RB-211 Turbofan Engine

applications (which require significant thrust for rapid acceleration along with low engine weight), civilian applications also require (in some cases) significant production of thrust if only for brief periods. A specific technology used to enhance thrust production is the

Figure 1.3: Concord at takeoff

technique known as "afterburning" used extensively for military aircraft and, to a much lesser extent, in civil aviation. The use of this technology has significant drawbacks in terms of reduced efficiency and an increase in thrust specific fuel consumption (TSFC). Figure 1.3 shows the Concord at takeoff (note the use of afterburners) which utilizes the Olympus turbojet supplied by Rolls-Royce (Figure 1.4).[1]

With the exception of performance improvements arising from the use of turbofan (as opposed to turbojet) configuations, the "recent" history of jet engine development has been dictated by much more fundamental and rudimentry cycle analysis. Specifically, enhanced power and engine efficiency can, and has been brought about by raising turbine inlet temperatures. The end result (historically) is a constant upward trend in turbine inlet temperatures and compressor pressure ratios in order to enhance the cycle efficiency and power of modern Brayton cycle gas turbine engines. This trend is readily observed

[1]High fuel consumption was the primary reason for the Concord's lack of commercial viability.

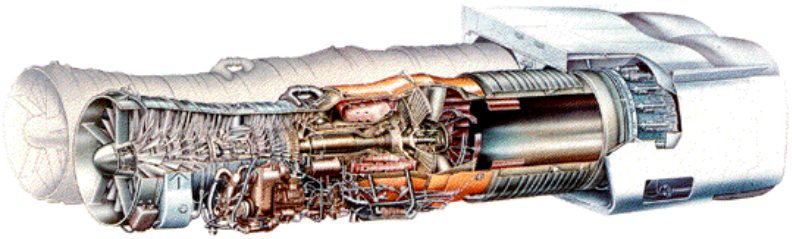

Figure 1.4: Roll-Royce Olympus

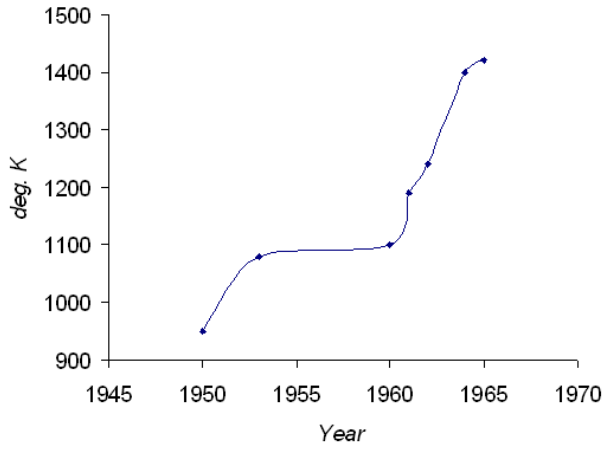

Figure 1.5: Temperature vs. year

in Figure 1.5 and Figure 1.6 which display turbine inlet temperatures vs. production date (for various Rolls-Royce engines) and cruise specific thrust-to-weight ratio vs. turbine inlet temperature for various turbojet engines. As Figure 1.5 indicates, the upward trend in peak engine temperatures is gradual throughout the 1950's whereupon the introduction of turbine blade cooling and advances in materials technology allowed for a more rapid increase in turbine inlet temperature. Finally, Figure 1.7 illustrates the historical trend in (cruise) thrust specific fuel consumption as a result of engine improvements including, amongst others, an increase in peak engine temperature (i.e. turbine inlet temperature). It should be borne in mind that turbine inlet temperatures cannot be raised indefinitely. Apart from the issue of turbine component durability, there exists a temperature limit in the form of the adiabatic flame temperature (for a given combustor inlet temperature), which the turbine inlet gases cannot exceed. For current aviation fuels this limit is in *excess* of $2,300^{\circ}K$. Hence, as peak engine temperatures approach this limit an alternative

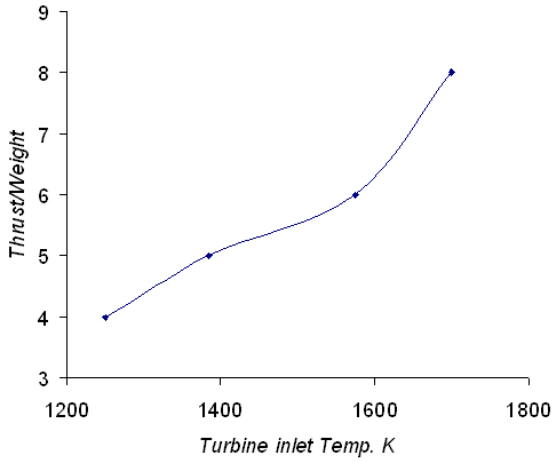

Figure 1.6: Thrust to weight vs. inlet temperature

strategy must be found for increasing engine efficiency without reducing power. Such an alternative potentially exits with the introduction of a new cycle and its hybrid counterpart in the form of isothermal heat addition within the turbine itself, (as opposed to the combustor alone (which is the case for all modern Brayton cycle engines currently used today)). To see this we first take a brief detour into the basic thermodynamics governing the Brayton work cycle.

1.2 IDEAL BRAYTON CYCLE

[2] The idealized Brayton cycle (for which all modern gas turbine engines are based) is illustrated in Figure 1.8 and composed of the following internally reversible processes:

1. Isentropic compression (in compressor), $(1 \rightarrow 2)$
2. Isobaric heat addition (in combustor), $(2 \rightarrow 3)$
3. Isentropic expansion (in turbine), $(3 \rightarrow 4)$
4. Isobaric heat rejection (to the ambient), $(4 \rightarrow 1)$

From a rather straight-forward cycle analysis assuming idealized processes for a perfect gas, we have the following expression for the thermal efficiency of the Brayton work cycle

$$\eta_{Brayton} = 1 - \tau_c^{-1} = 1 - \pi^{1-\gamma/\gamma} \tag{1.1}$$

[2]The following development in section 1.2-3 resembles that in Ramohalli, AIAA-87-1999

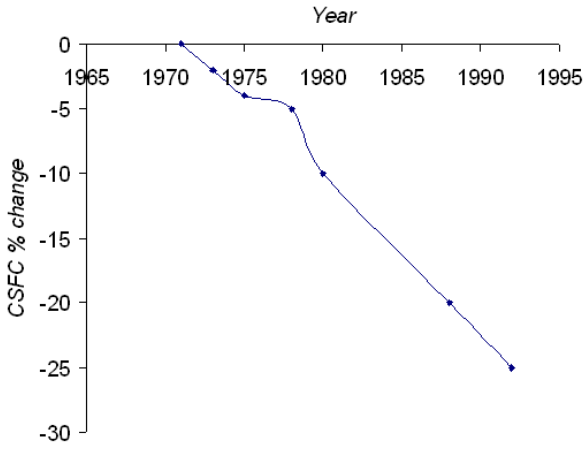

Figure 1.7: Thrust specific fuel consumption vs. production year

where τ_c and π are the compressor temperature and pressure ratios respectively. In addition, specific work (scaled or dimensionless work per unit mass of the working fluid) is also given by

$$W^*_{Brayton} = \frac{W}{C_p T_{ambient}} = \tau_\lambda - \tau_c + 1 - \frac{\tau_\lambda}{\tau_c} \tag{1.2}$$

The maximum normalized specific work for a fixed overall temperature ratio ($T_{turbineinlet}/T_{ambient} = T_3/T_1 \equiv \tau_\lambda$) is also given by

$$W^\star_{max(Brayton)} \equiv \frac{W^{Brayton}_{max}}{C_p T_{ambient}} = \tau_\lambda - 2\sqrt{\tau_\lambda} + 1 = \left(\sqrt{\tau_\lambda} - 1\right)^2 \tag{1.3}$$

where we find that

$$\tau_c^{workmax} = \sqrt{\tau_\lambda} \tag{1.4}$$

This yields an expression for the maximum work thermal efficiency

$$\eta^{workmax}_{Brayton} = 1 - \frac{1}{\sqrt{\tau_\lambda}} \tag{1.5}$$

Thus, from (1.5) and (1.3) we can see that in order to maximize output *and* reduce fuel consumption (i.e. increase thermal efficiency while producing the most work possible per unit mass flow), turbine inlet temperatures must be as high as possible (hence, maximizing the value of τ_λ). Unfortunately, as stated previously, physical limitations for such a strategy which cannot be avoided are the maximum combustion temperature for the fuels currently used, and the thermal limits of turbine and combustor materials. In addition,

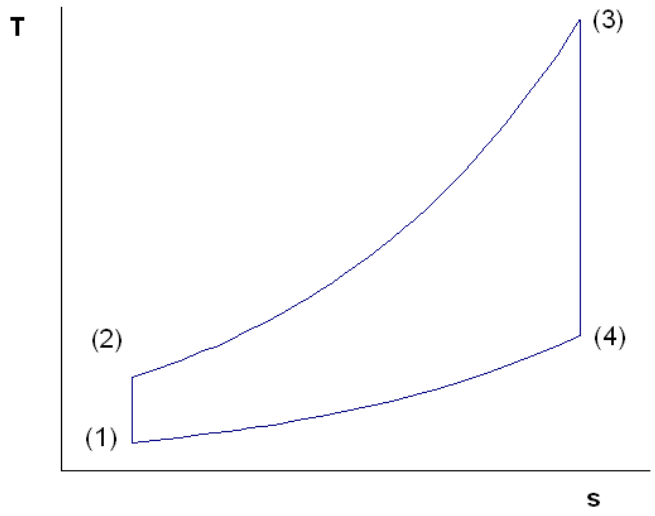

Figure 1.8: $T - s$ diagram for ideal Brayton cycle

while increasing compressor pressure ratios results in an increase in efficiency, specific output (or work per unit mass) ultimately falls as a result. Thus, to a significant extent, a tradeoff exists between engine power and efficiency for current machines based on the Brayton cycle.[3] It is in the hope of partially overcoming this tradeoff that a new, isothermal work cycle, could be implemented for use in gas turbines.

1.3 IDEAL ISOTHERMAL CYCLE

The Carnot cycle, composed of constant temperature (or isothermal) heat addition and rejection processes, is the most efficient work cycle. Hence, it makes sense to apply such a process, where possible, to gas turbines. Specifically, a new work cycle might be composed of the following processes as illustrated in Figure 1.9:

1. Isentropic compression (in compressor), $(1 \rightarrow 2' \rightarrow 2)$
2. Isothermal heat addition (combustion in turbine), $(2 \rightarrow 3)$
3. Isentropic expansion (work extraction in turbine), $(3 \rightarrow 4)$
4. Isobaric heat rejection (to ambient), $(4 \rightarrow 1)$

[3]For the maximum efficiency operating point $\tau_c \rightarrow \tau_\lambda$ and $\mathrm{W}^* \rightarrow 0$.

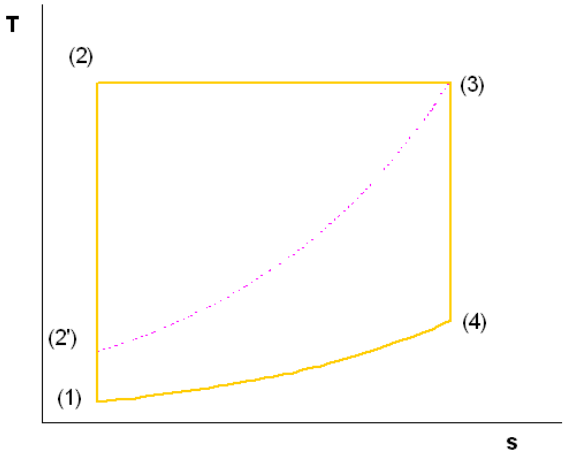

Figure 1.9: $T - s$ diagram for ideal isothermal cycle

Note that a distinct combustor (as used in the case of a Brayton cycle machine) is absent from the isothermal cycle. Instead, fuel is injected and combustion occurs at the location of work extraction (i.e. in the turbine), thus maintaining a constant gas flow temperature. Assuming an ideal isothermal process as shown in Figure 1.9 we find the efficiency for our new cycle to be

$$\eta_{isothermal} = 1 - \frac{(\tau_c^{-1} - \tau_\lambda^{-1})}{ln(\tau_\lambda/\tau_c)} \tag{1.6}$$

where $\tau_c \equiv T_{2'}/T_1$ (according to Figure 1.9). Now, assuming typical temperatures associated with conventional Brayton cycle engines we have $\tau_\lambda/\tau_c = T_3/T_{2'} \approx 2.5$. Thus, the isothermal thermal efficiency can be approximated as

$$\eta_{isothermal} \approx 1 - \tau_c^{-1} + \tau_\lambda^{-1} = \eta_{Brayton} + \tau_\lambda^{-1} \tag{1.7}$$

Hence, for *typical* jet engine operating conditions (in fact, for all conditions conforming to the cycle in Figure 1.9) the isothermal thermal efficiency is higher that that of the Brayton cycle. In addition, we can express the normalized work (again, scaled work per unit mass flow) for the isothermal cycle as

$$W^*_{isothermal} \equiv \frac{W_{isothermal}}{C_p T_{ambient}} = 1 + \tau_\lambda ln(\tau_\lambda/\tau_c) - \tau_\lambda/\tau_c \tag{1.8}$$

Similarly, normalized work for the isothermal process is maximized when

$$\tau_c = T_{2'}/T_1 = 1 \rightarrow W^{max}_{isothermal} \tag{1.9}$$

which is hardly surprising given that net work per unit mass flow is the area bound by the T-s curve. In contrast, for maximum efficiency we have

$$T_{2'} = T_3 \rightarrow \tau_\lambda = \tau_c \tag{1.10}$$

which (from the figure) minimizes heat rejection per unit heat addition. Note that like the

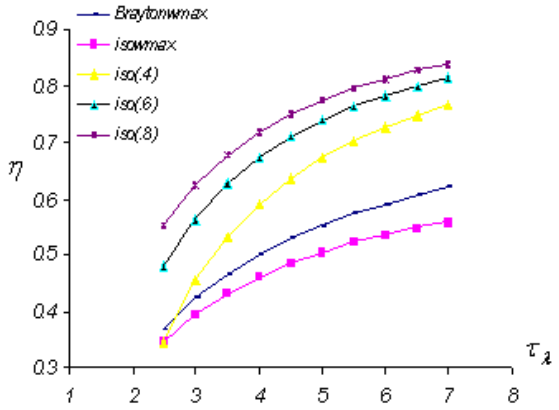

Figure 1.10: η vs τ_λ for Isothermal and Brayton cycle

conventional Brayton cycle, output is zero for the maximum efficiency operating point.

1.4 PERFORMANCE COMPARISONS FOR THE ISOTHERMAL AND BRAYTON CYCLES

Comparing cycle efficiency and specific output for the maximum work Brayton as a function of peak (or turbine inlet) temperature we find that the isothermal cycle performance is superior for almost all operating points. Specifically, Figure 1.10 displays isothermal and Brayton cycle efficiency for various values of the temperature ratio $\tau_c/\tau_\lambda = T_{2'}/T_3$ (in parenthesis) including the maximum work condition ($\tau_c = T_{2'}/T_1 = 1$) as a function of τ_λ. Note that Figure 1.10 indicates an improvement in cycle efficiency over the maximum work Brayton cycle except in the case of the operating points corresponding to the maximum work isothermal cycle. This efficiency penalty is rather small and ranges from 2% to 7% depending on turbine inlet temperature. If, however, we compare the *slight* reduction in cycle efficiency to the increase in work output for the maximum work Brayton and isothermal cycle (see Figure 1.11), we see an increase in specific output of 50% to

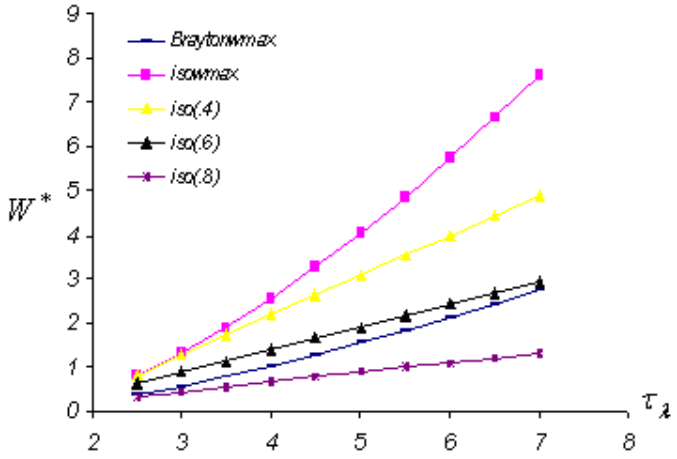

Figure 1.11: Normalized work vs. τ_λ for Isothermal and Brayton cycle

300% for the isothermal cycle (depending on turbine inlet temperature (proportional to τ_λ)). Hence, we conclude that, at the least, isothermal combustion results in a significant increase in engine power with only a modest decrease in efficiency. Conversely, if only a small increase in power is desired (over that of the conventional Brayton cycle), then isothermal combustion can result in a significant improvement in cycle efficiency.

1.5 HYBRID BRAYTON-ISOTHERMAL CYCLE

Unfortunately, to achieve the high output and efficiency associated with isothermal combustion very high compressor pressure ratios are required (see Figure 1.9 and note that the temperature rise $T_1 \rightarrow T_2$ is achieved solely through compression within the compressor (as opposed to compression followed by isobaric heat addition within a combustor as is the case for the Brayton cycle)). Such pressure ratios (on the order of 100 to 200/1) are not technologically feasible at present. The solution to this difficulty is to utilize a combustor with subsequent isothermal heat addition (burning within the turbine) yielding a hybrid isothermal-Brayton cycle. Such a cycle, depicted in Figure 1.12, is composed of the following processes

1. Isentropic compression, $(1 \rightarrow 2' \rightarrow 2)$
2. Isobaric heat addition (in combustor), $(2 \rightarrow 3)$
3. Isothermal heat addition (heat addition in turbine), $(3 \rightarrow 4)$

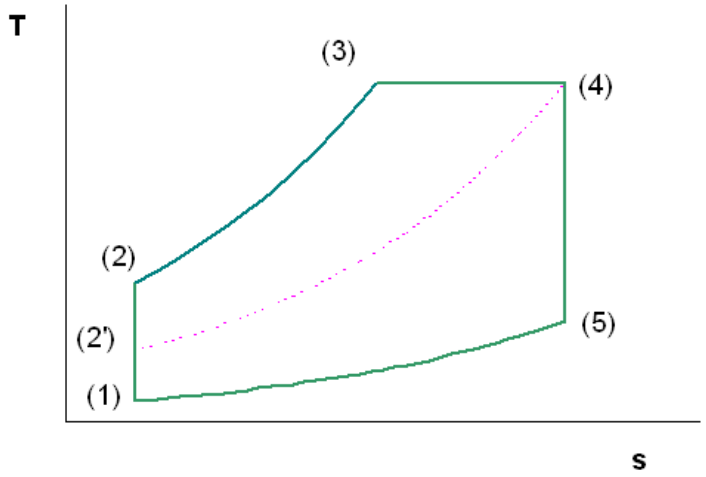

Figure 1.12: T-s diagram for hybrid isothermal-Brayton cycle

4. Isentropic expansion (work extraction in turbine (no combustion)), $(4 \rightarrow 5)$
5. Isobaric heat rejection (to the ambient), $(5 \rightarrow 1)$

This hybrid Brayton-isothermal cycle, while not as efficient as the pure isothermal cycle, still provides many advantages over the traditional Brayton machine in terms of increased output and/or enhanced thermal efficiency over a variety of operating conditions. The expression for the thermal efficiency for this hybrid cycle is[4]

$$\eta_{Hybrid} = 1 - \frac{\tau_\lambda/\tau_{c'} - 1}{\tau_\lambda - \tau_c - \tau_\lambda ln(\tau_{c'}/\tau_c)} \tag{1.11}$$

again where τ_c, $\tau_{c'}$ and τ_λ are defined as T_2/T_1, $T_{2'}/T_1$ and T_3/T_1. As in the case of the ideal Brayton and Isothermal cycle a normalized work can also be calculated.

$$W^*_{Hybrid} = 1 - \tau_c + \tau_\lambda(1 - \frac{1}{\tau_{c'}} - ln\frac{\tau_{c'}}{\tau_c}) \tag{1.12}$$

Hence, a comparison can now be made between the Brayton and Hybrid cycle. Figures 1.13 and 1.14 compare thermal efficiency and normalized work for the Hybrid and Brayton cycle assuming *reasonable* values for τ_c and $\tau_c^{'}$.[5] Specifically, from Figure 1.13 we see that the Hybrid (or combined) cycle (in blue) presents an efficiency advantage over the Brayton cycle (in yellow) *over all* temperature ratios τ_λ. Figure 1.14 also illustrates the

[4] See Appendix A for details

[5] Assuming a conventional Brayton machine overall pressure ratio of 30/1 and a Hybrid device pressure ratio of 40/1 we find (for isentropic compression) $\tau_{c'}$ and τ_c are 2.59 and 2.809 respectively.

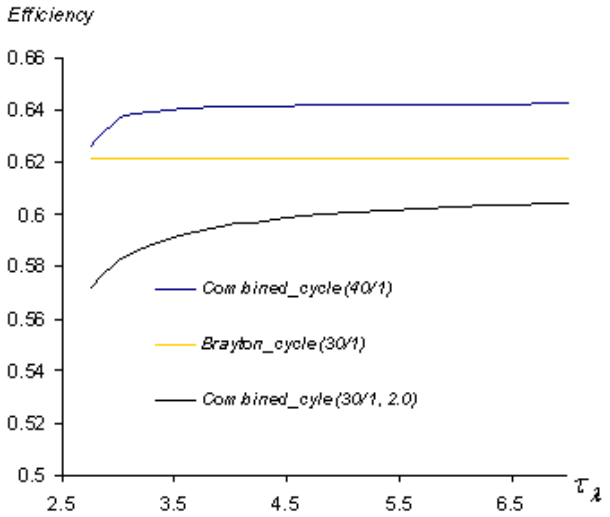

Figure 1.13: η vs. τ_λ for Hybrid (combined) and Brayton cycle

hybrid cycle advantage in net specific work over the Brayton cycle.[6] It should be noted that these results are only valid for the temperature ratios assumed, and in general, for an identical compressor and peak engine temperatures the Hybrid cycle must produce more work (but, may not be more efficient). Indeed the latter point is illustrated by comparing the combined cycle with the same compressor pressure ratio as the Brayton cycle. This combined cycle has a cutoff temperature ratio $\tau_{c'}$ of 2.0 and, while producing more work than the Brayton cycle, exhibits a lower efficiency.

Instead of plotting specific work and efficiency as a function of τ_λ we might instead be interested in holding the peak engine temperature, compressor pressure ratio for the Brayton machine and the cut-off pressure constant (i.e. holding T_3 and $T_{2'}$ constant). These results are given in Figure 1.15 and indicate that the Hybrid cycle always has superior performance in terms of enhanced output and efficiency.[7] In conclusion, we must be careful how we characterize the potential benefits of isothermal combustion. Specifically, isothermal combustion as used in the Hybrid cycle is only guaranteed to yield improved efficiency*and* output for compressor pressure ratios in excess of the equivalent Brayton machine with the same peak engine temperature.

[6] Note the following notation "Conbined_cycle(30/1,2.0)" refers to a compressor pressure ratio of 30/1 and value of 2.0 for $\tau_{c'}$.

[7] These plots assume *reasonable* values for $\tau_{c'}$ and τ_λ of 2.76 and 6.5 respectively (but this result is general).

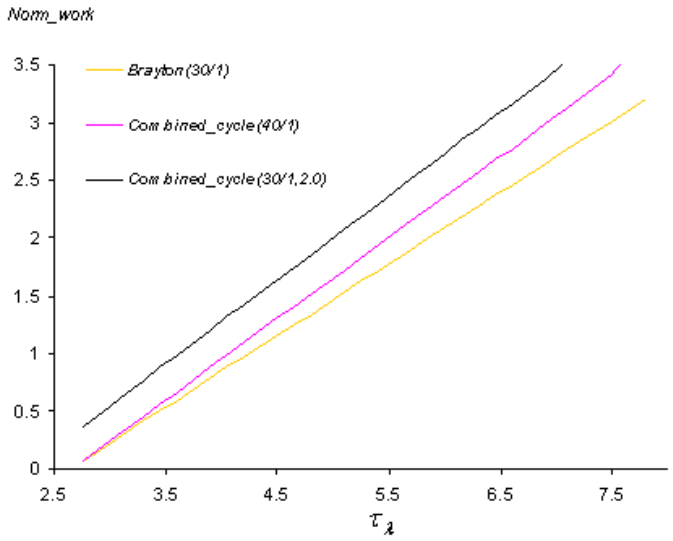

Figure 1.14: Normalized work vs. τ_λ for Hybrid (combined) and Brayton cycle

In subsequent chapters we shall demonstrate some of these results using a *pseudo-direct* simulation of a Hybrid and Brayton machine.

1.6 TOPICS OF INQUIRY AND THESIS FORMAT

1.6.1 TOPICS OF INQUIRY

Thus far, no information has been presented which relates to actual combustion inside a turbine nor the real benefits associated thereof. As indicated in the next chapter research into this topic has been limited and confined to several areas:

1. Simple cycle analysis comparing Brayton and Isothermal efficiency and power (no treatment has been found of a Hybrid cycle as such)

2. Experimental results for porous plate injection none of which were conducted at pressures *and* temperatures associated with the interior of a gas turbine

3. Computational experiments for combustors and stabilized flames, but few results for boundary layer injection of jet fuels under conditions similar to those existing in gas turbines

Hence, this thesis attempts to extend, using available computational tools, the range of inquiry into the feasibility of boundary layer and recirculation zone combustion for

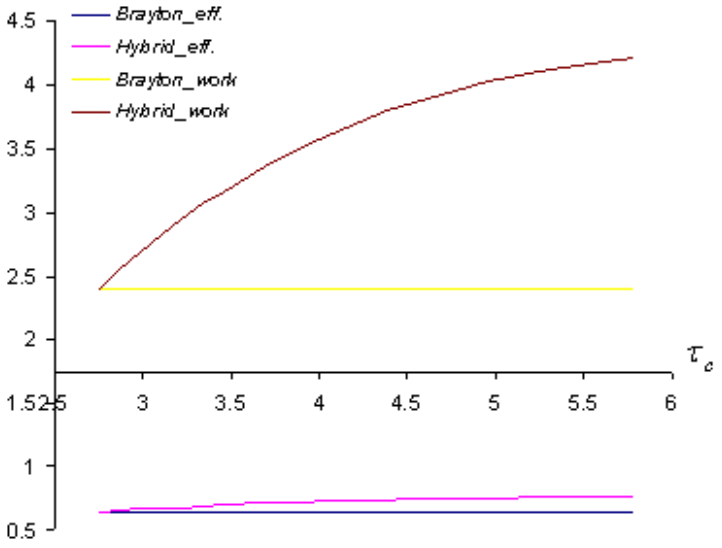

Figure 1.15: Normalize work and η vs. τ_c for Hybrid and Brayton cycle

conditions specific to gas turbines. Specifically, flow inside a turbine with first be modeled afterwhich the following questions will be addressed:

1. Using all computational tools at our disposal (via the computational package FLUENT), can we demonstrate the feasiblity of combustion within a gas turbine passage under *typical* conditions?

2. If combustion appears to be possible, which combustion scheme is the most desirable from an engineering standpoint. In other words

   Does injection location affect aerodynamic performance of the turbine airfoils?

   Does injection location affect blade heat transfer in magnitude and distribution?

   How does injection location affect pattern factors (transverse temperature variations just downstream of the foil trailing edge)?

   How does injection location (rotor or stator injection) affect the engine temperature distribution (i.e. which scheme produces the most "isothermal" temperature distribution)?

   Does isothermal combustion indeed result in any of the performance improvements promised?

1.6.2 THESIS FORMAT

Given that this research is computatonal in nature a heavy emphasis will be placed on providing an "in depth" review of the theoretical underpinnings as well as detailed descriptions of the solution procedure. Specifically, organization of the material will be as follows:

1. Present background into the desirability and motivation for investigation of isothermal combustion
2. Review the progress previously made and justify the need for further inquiry
3. Carefully illustrate the development of a computational model for the simulated phenomena (reacting flow inside a gas turbine-like environment)
4. Review simulation results and answer the questions stated previously

In addition, several *Appendices* are provided for conciseness and efficiency where needed.

Chapter 2

REVIEW OF THE LITERATURE

2.1 ISOTHERMAL COMBUSTION

The potential benefits of isothermal combustion are illustrated in the works of Ramohalli [3], Liu and Sirignano [4] and Sirignano, Delplanque and Liu [5]. Ramohalli, the first of the above to illustrate the benefits of isothermal combustion, compared thermal efficiencies and specific (or normalized work) for both the idealized and "real" isothermal and Brayton cycles. Assuming *typical* compressor exit temperatures, Ramohalli showed that the isothermal efficiency advantage over the Brayton cycle is proportional to the ambient temperature and inversely proportional to the peak engine temperature. In addition, he found that the isothermal cycle maximum specific work was substantially higher than that of the maximum work Brayton cycle with only a modest decrease in efficiency. Specifically, for the maximum specific work operating conditions for both cycles, (assuming an overall temperature ratio of 5), the ideal isothermal engine will produce *three times* the normalized work of the equivalent Brayton machine operating between the same temperature limits, while suffering a reduction in thermal efficiency of approximately 10%. Ramohalli points out, however, that to achieve the necessary high turbine inlet temperatures, compressor pressure ratios on the order of 100 to 1 would be required which is unattainable using current technology. The Author also notes an inherent advantage of the isothermal cycle for high flight Mach numbers.[1] Finally, Ramohalli also finds (using order of magnitude analysis) that the chemical and flow residence times are of the same maginitude (for droplet combustion in a turbine like environment). Thus, yielding inconclusive results as to the possibility of burning within a turbine. Liu and Sirignano investigated the performance

[1]Indeed, under such conditions the local compressor inlet temperature can be quite high, hence (for a constant compressor pressure ratio) increasing combustor inlet temperatures for the traditional Brayton cycle. This, given a maximum combustor outlet temperature necessitates a reduction the fuel burn rate (and hence work extraction).

benefits of interturbine burning as an alternative to afterburners and notes the enhanced efficiency associated with the former. The Authors also find that the isothermal device achieves a peak thrust efficiency at a higher bypass ratio than the conventional Brayton machine.

As in the case of Ramohalli, Liu and Sirignano find that turbine interburning results in improvements in efficiency and/or output (manifested in lower $TSFC$ (thrust-specfic-fuel-consumption)) over the conventional Brayton cycle. Specifically, for pressure ratios in the range $30 - 40/1$ performance of the conventional Brayton cycle machine deteriorates in terms of ST (specific thrust), while the isothermal device exhibits performance improvements for pressure ratios in excess of $60/1$. Sirignano, Delplanque and Liu repeat the analysis of the two previous studies, but also extends it to land-based regenerative gas turbines and finds that isothermal combustion yields superior specific power and/or thermal efficiency over the conventional Brayton cycle utilizing reheat. Finally, Andriani [2] using a simple one dimensional code (solving the governing *bulk* flow equations) finds that a two stage turbine utilizing interstage reheating, can produce specific thrust comparable to a conventional Brayton cycle engine with afterburner, while at the same time exhibiting thrust specific fuel consumption equivalent to the non-afterburning engine.

2.2 COMBUSTION IN HIGH SPEED FLOW

2.2.1 APPLICABLE EXPERIMENTAL RESULTS

Success of the isothermal scheme depends on the ability to light and sustain a flame in high speed flows present in turbine passages. Attemps have been made (both experimentally and computationally) to simulate combustion in a turbine passage-like environment. These attemps range from porous flat plate injection as in the case of Nasir [6], Agrawal [7] and Ramachandra [9] , to bluff body and step flame holders in high speed flow as in the case of Owens [10] and Schefer [11]. Specifically, Nasir experimentally simulated combustion within turbine passages using two parallel porous flat plates through which passed a heated air stream and found that combustion (of Methane) could be maintained for freestream velocities over $60m/s$. The airstream experienced precombustion corresponding to an equivalance ratio ϕ of 0.85 at atmospheric pressure yielding a freestream temperature of approximately $2000^{\circ}K$. Ramachandrea investigated the stabilization of a flame in a freestream using porous plate injection of Pentane. However, unlike the previous attempt, freestream temperatures were limited to $450^{\circ}K$. Ramachandra found an extinction freestream velocity of $3.5m/s$ and that "blowout" injection velocity increased with freestream oxygen content and decreased with fuel dilution. Rohmat, on the other hand, experimented with block and step flame holders placed upstream of a porous flat plate injection of methane and found the unsurprising result that flame holders (block or step) significantly increase flame stability. Like all previous experiments, this was also

conducted at atmospheric pressure (and a temperature of approximately $300^{\circ}K$) in the freestream. In addition, Lewis [19] found that the laminar flame speed is proportional to $g^{1/2}$ where g refers to the g-force experienced by the flow. In other words, the presence of swirl in the flow field has the effect of increasing the reaction rate. The presumed physical mechanism responsible for this effect is the migration of unburned fuel (of higher density than the surrounding products) due to centrifugal effects, thus exposing additional quantities of unburned fuel to the surrounding oxidizer (resulting in a faster burn rate). Zelina [18] conducted experiments using a high swirl combustor and found that the centrifugal force (applied to a burning element of fuel) indeed had the effect of increasing the effective reaction rate. These results, although not utilized in our study, are important given that the turbine environment is characterized by high swirl.

2.2.2 APPLICABLE COMPUTATIONAL RESULTS

Computational simulation of reacting high-speed swirling flows was conducted by Roy [12]. Specifically, Roy utilized an Eddy Dissipation model and PDF approach (in temperature) to simulated reacting flows past a bluff body. The turbulence model used was a $\kappa - \zeta$ (ζ is defined as the mean vorticity variance) and the use of global as well as a four-step reaction mechanism yielded accurate results (unlike the $\kappa - \epsilon$ turbulence model which is known to, and did perform poorly for separated flows). In addition, numerical simulations of more complex geometries such as full combustors have been conducted by Lee [15] and Xia [17] . Xia specifically compares the performance of two $\kappa - \epsilon$ turbulence models with a Reynolds stress formulation and finds the *familiar* deficiency in peformance of the former (compared with experimental results). The Author notes that many of the *interesting* features of the flow are not even qualitatively reproduced by the $\kappa - \epsilon$ model.[2] Lee, on the other hand, attempted to model combustion within a Pratt & Whitney gas turbine combustor (again) using a $\kappa - \epsilon$ turbulence model with reaction rates based on eddy-dissipation. Results were less than satisfactory with some of the overall qualitative characteristics of the flow not being predicted. Peak combustion temperatures were also incorrect (error on the order of 30%), however, some uncertainty as to the geometric configuration of the device may have been a factor.[3] A computational study was also conducted by Zelina [18] using the enhanced reaction rate of Lewis [19] (utilizing a $\kappa - \epsilon$ turbulence model with PDF species transport) and found the results to be in good agreement with experiment. However, it must be noted that the model used was specifically *tuned* to achieve this result.

[2] It should be stated that Xia's results are for "cold" incompressible flow (i.e. non-reacting).

[3] These results along with the *known* performance advantage posed by the $\kappa - \omega$ turbulence model for separated flows led to our choice of this model for the turbulence formulation.

2.3 OBSERVATIONS AND OPPORTUNITIES FOR INQUIRY

The previous studies, all of which approach (indirectly) the issue of combustion within a turbine, do not attempt to fully simulate conditions thereof. A simple cycle analysis demonstrating the theoretical improvements in engine output or efficiency due to isothermal combustion may not be realizable in real gas turbines. Likewise, order of magnitude analysis on chemical and flow times in a gas turbine-like environment lack specificity and yield inconclusive results as to the possibility of combustion. The experiments supposedly aimed directly at combustion in gas turbines are only loosely applicable given the fuels and operating conditions used. The same can also be said for the computational studies.

Hence, the opportunity exists for conducting computational experiments to determine whether isothermal combustion is clearly impossible in a "realistic" gas turbine. Specifically, we wish to address the following shortcomings in the literature:

1. Only simple cycle analysis comparing the Brayton and Isothermal cycle has been found (no treatment of the previously described Hybrid cycle has been presented to this Author's knowledge).

2. The experimental results for porous plate injection, although of interest, were not conducted at pressures *and* temperatures associated with the interior of a gas turbine.

3. Computational experiments for combustors and stabilized flames present few results for boundary layer injection of jet fuels under conditions similar to those existing in a gas turbine.

Indeed, in reference to (2) reaction rates and flame speeds are strong functions of the ambient temperature and relatively weak functions of pressure. Specifically, for most hydrocarbon fuels[4]

$$\text{laminar flame speed} \propto P^{-0.16}T^{2.18} \tag{2.1}$$

Hence, if possible, experiments should be conducted at the correct operating conditions.

It should however be stated that methods based on CFD are only as good as the modeling. Thus, strictly speaking, we seek only to ascertain whether combustion is *possible according to various models* for the flow as opposed to arriving at a definitive conclusion as to the possibility of boundary layer injection and combustion in a turbine.

[4]See Metghalchi and Keck, *Burning Velocities of Mixtures of Air with Methanol, Isooctane and Indolene at High Pressures and Temperatures*, Combustion and Flame, 48: 191-210

Chapter 3

THERMODYNAMIC MODELING OF THE FLOW

3.1 INTRODUCTION

The combustion models used for the simulations were based on Arrhenius Kinetics, Eddy-Dissipation or "Turbulent length scales" and the conserved scalar or PDF approach, all of which utilize differing forms of the basic conservation equations for the flow field (mass, momentum, energy, species, etc). Hence, in the interest of clarity the governing equations of the flow for the PDF method will be treated separately from the "traditional" Arrhenius kinetics (or reaction rate based) approach and the Eddy Dissipation model.

3.2 MASS, MOMENTUM, ENERGY AND SPECIES CONSERVATION

The behavior of single component fluids (i.e. fluid containing a single species) can be described and predicted by application of the principles of conservation mass (producing the continuity equation), conservation of linear momentum or Newton's second law (yielding the Navier-Stokes equations) and conservation of energy or the energy balance (giving the energy equation) all for a differential control volume. Specifically, in the absense of mass creation or destruction (e.g. no nuclear processes) the application of mass conservation on a differential basis yields

$$\frac{\partial \rho}{\partial t} + \nabla \cdot (\rho \vec{V}) = 0 \tag{3.1}$$

where ρ is the fluid density and $\vec{V}$ is the bulk flow velocity. With the application of Newton's second law for fluid motion (for an open system) we have the fluid equations of

motion (neglecting gravitational forces)

$$\frac{\partial}{\partial t}(\vec{V}) + \nabla \cdot (\rho \vec{V}^2) = -\nabla P + \nabla \cdot (\overline{\tau}) \tag{3.2}$$

where P is the local (or static) pressure and $\overline{\tau}$ is the shear stress tensor which includes the viscous as well as dilation (compressible) effects. Note that since we are dealing with conservation of a vector quantity (force) the second term on the left has a special interpretation. Specifically,

$$\nabla \cdot (\rho \vec{V} \vec{V}) = \begin{pmatrix} \rho V_i \frac{\partial V_i}{\partial x_i} + \rho V_i \frac{\partial V_j}{\partial x_j} + \rho V_i \frac{\partial V_i}{\partial x_i} + \rho V_j \frac{\partial V_i}{\partial x_j} \\ .. \end{pmatrix} \tag{3.3}$$

for the two-dimensional case where i and j refer to the x and y coordinate directions. The stress tensor $\overline{\tau}$ is taken to mean the following

$$\overline{\tau} = \mu \left[(\nabla \vec{V} + \nabla \vec{V}^T) - 2/3 (\nabla \cdot \vec{V}) I \right] \tag{3.4}$$

where μ is the absolute fluid viscosity and I is the identity matrix. In the case of turbulent flow the typical approach is to replace absolute viscosity (a property of the fluid) with an effective viscosity reflecting the enhanced diffusion due to fluctuating or oscillatory motion of the flow (i.e. $\mu_{eff} = \mu + \mu_t$). Finally, conservation of energy can be applied for a differential control volume (for a multi-component mixture while neglecting radiative energy transfer) to yield

$$\frac{\partial}{\partial t}(\rho e) + \nabla \cdot (\vec{V}(\rho e + P)) = -\nabla \cdot \left(k \nabla T - \sum_j h_j \hat{J}_j + (\overline{\tau} \cdot \vec{V}) \right) + S_h \tag{3.5}$$

where k is the (mixture) thermal conductivity of the fluid (replaced by $k_{eff} \equiv k + k_t$ in the case of turbulent flow), $\hat{J}_j$ is the diffusion flux of species j (to be discussed subsequently), S_h is an energy source term (due, for example, to chemical reactions) and e is defined as the total energy of the mixture per unit mass neglecting changes in gravitational potential energy ($e \equiv u(T) + |\vec{V}|^2/2$ where $u(T)$ is the mixture specific internal energy). Note that if we introduce a turbulent Prandlt number

$$Pr_t \equiv \frac{\mu_t C_p}{k_t} \tag{3.6}$$

we can express the effective thermal conductivity as

$$k_{eff} \equiv k + k_t = k + \frac{\mu_t C_p}{Pr_t} \tag{3.7}$$

Terms in (3.5) which may be unfamiliar to us include the diffusive term (second in brackets on the right hand side) resulting from species transport.

In the case of multi-component fluids the enthalpy h of the mixture is calculated via the fact that enthalpy, for an ideal mixture, is an additive property

$$h = \sum_j \chi_j h_j \tag{3.8}$$

where

$$h_j = h_j^{ref} + [h_j - h_j^{ref}] \tag{3.9}$$

and χ_j is the mass fraction of the j^{th} species. Also note that for an ideal gas enthalpy and energy are related via the following

$$e(T, \vec{V}) = u(T) + |\vec{V}|^2/2 = h(T) - P\nu + |\vec{V}|^2/2 = h(T) - R_m T + |\vec{V}|^2/2 \tag{3.10}$$

where R_m is the mixture gas constant. Species conservation is imposed via

$$\frac{\partial}{\partial t}(\rho\chi_j) + \nabla \cdot (\rho\vec{V}\chi_j) = -\nabla \cdot \hat{J}_j + R_j \tag{3.11}$$

where R_j is the net rate of production of species j. The second term on the left refers to the net convective flux of species j while the first term on the right represents the net diffusive flux. Note that conservation of mass implies (and is enforced via the requirement)

$$\sum_j \chi_j = 1 \tag{3.12}$$

In the case of laminar flow $\hat{J}_j$ is calculated using Fick's law for a dilute mixture (i.e. we assume that each of the mixture components behave as if they are dilutants within an "parent" fluid (in our case air)). Or

$$\hat{J}_j \equiv J_{j,i} = D_{j,i}\nabla\chi_j \tag{3.13}$$

where $D_{j,i}$ is the (assumed constant) diffusivity of species j into the surrounding fluid i (air). In the case of turbulent flow, mass transfer is enhanced and we can replace diffusion with an *effective* diffusion ($D_{j,i} \rightarrow D_{j,i}^{eff}$) as in the case with energy (k) and momentum diffusivity (μ). Finally, the equation of state (used previously) is simply

$$Pv = R_m T \tag{3.14}$$

where the mixture gas constant R_m is given by

$$R_m = R_u \sum_j \frac{\chi_j}{MW_j} \tag{3.15}$$

3.2.1 TURBULENCE MODELING

While conservation of mass, momentum and energy are relatively transparent concepts the same cannot be said for turbulence quantities and modeling in general. The phenomena of turbulence (and the associated difficulty of modeling) arises out of the fact that not all solutions to the Navier-Stokes, continuity and energy equations are stable. For some flows, slight perturbations (in velocity, pressure, temperature, etc) within the fluid stream are damped out, while for others these pertubations (which can be microscopic or macroscopic) grow until the overall flow field is altered. This purturbation, or disturbance of the flow field is characterized by time and spatially dependent fluctuations in all properties. Specifically, in the case of steady flow (in the mean), all properties can be represented as the sum of the mean property value $\overline{R}$ and a fluctuating component $r(t)$. Hence, Pressure, Temperature and momentum are generally expressed as $R(t) = \overline{R} + r(t)$. Now, given that most problems of practical interest are concerned with quantities in the mean (e.g. average shear stress or total drag on a surface, average heat transfer, etc) it is natural to attempt to solve the governing equations of motion for the *average values of the quantities of interest*. Specifically, we desire expressions for all time-averaged quantities $\overline{R}$ which can be found by integrating the governing expressions for the flow over some time period much greater than the period of turbulence. This approach, advocated and implemented by Sir Reynolds is refered to as "Reynolds averaging".

The next prudent question to ask is what physical situations, in terms of geometry, we wish to model. After all, substitution of our time-dependent properties $\vec{V}(t)$, $T(t)$, etc would, even after Reynolds averaging yield an intractable and complex set of governing equations for the flow with dependent variables $\overline{\vec{V}}$ and $\vec{v}(t)$ in the case of the Navier-Stokes equations alone. In fact, in terms of velocities, we have as set of three equations enforcing momentum conservation and six unknowns (the three components of the mean and fluctuating velocity).[1] This predicament is termed the *closure problem of turbulence* and, in a purely mathematical sense, renders the flow solution unattainable. However, if one assumes that the turbulence is isotropic, in other words

$$\overline{u'^2(t)} = \overline{v'^2(t)} = \overline{w'^2(t)} \tag{3.16}$$

(where again the mean is taken over some period greater that the period of the turbulent fluctuation), then after making boundary layer assumptions the number of unknowns is reduced, resulting in a set of *time-averaged* Navier-Stokes equations where the molecular

[1] Note that strictly speaking, pressure has a fluctuating component as well, but we will be neglecting this.

viscosity is replaced by the effective viscosity[2]

$$\mu_{eff} \equiv \mu + \mu_t \tag{3.18}$$

However, strictly speaking, one would appear to be none the wiser given that we have just given another name (turbulent viscosity) μ_t to an unknown quantity (namely $\overline{u'v'}$). Attempting another route we perform the following operation (where NS_j is the j^{th} direction Navier-Stokes equation)

$$\sum_j NS_J \cdot (\vec{V} + v\vec{(t)}) \tag{3.19}$$

After Reynolds averaging the result and making boundary layer assumptions we have a conservation equation for κ (the average turbulent kinetic energy per unit mass $\overline{(v')^2 + (u')^2}$) of the form

$$\frac{\partial}{\partial t}(\rho\kappa) + \frac{\partial}{\partial x_i}(\rho\kappa u_i) = \frac{\partial}{\partial x_j}(\Gamma_\omega \frac{\partial \kappa}{\partial x_j}) + G_\kappa - D_\kappa \tag{3.20}$$

where Y_k, G_κ and Γ_κ represent the dissipation, production and diffusion of κ, (notice the gradient transport formulation as with flow shear stress or heat transfer). The generation of turbulent kinetic energy is related to the vorticity of the flow

$$G_\kappa = -\rho\overline{u_i' u_j'}\frac{\partial u_j}{\partial x_i} = \mu_t S^2 \tag{3.21}$$

where S^2 is the square of the modulus of the mean rate-or-strain tensor. In addition, dissipation (or destruction) and the diffusivity of κ are given by

$$D_\kappa = \rho\beta f \kappa\omega \tag{3.22}$$

$$\Gamma_\kappa = \mu + \frac{\mu_t}{\sigma_\kappa} \tag{3.23}$$

where σ_κ is the turbulent Prandlt number based on κ, β is a constant, $f(\text{Vorticity}, \omega)$ and the new quantity ω is the dissipation ϵ per unit turbulent kinetic energy of the flow (or, if you like, the turbulence frequency). To arrive at the conservation equation for turbulent frequency ω we postulate that (like κ), ω is subject to convection, diffusion, generation and dissipation. Thus, we have an analogous expression to that of κ

$$\frac{\partial}{\partial t}(\rho\omega) + \frac{\partial}{\partial x_i}(\rho\omega u_i) = \frac{\partial}{\partial x_j}(\Gamma_\omega \frac{\partial \omega}{\partial x_j}) + G_\omega - D_\omega \tag{3.24}$$

[2]The turbulent viscosity replaces the remaining (after making BL assumptions) time-averaged fluctuating velocity components via

$$\mu_t \equiv -\frac{\rho\overline{u'v'}}{\partial U/\partial y} \tag{3.17}$$

according to the Boussinesq formulation.

where the generation and dissipation of ω are modeled via

$$G_\omega = \alpha \frac{\omega}{\kappa} G_\kappa \tag{3.25}$$

$$Y_\omega = \rho \beta d \omega^2 \tag{3.26}$$

where $d = f(\omega, \text{vorticity})$ The diffusion of ω is also given by

$$\Gamma_\omega = \mu + \frac{\mu}{\sigma_w} \tag{3.27}$$

where σ_ω is the Prandtl number based on ω. Finally, the set of momentum (related) equations are closed by noting that (on dimensional grounds)

$$\mu_t = \alpha \frac{\rho \kappa}{\omega} \tag{3.28}$$

where the significance of the dimensionless quantity α will become apparent with the introduction of transition modeling. Complete closure of the system of equations (the energy and species turbulent diffusion have not been dealt with) can be achieved by noting that, physically speaking, all conservation equations (except mass) include all the same basic processes (diffusion and convection) and, within the boundary-layer (in the absense of any pressure gradient), take on identical mathematical forms. Hence one might presume $\mu_t \sim k_t \sim D_t$. Or to be more rigorous

$$k_t = \frac{\mu_t C_p}{Pr_t} \tag{3.29}$$

where Pr_t is the turbulent Prandlt number (assumed to be a constant). And in the case of species diffusion

$$D_t = \frac{\mu_t}{\rho Sch_t} \tag{3.30}$$

where the turbulent Schmidt Sch_t number is also taken as a constant. The values for the turbulent Prandlt and Schmidt numbers are 0.85 and 0.7 respectively.

3.3 CHEMICAL REACTIONS

3.3.1 ARRHENIUS KINETICS

The effects of chemical reactions enter into the computation of the flow field by way of the energy equation (and indirectly by way of the dependence of various fluid (*not flow*) properties on composition). Specifically, combustion enters into the energy equation in the

form of the dependence of specific enthalpy h on mixture composition and the energy source term S_h. Mixture specific enthalpy is given by (assuming ideal gas mixture behavior)

$$h = \sum_j \chi_j h_j(T) = \sum_j \chi_j (h_j^{ref} + \int_{T_{ref}}^{T} C_{p,j} dT) \tag{3.31}$$

and the energy source term is

$$S_h = \sum_j (h_j^{ref} + \int_{T_{ref}^j}^{T} C_{p,j} dT) MW_j \sum_{r=1}^{N_R} \hat{R}_{j,r} \tag{3.32}$$

where $R_{j,r}$ is the volumetric rate of production of species j due to reaction r. The reaction corresponds to a forward reaction of the form

$$\sum_r \sum_j \nu_{j,r}^{'} X_{j,r} \overset{k_{f,r}}{\Rightarrow} \sum_r \sum_j \nu_{j,r}^{''} X_{j,r} \tag{3.33}$$

where the summation is over all reaction mechanisms r with forward reaction rate $k_{f,r}$ and reactant and product stoichiometric coeffients are labeled $\nu_{j,r}^{'}$ and $\nu_{j,r}^{''}$. In addition, the X's are simply labels for the relevant species.[3] Note that global (as opposed to reversible elemental reactions) are utilized in this study. Assuming that the overall reaction rate is a function of reactant species concentrations $[C_j]$ and temperature, the form for the rate of species production (for species j) is

$$\hat{R}_j = \sum_r [(\nu_{j,r}^{''} - \nu_{j,r}^{'}) k_{f,r} \prod_j C_j^{\eta_{j,r}}] \tag{3.34}$$

where $\eta_{j,r}$ is the corresponding reaction exponent for species j in reaction r. The forward reaction rate constant $k_{f,r} = f(T)$ is given by

$$k_{f,r} = A_r T^{\beta_r} e^{-\frac{E_r}{R_u T}} \tag{3.35}$$

where E_r, β_r and A_r are emperical constants.

3.3.2 EDDY DISSIPATION MODEL

Now, the previous expression for the rate of species production does not in any way directly take into account the effects of turbulence and turbulent mixing. In fact, the only path of influence for turbulence is via the rate of species and energy transport (i.e. the effect of turbulent mixing on mean concentrations $\overline{C}$ and fluid temperature $\overline{T}$). We can

[3] Thus, the simple stoichiometric equation $1CO_2 \Rightarrow 1C + 1O_2$ would involve the species (X's) C, O_2 and CO_2 with stoichiometric coefficients 1 for $\nu^{'}$, and 1 and 1 for the $\nu^{''}$'s.

begin to appreciate the influence which turbulence and turbulent structures have on the combustion process by introducing the concept of a "rate-limiting process". An example of this is would be the assumptions made in boundary layer analysis as to the governing or rate-limiting process for momentum transfer (i.e. the comparative importance of convective vs. diffusive (viscous) transfer of momentum). The same is true for turbulence and analysis of turbulent flow where the boundary layer is partitioned into regions dominated by certain momentum transfer processes (viscous effects in the laminar sub-layer and turbulent "diffusion" in the log and wake region). Hence, it should not come as a surprise that there are limiting processes associated with chemical reactions as well. Specifically, one could imagine the following possible extremes: Combustion occurs in regions of much smaller scale than the smallest turbulent eddies. Conversely, the combustion region could be large compared to the mixing length, etc. Note that in the first case this must imply that on a differential (control volume) basis, the reaction is governed (or if you like "rate-limited") by chemical kinetics that are, on the scale of the flame, laminar in character. Hence, we can postulate that under the first extreme the reaction is laminar and "kinetically limited". Another way of say this is that in the first case, turbulent fluctuations due to the motion of turbulent eddies appears (relatively speaking) *macroscopic* when compared with the scale of chemical reaction.

This is in contrast to the latter extreme where we postulate that turbulent structures populated the combustion region. Hence, in this case we can say that turbulence and turbulent mixing play an important, if not dominant role in governing the reaction rate.[4] Specifically, in the latter regime we can think of combustion occuring when "clumps" of unburned fuel are broken down into smaller "clumps" of sufficiently small volume (compared to surface area) to allow for complete combustion. We could operationalize this approach by surmising that as the eddies rotate, there exist some likelihood of "breakup" (into smaller eddies) per revolution. Note that this implies the greater the number of revolutions per unit time (i.e. the higher the turbulence frequency ω) the higher the rate of eddy breakup and combustion. In addition, one would assume that as the amount of fuel present in the fluid increases (per unit volume) the greater the consumption rate for the fuel. Hence, we can render these observations in mathematical form via the following.

$$\dot{m}'''_{fuel} \propto -\omega \rho \chi_{fuel} \tag{3.36}$$

where $\dot{m}'''_{fuel}$ is the fuel consumption per unit volume per unit time.

Applying the above to a *single-step* reaction mechanism we have the slightly modified expressions for the reaction rate as the minimum of either of the two expressions

$$R_j = \nu'_j MW_j A \rho \omega \min[\frac{\chi_R}{\nu'_R MW_R}] \tag{3.37}$$

[4]Note that this combustion regime is refered to as the "flamelets-in-eddies" regime.

or

$$R_j = AB\nu_j^{'} MW_j \rho\omega \frac{\sum_P \chi_P}{\sum_j^N \nu_j^{''} MW_j} \tag{3.38}$$

where χ_P and χ_R are the mass fractions of particular product P and reactant R species (A and B are empirically derived constants). Note that the above formulation is required since the overall reaction is limited by the breakup and combustion of the *slowest* reacting component species.[5]

3.4 FLUID PROPERTIES

Mixture fluid properties such as the viscosity μ, thermal conductivity k, specific heat C_p were all calculated using the ideal gas mixing law based on indivudual component mixture properties. Thus, given individual fluid component properties ψ_j (on a per mole basis) we can express the mixture property ψ as

$$\overline{\psi}(T) = \sum_j y_j \overline{\psi}_j(T) \tag{3.39}$$

where y_j is the mixture mole fraction of species j.

The individual component fluid viscosities μ_j are given by Sutherland curve fits of the following form.

$$\mu_j = \mu_{0,j} (\frac{T}{T_{0,j}})^{3/2} (\frac{T_{0,j} - S_j}{T + S_j}) \tag{3.40}$$

where $\mu_{0,j}$, $T_{0,j}$ and S_j are empirical constants. The individual fluid component molar specific heats $\overline{C}_{p,j}$ are given by the polynomial curve fit

$$\overline{C}_{p,j}(T) = \phi_j + \varrho_j T + \xi_j T^2 + \upsilon_j T^3 + \kappa_j T^4 \tag{3.41}$$

Likewise, the individual component fluid thermal conductivities $k_j(T)$ are calculated using kinetic theory.

$$k_j(T) = k_j(C_{p,j}(T), \mu_j(T)) = \frac{15R\mu_j}{4MW_j} \left[\frac{4C_{p,j}MW_j}{15R_u} + 1/3 \right] \tag{3.42}$$

where R_u is the universal gas constant

[5] Model based on the work of Magnussen and Hjertager utilizing the eddy-breakup model of Spalding

3.5 BOUNDARY CONDITIONS

The boundary conditions imposed for momentum, energy and species conservation should be familiar (e.g. no slip, adiabatic/constant wall temperature, etc). However, boundary conditions which are most interesting and least *obvious* are those used in the conservation equations for specific turbulent kinetic energy κ and frequency ω. The boundaries of which we speak are (for any computational domain) the inlets, outlets and surfaces. The simulations to be conducted here specify the values of κ and ω at inlets and outlets (in the case of backflow). But on surfaces (i.e. blade surfaces) the only boundary condition relevant (to the momentum equation) is no slip. The method used for implementing boundary conditions for the turbulence quantities κ and ω near a surface (i.e the first grid point off the wall) is as follows: The region adjacent to a no slip surface (a wall)

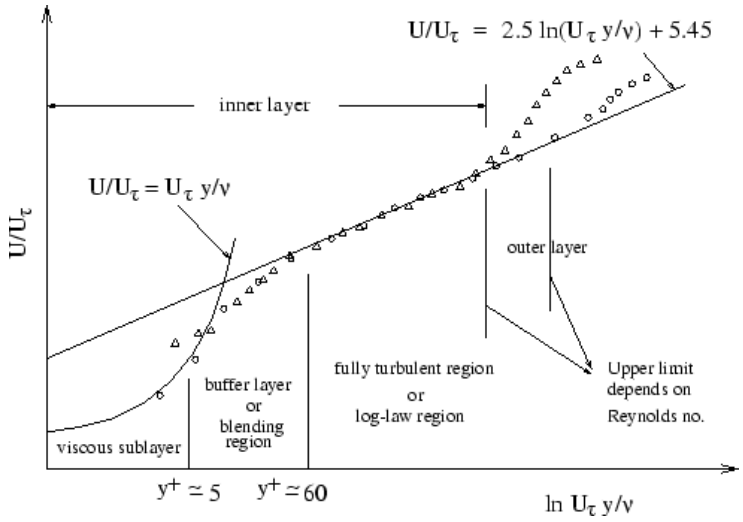

Figure 3.1: Near wall flow regimes

is (*in turbulent flow*) characterized by a sucession of flow regimes where certain physical effects dominate. Specifically, at the wall turbulent velocity oscillations are damped (in fact turbulent kinetic energy vanishes very near the wall), hence, the flow is *locally* laminar and referred to as the viscous or laminar sublayer. Further from the wall the effects of turbulent transport dominate diffusion. It is this region which specifies the *log layer* and where the *law of the wall* applies (note the "buffer" region bridging the laminar and log layers (see Figure 3.1)). Thus, wall boundary conditions depend on which region the first *off the wall* grid point resides. If the first grid point is in the viscous sublayer (which extends, approximately, over the interval $0 < y^+ < 5$)[6] we have, for all intents and

[6] y^+ is defined as $y^+ \equiv y(u^*/\nu) = (y/\nu)\sqrt{\tau_w/\rho}$ where τ_w is the wall shear stress.

purposes resolved the flow field to the wall.[7] Specifically, for a smooth wall (no surface

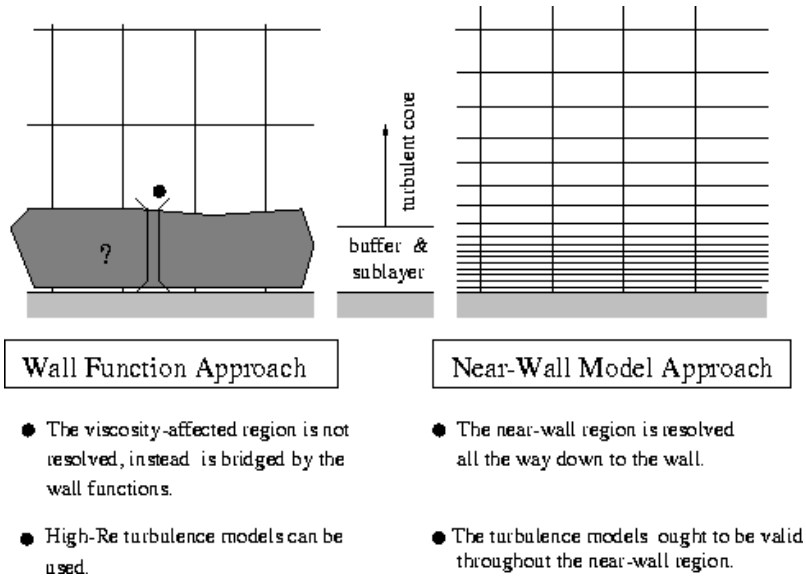

Figure 3.2: Wall boundary conditions

roughness) the boundary conditions for κ and ω are[8]

$$\omega_{wall} = 66.6\frac{\nu(u^*)^2}{(y^+)^2} \tag{3.43}$$

$$\kappa_{wall} = 0 \tag{3.44}$$

Thus, our approach here is to resolve the flow all the way through (into) the viscous sublayer.

Note that the previous discussion only refers to *surface* boundary conditions for κ and ω. In the case of inlet boundary conditions for turbulent quantities we instead specify the values of turbulent intensity Tu and the hydraulic diametery H_D. If one assumes the inlet flow is turbulent and fully developed, then a unique value for the length scale exists at the inlet (presumably some fraction of the total inlet diameter (since the turbulent mixing length cannot be greater than the flow's confinement distance)). Specifically,

$$l = 0.007H_D \tag{3.45}$$

[7]Note that this is in contrast to the wall function approach which assumes the "near wall", or first grid point resides in the log-layer and bridges the spatial gap via wall functions (see Figure 3.2).

[8]This assumes a value of y^+ less than 10 where u^* is the friction velocity $(\tau_w/\rho)^{1/2}$.

where ω can be related to the length scale l and turbulent specific kinetic energy κ via

$$\omega = \frac{k^{1/2}}{0.56l} = 255.1\frac{k^{1/2}}{H_D} \tag{3.46}$$

κ on the other hand is related to turbulent intensity Tu via

$$Tu \equiv \frac{\sqrt{3\kappa/2}}{U_{ref}} \Rightarrow \kappa = \frac{2}{3}(TuU_{ref})^2 \tag{3.47}$$

where the reference velocity U_{ref} is the inlet bulk flow velocity magnitude $|\vec{V}_{in}|$.

Finally, a word must be said about the methodology employed by an elliptic solver, i.e the generation of a solution for a set of eliptic equations where, apriori, the values of all quantities are not known on all boundaries. Specifically, while inlet and surface flow conditions are known (i.e. specified by the user in the form of boundary conditions), the outlet flow properties (except local pressure) are unknowns (part of our purpose is to solve for exit flow quantities as well as all properties in between). The solution is to specify gradients of properties at the exit consistant with the fully-developed solution (no changes in flow properties after the fluid exits the computational domain). In other words, we implicitly apply a boundary condition at the flow exit in the form of vanishing property gradients. Unfortunately, this requires that we iterate the solution while updating exit flow properties based on the previous estimates just downstream of the computational domain outlet.[9]

3.6 TRANSITION MODELING

The previous treatment does not address transition (even high Reynolds number flow contains an initial laminar region). Clearly the means of modeling transition is to make the turbulent viscosity of the following functional form

$$\mu_t = \alpha\frac{\rho\kappa}{\omega} \tag{3.48}$$

where $\alpha = f(\kappa, \omega)$ and $\alpha \rightarrow$ (small quantity) or $\alpha \rightarrow 1$ in the laminar (typified by low values for k) or turbulent region (typified by high values for κ) respectively. Bearing this in mind α is modeled via the following

$$\alpha = \frac{0.024 + Re_t/6}{1 + Re_t/6} \tag{3.49}$$

where $Re_t \equiv \rho\kappa/\mu\omega$.[10]

[9] Hence the solver employs an iterative approach (as opposed to a marching solution as is the case for supersonic (where the governing equations are parabolic in nature)).

[10] Note that the asymptotic behavior of α is as desired (i.e. for high values of κ/ω or κ, $\alpha \rightarrow 1$).

3.7 CONSERVED SCALAR APPROACH

The approach previously taken attempts to incorporate the effects of turbulence by calculating an *effective* viscosity, thermal conductivity and species diffusion. However, the introduction of these *effective diffusivities* has no direct effect on rate of species creation via the general expression for the reaction rate

$$\hat{R}_j = \sum_r [(\nu''_{j,r} - \nu'_{j,r}) k_{f_r} \prod_j C_j{}^{\eta_{j,k}}] \tag{3.50}$$

where

$$k_{f,r} = A_r T^{\beta_r} e^{-\frac{E_r}{R_u T}} \tag{3.51}$$

Specifically, small fluctuations in temperature about the mean (indicative of turbulent flow) can have a significant effect on the reaction rate due to the nonlinear behavior of the exponential. The same is true for fluctuating values of concentration C. Another way of stating this is that *inserting the time mean values for T and C into the reaction rate expression effectively neglects the fluctuating nature of these values and renders the reaction as essentially laminar.*

3.7.1 CONSERVATION EQUATIONS FOR NON-PREMIXED COMBUSTION

Given that the effects of turbulence not captured by the previous "laminar" approach are due to neglecting temperature and concentration fluctuations, we must restate species and energy conservation if we are to take into account these effects of turbulence. Specifically, we intend to neglect the reaction rate and its calculation entirely by assuming the reaction takes place instantaneously once the mixture has reached stoichiometric proportions. Thus, the following approach will concentrate more on the transport mechanisms occuring within the mixture instead of the reaction chemistry (in other words, assume species transport is the rate-limiting process).

To reduce computational complexity species conservation is enforced using the "conserved scalar approach" which is formulated as follows. Note that the previous approach for laminary combustion utilized multiple species (in our case Oxygen, Nitrogen, water vapor, Carbon Dioxide and fuel (Kerosene)). However, it is possible to describe the mixture composition in terms of material which has its origin either within the fuel or oxidizer stream. Specifically, we can express the total mass of the mixture anywhere in the computational domain as

$$m_{mixture} = m_{fuel} + m_{oxidizer} + m_{products}$$

$$\Rightarrow 1 = \chi_{fuel} + \chi_{ox} + \chi_{prod} \tag{3.52}$$

or

$$f_{fuel} + f_{ox} = 1 \tag{3.53}$$

where f_{fuel} and f_{ox} are the fraction of material having its origin in the fuel and oxidizer stream respectively (this is, of course assuming a single inlet fuel stream). But, in terms of a quantity f defined as the ratio of mass have is "origin in fuel stream" and the mixture mass we have

$f \equiv$ "mass of material with origin in fuel stream/mass of mixture" =

$$\frac{m_{fs}}{m_{fuel}}\frac{m_{fuel}}{m_{mixture}} + \frac{m_{fs}}{m_{products}}\frac{m_{products}}{m_{mixture}} + \frac{m_{fs}}{m_{oxidizer}}\frac{m_{oxidizer}}{m_{mixture}} =$$

$$(1)\chi_{fuel} + (\frac{1}{1+(A/F)_{stoc}})\chi_{prod} + (0)\chi_{ox} = \chi_{fuel} + f_{stoc}\chi_{prod} \tag{3.54}$$

where m_{fx} is the "mass of fuel stuff" and

$$f_{stoc} \equiv (1/(1 + (A/F)_{stoc})) \tag{3.55}$$

This definition of the mixture fraction is highly useful if we make several assumptions regarding the combustion process (some of which have already been stated).

1. Chemistry is *fast* compared to convection and diffusion
2. Combustion occurs instantaneously and completely when mixture is stoichiometric (flame sheet assumption)
3. Oxidant and fuel are segregated (i.e. no unburned fuel in free-stream and no oxidizer inside flame)
4. Diffusion is binary and follows Fick's Law
5. Radiative energy transfer is neglected

Specifically item 2 implies the partition of the flow field into three zones: the internal (no oxidizer present), flame sheet (infinitely thin region where the A/F ratio is stoichiometric), and external zone (no unburned fuel present). The assumptions regarding composition are illustrated in Figure 3.3.

Note that the previous assumptions regarding internal/flame-sheet/external (to flame) impose the following conditions for mass conservation

$$\begin{aligned} \chi_{fuel} + \chi_{prod} &= 1, \quad \text{inside flame (internal zone)} \\ \chi_{prod} &= 1, \quad \text{at flame sheet} \\ \chi_{ox} + \chi_{prod} &= 1, \quad \text{outside flame (external zone)} \end{aligned} \tag{3.56}$$

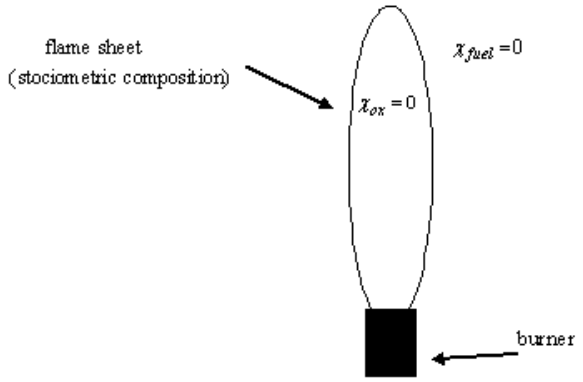

Figure 3.3: Flame sheet compositions

This leads to the following expressions for fuel and product mass fraction inside the flame sheet via 3.54

$$\chi_{ox}^{internal} = 0 \tag{3.57}$$

$$f = \chi_{fuel} + f_{stoc}\chi_{prod} = \chi_{fuel} + f_{stoc}(1 - \chi_{fuel})$$

$$\Rightarrow \chi_{fuel}^{internal} = \frac{f - f_{stoc}}{1 - f_{stoc}} \tag{3.58}$$

$$f = \chi_{fuel} + f_{stoc}\chi_{prod} = (1 - \chi_{prod}) + f_{stoc}(\chi_{prod})$$

$$\Rightarrow \chi_{prod}^{internal} = \frac{1 - f}{1 - f_{stoc}} \tag{3.59}$$

And for the region external to the flame sheet we have

$$\chi_{fuel} = 0 \tag{3.60}$$

$$f = \chi_{fuel} + f_{stoc}\chi_{prod} = f_{stoc}\chi_{prod}$$

$$\Rightarrow \chi_{prod}^{external} = \frac{f}{f_{stoc}} \tag{3.61}$$

$$f = \chi_{fuel} + f_{stoc}\chi_{prod} = f_{stoc}\chi_{prod} = f_{stoc}(1 - \chi_{ox})$$

$$\Rightarrow \chi_{ox}^{external} = 1 - \frac{f}{f_{stoc}} \tag{3.62}$$

Note that all expressions are linear in f. Thus, the relationship between mixture fraction and composition is a simple one as displayed in Figure 3.4. Now, for this approach to

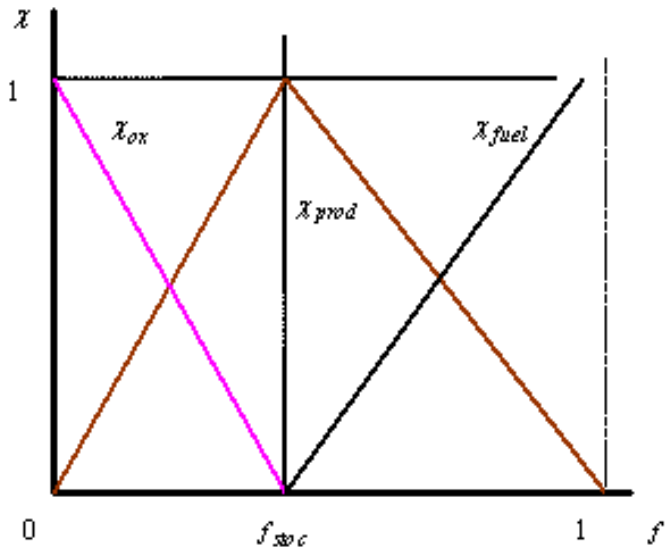

Figure 3.4: Mass fractions χ_j vs. mixture fraction f

be useful, not only must chemical composition be related to f, but properties such as density and temperature must also be related to mixture fraction f and enthalpy where the relevant formulation of the energy equation (in terms of enthalpy) is

$$\frac{\partial}{\partial t}(\rho h) + \nabla \cdot (\rho \vec{V} h) = \nabla \cdot (\frac{k_t}{C_p} \nabla h) + S_h \tag{3.63}$$

where all quantities are as defined previously. Note that the mixture fraction, since we are intending to model turbulent combustion, must be a fluctuating quantitiy posessing a mean $\overline{f}$ and fluctuating component f' (with variance $\overline{f'^2}$)). If we also assume equal diffusivities D for all species then species conservation can be expressed in terms of a conservation equation *involving the mean mixture fraction* $\overline{f}$ *and its variance* $\overline{f'^2}$.

$$\frac{\partial}{\partial t}(\rho \overline{f}) + \nabla \cdot (\rho \vec{V} \overline{f}) = \nabla \cdot (\frac{\mu_t}{\sigma_t} \nabla \overline{f}) \tag{3.64}$$

$$\frac{\partial}{\partial t}(\rho\overline{f'^2}) + \nabla\cdot(\rho\vec{V}\overline{f'^2}) =$$
$$\nabla\cdot(\frac{\mu_t}{\sigma_t}\nabla\overline{f'^2}) + C_g\mu_t(\nabla^2\overline{f}) - C_d\rho\frac{\epsilon}{k}\overline{f'^2} \tag{3.65}$$

Note that the coeficients σ_t, C_g and C_d are empirical constants. Specifically, the above expression is arrived at via combining the species conservation equations and using the definition of mixture fraction f. The result is a conservation equation (3.64) whose first right hand side term represents species diffusion, and first and second terms on the left, represent unsteady effects and convection of species via bulk motion respectively. Thus, we have been able to reduce the number of species conservation equations from (in our case) four to two. Of course the "direct" incorporation of turbulent fluctuations into the equation for species transport and energy has not yet been performed. This incorporation is done by (again) noting that f is a fluctuating quantity. Hence we can evaluate the mean value of any dependent flow property $\psi_i(f)$ according according to the weighting scheme

$$\overline{\psi_i(f)} = \int_0^1 p(f)\psi_i(f,h)df \tag{3.66}$$

where

$$\int_0^1 p(f)df = 1 \tag{3.67}$$

Thus, $p(f)$ is termed the probability density function and the method used here is termed a pdf combustion calculation. The functional dependence of $p(f)$ on the muxture fraction f has been approximated using semi-emperical methods and is described by the following expression:

$$p(f) = \frac{f^{\alpha-1}(1-f)^{\beta-1}}{\lambda} \tag{3.68}$$

where

$$\lambda(f,\alpha,\beta) \equiv \int_0^1 f^{\alpha-1}(1-f)^{\beta-1}df \tag{3.69}$$

$$\alpha(\overline{f},\overline{f'^2},\beta) \equiv \overline{f}\left[\frac{\overline{f}(1-\overline{f})}{\overline{f'^2}} - 1\right] \tag{3.70}$$

and

$$\beta(\overline{f},\overline{f'^2}) \equiv (1-\overline{f})\left[\frac{\overline{f}(1-\overline{f})}{\overline{f'^2}} - 1\right] \tag{3.71}$$

Finally, boundary conditions for f and $f^{'}$ are given at the computational boundaries such as inlets, outlets and surfaces (gradients in f and $f^{'}$ vanish at solid surfaces).

Chapter 4

NUMERICAL MODEL

4.1 APPROACH

The present endeavor attemps to simulate the important geometric and fluid mechanical conditions within a gas turbine. These conditions in particalar include flow around foil-like objects which can be moving or stationary (corresponding to rotor or stator blades), compressibility effects, work extraction (via rotor blades due to moving boundaries), repeating boundary conditions to simulate multiple blades within stages as well as appropriate turbulence modeling and chemical reactions for vapor combustion. The result is a 2-D linear cascade-type geometry in the xy plane utilizing the low Reynolds number (i.e. transitional) $\kappa - \omega$ turbulence model along with Arrhenius chemical kinetics, eddy-dissipation or PDF species conservation and transport (as described in the previous chapter).

4.2 THE GEOMETRY

The chosen geometry is a simple 2-D cascade of *generic* dimensions and shape (see Figure 4.1).[1] Specifically, a stage consisting of a stator and matched rotor are used to simulate flow inside a gas turbine albeit in a 2-dimensional sense. The overall dimensions of the computation space as illustrated in Figure 4.1 and given in Table 4.1

Table 4.1: Stage geometry summary

Domain height(m)	$Itsle(m)$	$Stetrle(m)$	$Rteto(m)$
0.08	0.0603	0.03145	0.0977

[1]The geometry used was generatured using the FLUENT preprocessor GAMBIT.

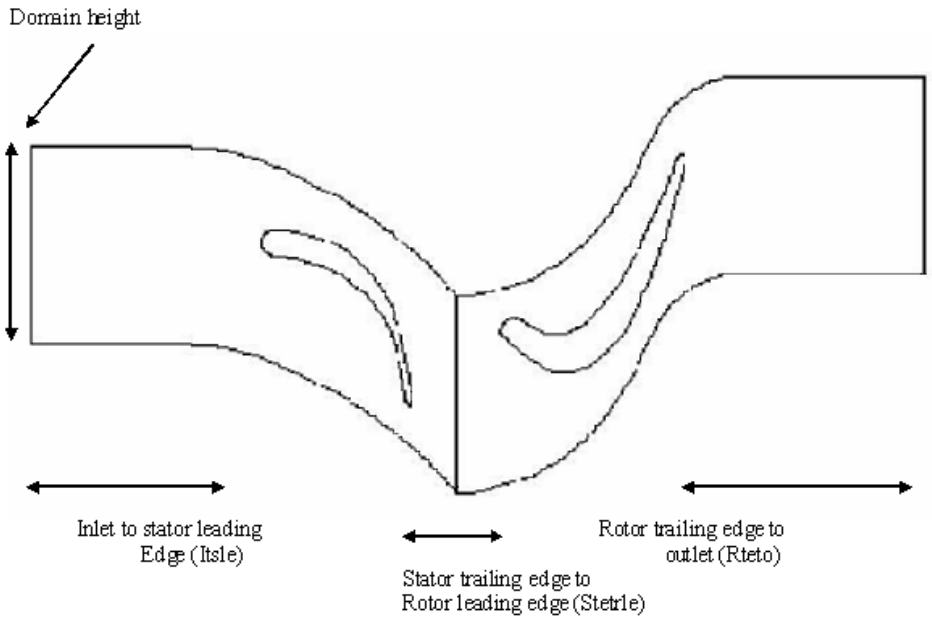

Figure 4.1: Linear cascade geometry (see Table 4.1 for dimensions (as labeled in parenthesis))

In addition, injector surface areas are given in 4.2

Table 4.2: Injector area

$Injectorlocation$	$Area$(m)
LESS (Rotor)	0.00073
LEPS (Rotor)	0.00046
MID (Rotor)	0.00042
LESS (Rotor)	0.00024
LEPS (Rotor)	0.00027
TESS (Rotor)	0.00031
TEPS (Rotor)	0.00028

The grid utilized is composed of a non-structured triangular mesh with quadrihedral elements within the boundary layer and contains approximately $35,000$ grid points.

Figure 4.2 displays the stator used, having overall turning in the relative and absolute frame of 75°, a cord length c of $0.0887m$, a cord to pitch ratio c/s of 1.11 and total uncovered turning τ of 70° (see Table 4.3). Figure 4.3 displays the matched rotor used,

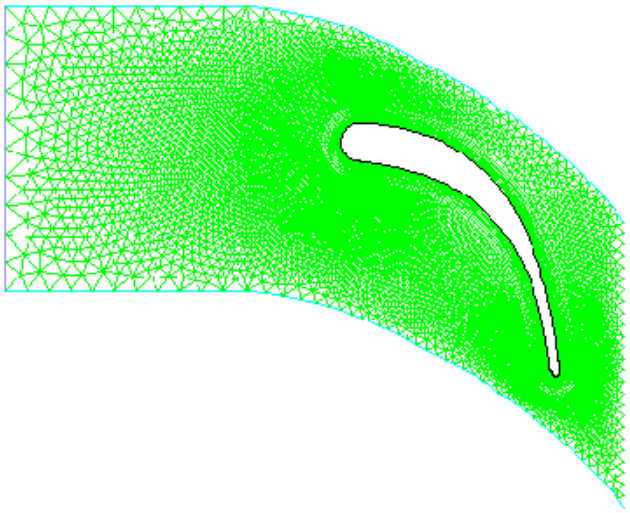

Figure 4.2: Stator geometry and grid

having overall turning in the relative frame of 118°, a cord length c of $0.1016m$, a cord to pitch ratio c/s of 1.27 and total uncovered turning τ of 32°. Note that these specifications are summarized in Table. 4.4.

Table 4.3: Stator geometry summary

$\alpha_1(\circ)$	$\alpha_2(\circ)$	$\alpha(\circ)$	$\beta_1(\circ)$	$\beta_2(\circ)$	$\beta(\circ)$	Cord(c) m	Pitch(s) m	C/S	τ
0	75	75	0	75	75	0.0887	0.08	1.11	70

Table 4.4: Rotor geometry summary

$\alpha_1(\circ)$	$\alpha_2(\circ)$	$\alpha(\circ)$	$\beta_1(\circ)$	$\beta_2(\circ)$	$\beta(\circ)$	cord(c) m	pitch(s) m	c/s	τ
69	47	116	37	81	118	0.1016	0.08	1.27	32

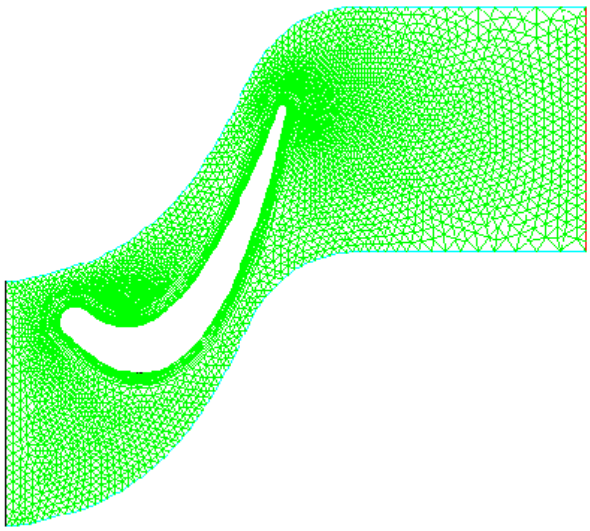

Figure 4.3: Rotor geometry and grid

4.3 BOUNDARY CONDITIONS

Boundary surface conditions for the geometry are labeled in Figure 4.4. Specifically, the domain inlet utilizes a pressure boundary condition for subsonic flow which resembles the conditions found in the combustor exit of a gas turbine (i.e. flow entering the high pressure turbine of which we are modeling). In particular, a total pressure of 35atm is used with an inlet total temperature of $1,700^{\circ}K$. In addition, the species composition reflects a stoichiometric combustion in the combustor followed by 50% dilution with air. These parameters are summarized in Table 4.5

Table 4.5: Inlet boundary conditions

$P_0(MPa)$	$T_0(\circ K)$	$Tu(\%)$	$\omega(1/s)$	$\chi_{C_{12}H_23}$	χ_{O_2}	χ_{CO_2}	χ_{H_2O}
$3.5(10^6)$	1700	5	836.4	0	0.122	0.076	0.031

The outlet boundary condition (corresponding to subsonic flow) is simply an exit local pressure of $2.5(10^6)MPa$. Boundary conditions at the fuel injection points on the foils (four on the stator and three on the rotor) are of the mass flow type, with a fuel temperature of $600^{\circ}K$ (conforming to the pyrolosis limit for JP-8). In contrast, fuel injection was varied from injection surface to surface to achieve a given approximate total injection rate. This tailoring of bulk flow injection rates to yield a certain total mass flow was necessarily conducted by trial and error, and thus resulted in slightly different injection rates for the various injectors.

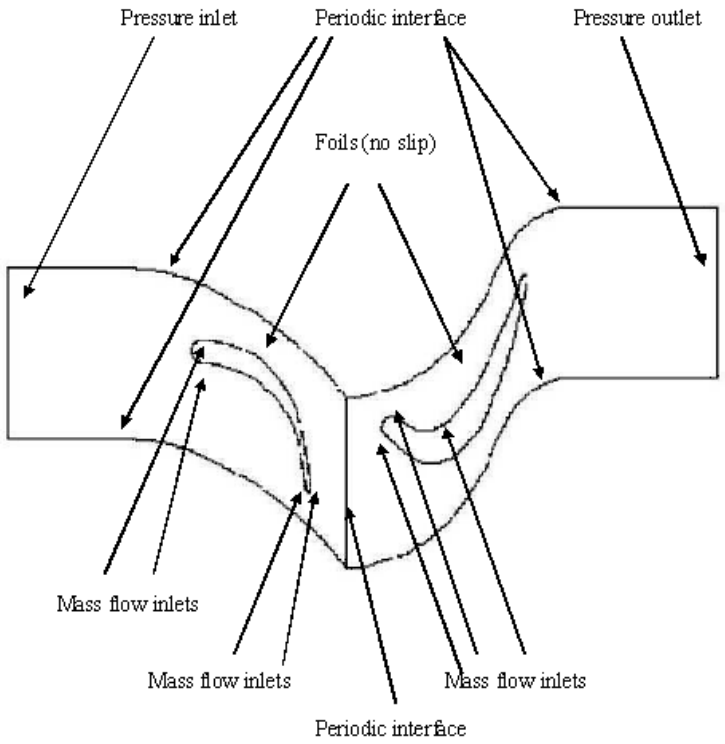

Figure 4.4: Domain boundary surfaces

In addition, foil surface conditions both included adiabatic and isothermal boundaries (with a constant wall temperature of $1,000°K$). Finally, the interface boundary conditions (see Figure 4.4) are simple grid point to grid point mappings from the top of the domain to the bottom and interpolative mappings for the stator-to-rotor interface (since grid points in the sliding mesh will not, in general, remain in alignment). Specific boundary conditions are given in Appendix E.

4.4 FLUID PROPERTIES

Given that we have assumed ideal gas behavior for the fluid the question arises as to whether air and fuel can be modeled as ideal gases throughout the flow field. In the case of the inlet flow (which is essentially air diluted with products of combustion) P_{crit}^{air} and T_{crit}^{air} are $3.7MPa$ and $132°K$. This yields an approximate reduced pressure P_R and temperature T_R of 1 and 10 respectively and a compresibility factor Z of about one. Hence, treatment of the freestream as an ideal gas is deemed acceptable. In the case of the unburned fuel (Kerosene) we are on much more contentious grounds. Specifically, the critical pressure

P_{crit} and temperature T_{crit} for jet fuel (JP-7) are $1.8MPa$ and $723^\circ K$ respectively. Hence, given that fuel will be entering the computational domain at approximately freestream pressures ($3.5MPa$) and with an injection temperature of $600^\circ K$ the reduced pressure and temperature are on the order of one. Thus, the assumption of ideal gas behavior will be a poor one near the point of fuel injection.[2] While this would result in highly inaccurate ideal gas behavior based calculations of density as a function of temperature and pressure, calculations of physical properties such as specific heat C_p and thus changes in enthalpy, entropy, etc may also suffer in terms of accuracy. From the definition of Z_h[3]

$$\overline{h}^{ideal} - \overline{h} = Z_h R_u T_{crit} \tag{4.1}$$

Now, we would expect fuel temperature to vary more then fuel pressure up to the point of combustion. Thus, taking the partial derivative of the above expression with respect to T holding pressure constant gives

$$\frac{\partial}{\partial T}(\overline{h}^{ideal} - \overline{h}) = \frac{\partial}{\partial T_r}\frac{T_{crit}}{T_{crit}} Z_h R_u = \frac{\partial}{\partial T_r} Z_h R_u \tag{4.2}$$

Noting the definition of C_p the above becomes (for evaluation at the point of injection where $T_r \approx 1$)

$$\begin{aligned}\overline{C}_p^{ideal} - \overline{C} = R_u \frac{\partial}{\partial T_r} Z(T_r, P_r)\Big|_{P_r} \Rightarrow \frac{\overline{C}_{P_r}^{ideal} - \overline{C}}{\overline{C}^{ideal}}\Big|_{P_r} &= \frac{R_u}{\overline{C}_{P_r}^{ideal}} \frac{\partial}{\partial T_r} Z(T_r, P_r)\Big|_{P_r=2} \\ \approx \frac{(8.3(10^3))}{556.9(10^3)} \frac{Z(1.5,2) - Z(0.5,2)}{1} &\cong \frac{(8.3(10^3))}{556.9(10^3)} \frac{1.5 - 7.5}{1} = -0.089\end{aligned} \tag{4.3}$$

i.e. an error in the estimate for specific heat on the order of 10%. Thus, estimates for changes in specific enthalpy, entropy, etc for the fuel near the point of fuel injection via the ideal gas behavior assumption will likely result in an error (of about) 10%. *However, it should be noted that rapid heating of the fuel will occur, thus rendering the behavior of the fuel as approximately ideal everywhere but very near the point of injection.*

Note that the reduced pressure for the fuel must exceed the value of one everywhere in the domain. This implies that the fuel must also be at a reduced pressure in excess of one (approximately 2, in fact) anywhere in the injection system and hence within the internal blade passages themselves. This has repercussions in terms of using the fuel as a coolant given that no phase change can occur as the fuel is heated, say from room temperature within the blade, to a temperature near the coking limit (approximately $600^\circ K$) at the point of injection into the freestream. Hence, heat transfer will result only in a sensible

[2] Specifically, the compressibility factor takes on a value of around 0.2.

[3] See generalized enthaloy chart for enthalpy deviation Z_h

enthalpy change in the fuel, thus reducing its effectiveness as a coolant. Having justified the assumption of ideal gas behavior all fluid properties are derived using *FLUENT*'s thermodynamic database according to the correlations given in the previous chapter.

The only remaining properties to determine are the binary diffusivities $D_{i,j}$ for an (assumed) dilute mixture. Specifically, for an ideal mixture, assuming dilute mixture behavior (i.e. the multi-component mixture behaves as a binary mixture with fuel, oxidizer and products diffusing into air) we have the correlation

$$D_{i,j} \propto (T^{3/2}/P) \tag{4.4}$$

Hence,

$$D_{i,j} = D_{i,j}^{ref} \frac{T^{3/2}/P}{T^{ref\,3/2}/P^{ref}} \tag{4.5}$$

Table 4.6: Calculated constant binary diffusivities for a temperature of $2,000^{\circ}K$ and pressure of $3(10^6)Pa$

Species i	Species j	$T^{ref\,\circ}K$	$P^{ref}MPa$	$D_{i,j}^{ref}(m^2/s)$	$D_{i,j}(m^2/s)$
CO_2	Air	273	0.1	$1.38(10^5)$	$0.9(10^5)$
H_2O	Air	273	0.1	$2.2(10^5)$	$1.45(10^5)$
$n-Dodecane$	N_2	399	0.1	$0.81(10^5)$	$0.37(10^5)$

Thus, given data for the reference diffusivity, temperatures and pressures, a new approximate diffusivity can be calculated via 4.5. Table 4.6 gives the reference as well as newly calculated values for species diffusivity of interest at a pressure of $3(10^6)Pa$ and a temperature of $2,000^{\circ}K$.

For the remaining diffusion coefficients (N_2, O_2 into air) where reference values are not available we can use the Chapman-Enskog correlation. The calculated diffusion coefficients are given in Table 4.7 for completeness and one should refer to Appendix B for details.

Table 4.7: Calculated constant binary diffusivities for a temperature of $2,000^{\circ}K$ and pressure of $3(10^6)Pa$ (using Chapman-Enskog correlation)

Species i	Species j	$D_{i,j}(m^2/s)$
O_2	Air	$1.74(10^{-5})$
N_2	Air	$1.70(10^{-5})$

4.5 REACTION MECHANISM

Finally, the single-step global reaction mechanism used describes the combustion of Kerosene in the presence of oxygen and corresponds to the following reaction

$$C_{12}H_{23} + 17.75O_2 \Longrightarrow 12CO_2 + 11.5H_2O \tag{4.6}$$

The reaction rate or change in fuel molar concentration per unit time (kmol/(m^3-s)) is given by

$$\frac{d[C_{12}H_{23}]}{dt} = -k_G(T)[C_{12}H_{23}]^{0.25}[O_2]^{1.5} \tag{4.7}$$

where the global rate coefficient $k(T)$ is of the Arrhenius form

$$k(T) = 2.587(10^9)e^{-1.256(10^8)/R_uT} \tag{4.8}$$

Chapter 5

SIMULATIONS

5.1 SIMULATION PROCEDURE

The simulations in this study were conducted by slowly building from simple to more complex models. Specifically, the flow solution was iterated via the following steps

1. Inviscid/incompressible flow solution, (steady flow)
2. Laminar incompressible flow solution, (steady flow)
3. Laminar compressible flow solution, (steady flow)
4. Turbulent compressible flow solution, (steady flow)
5. Turbulent compressible with species transport (no injection/non-reacting), (steady flow)
6. Turbulent compressible with species transport (no injection/non-reacting), (unsteady flow)
7. Turbulent compressible with species transport (with injection/combustion), (steady flow)
8. Turbulent compressible with species transport (with injection/combustion), (unsteady flow)

The simulations where performed in this order not only to increased stability (running the full combustion simulation (even with very low relaxation) always resulted in a diverging solution), but also to decrease the time to convergence and check basic flow conservation and work extraction. Finally, the non-injection cases provided a common starting point for all injection simulations with and without adiabatic foil surfaces. In addition, all

reacting flow simulations were subsequently performed using "time accurate" unsteady computations (to gauge convergence). The extent of convergence was determined by not only examining residuals, but by repeatedly iterating the flow solution until exit flow properties such as local temperature, turbulence intensity and total pressure converged to (essentially) constant quantities. For the unsteady calculation the time step Δt was chosen so as to provide at least 7 steps per blade pass.[1] Specifically, the time required for the free-stream flow to transverse the domain is given by

$$t_{tras} \approx \frac{L_{domain}}{V^{av}_{meridinal}} \approx \frac{L_{domain}}{V^{av}_{x}} \approx \frac{0.32}{90} = 3.5(10^{-3})s \tag{5.1}$$

where V^{av}_{x} is approximated by the inlet x velocity component. The time required per blade pass on the other hand is given by

$$t_{pass} = \frac{H_{domain}}{V_{rotor}} = \frac{0.08}{275} = 2.9(10^{-4})s \tag{5.2}$$

Thus, a time step Δt was chosen as $4(10^{-5})s$ and the number of minimum computational time steps were chosen so as to satisfy (5.1).

5.2 NON-REACTING FLOW

The first results of interest are the non-reacting flow simulations used to test the accuracy of the species transport solution, presence of work extraction via the rotor and correct minimum y^+ values at foil surfaces (to reduce computational effort, a higher y^+ (i.e. a coarser) grid was used for the non-injection surface (e.g. the stator in the case of rotor injection)). Figure 5.1 and Figure 5.2 display total pressure and temperature contours. Note that one interesting anomaly is the localized region of high pressure and temperature near the leading edge of the rotor. Specifically, total pressure and temperature exceed free-stream values by a maximum of approximately 5% (at several gid points near the blade surface). However, at mid-stage total temperature and pressure vary from their (theoretically) constant value by approximately 1.5 % and 0.01% respectively.[2]

[1] Note that decreasing duration of the time step increases the number of steps required for the freestream flow to travel the length of the computational domain.

[2] The values for P_0 and T_0 at mid-stage are 3.442MPa and $1,700.2^{\circ}$K. This result was robust in that the region of high total temperature and pressure persisted even for alternative grid densities.

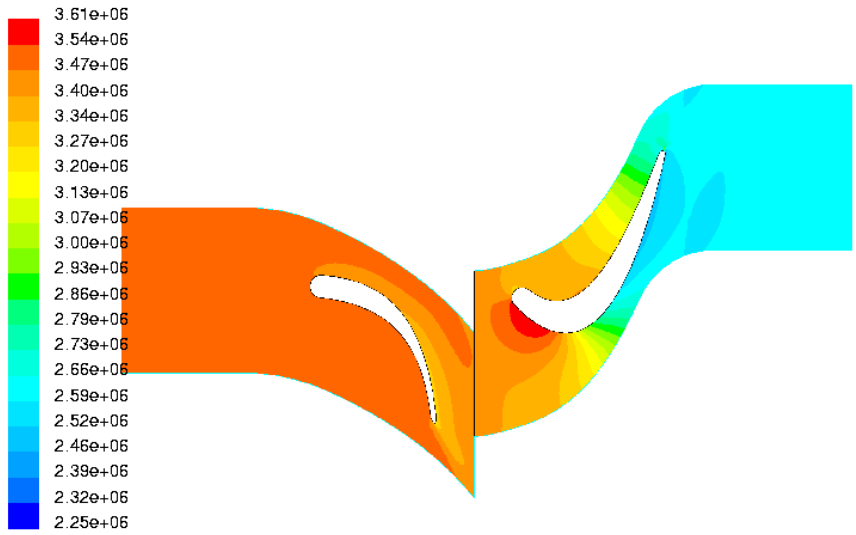

Figure 5.1: Total pressure contours non-injection simulation

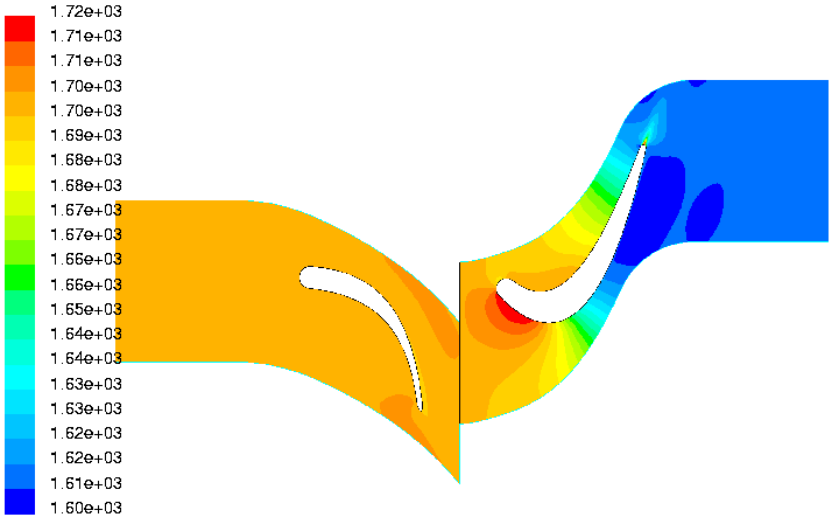

Figure 5.2: Total temperature for non-injection simulation

Flow Mach number is given in Figure 5.3 and varies in the free-stream from 0.1 at the inlet to in excess of 0.5 within the cascade itself. In addition, the flow includes a

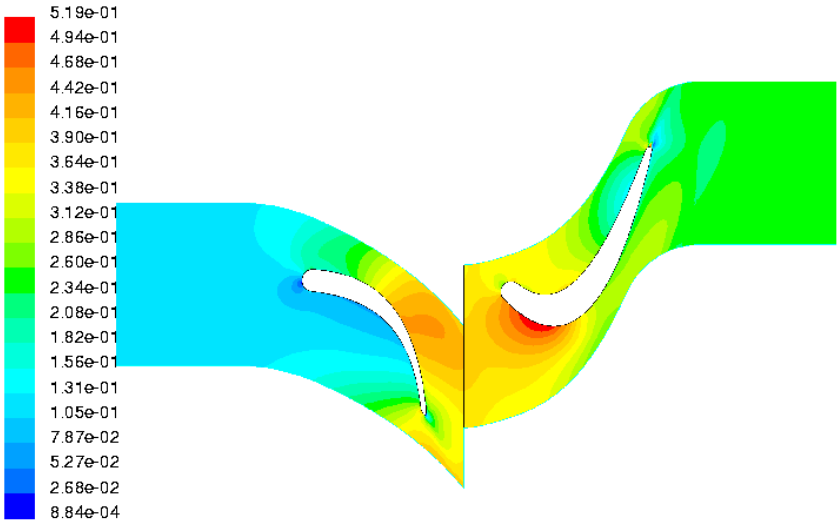

Figure 5.3: Flow Mach number

pressure side separation on the rotor as indicated by the pathlines given in Figure 5.4.[3] In terms of species conservation we see that the O_2 mole fraction is conserved (see Figure 5.5). Finally, to ensure adequate grid quality we note that y^+ values are on the order of one over the foil surface (the stator is displayed for illustrative purposes and the rotor exhibits similar values) as displayed in Figure 5.6. Inlet and outlet flow properties are given in Table 5.1.[4]

Table 5.1: Inlet and exit flow properties for non-reacting flow case

Sim. type	$v_{inlet}(m^3)$	$v_{outlet}(m^3)$	P_{inlet}(MPa)	P_{outlet}(MPa)	$T^{\circ}_{inlet}K$	$T^{\circ}_{outlet}K$	$\dot{m}$ (kg/m)
Unst.-ad.	0.1375	0.1776	3.464	2.50	1,696.23	1,597.4	57.27
Unst.-nonad.	0.1375	0.17761	3.4645	2.50	1,696.20	1,556.1	57.8

The first item to note is the reduction in local temperature at the outlet due primarily to work extraction (total temperature also decreased by approximately $100^{\circ}K$ (see Figure

[3] In the case of fully laminar flow both the rotor and stator exhibited gross separation.

[4] The nomenclature used here is "st" (steady), "ad" (adiabatic wall) and "nonad" (isothermal wall).

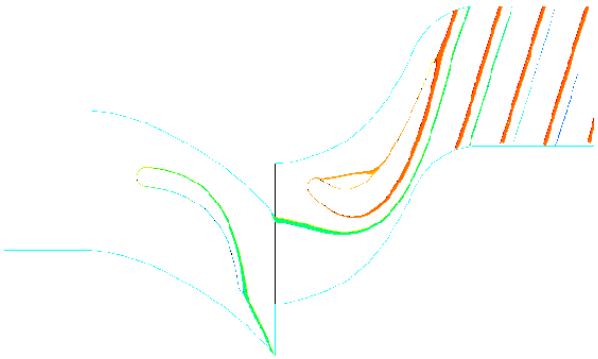

Figure 5.4: Pathlines indicating pressure side rotor blade separation

5.2)). In addition, the non-adiabatic case (i.e. isothermal foil surfaces at $1,000^{\circ}K$) exhibits an increase in flow rate due, presumably, to the decrease in average viscosity of the fluid near the wall. Indeed, for air absolute viscosity increases with temperature.

We can describe the overall process by calculating the polytropic exponent n according to

$$P_{inlet}v_{inlet}^{n} = P_{outlet}v_{outlet}^{n} \tag{5.3}$$

and (in the adiabatic case) a polytropic efficiency η via the following

$$\eta = \frac{n-1}{n} / \frac{\overline{\gamma}-1}{\overline{\gamma}} \tag{5.4}$$

where $\overline{\gamma}$ is the average of the flow inlet and outlet values.[5]

Table 5.2: Inlet and exit flow properties for non-reacting flow case

Simulation type	n	$\overline{\gamma}$	η_{poly}
Unsteady-ad.	1.274	1.2859	0.9672
Unsteady-nonad.	1.3587	1.2881	

The polytropic exponent is useful in that it may be specified in a cycle deck to describe the work extraction process taking place for a complete stage.

[5] γ is defined at the ratio of specific heats C_p/C_v.

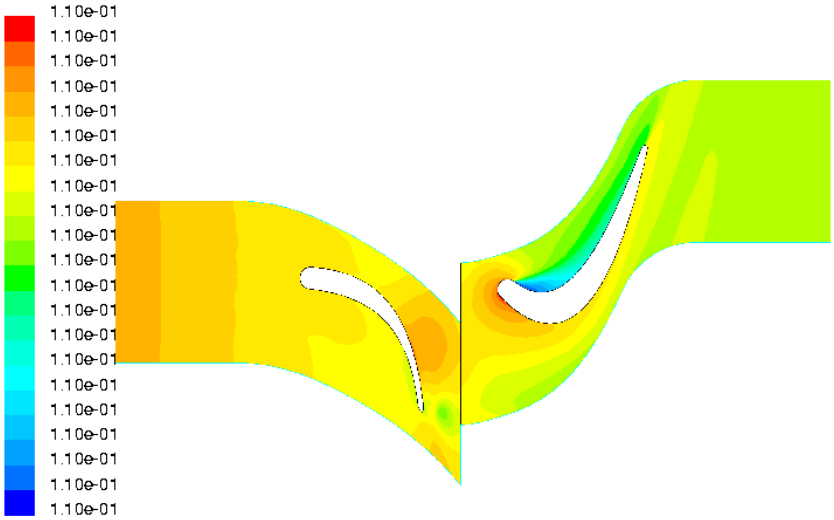

Figure 5.5: Contours of y_{o_2} for no injection

Of interest is also the rate of work extraction which can be directly calculated using the expression

$$\dot{W} = \vec{F}_{blade} \cdot \vec{V}_{blade} = F_{y,blade} \|\vec{V}_{blade}\| \tag{5.5}$$

The required quantities for calculating work extraction are give in Table 5.3.[6]

Table 5.3: Rotor foil velocity, force and work extraction for non-reaction flow

Simulation type	$\|\vec{V}_{blade}\|$ (m/s)	$F_{y,rotor}$ (kN/m)	$\dot{W}$ (MW/m)
Unsteady-ad.	275	-24.02	6.61
Unsteady-nonad.	275	-24.36	6.70

Again, note that due to the increased mass flow rate for the non-adiabatic foils there is an increase in force applied to the blades in the y-direction and hence an increase in power extracted by the rotor.

Finally, of interest here is arriving at an estimate of the required heat addition and hence fuel injection to yield an isothermal process.

[6]The units given for force and power are *per unit width* since the simulation is 2-dimensional.

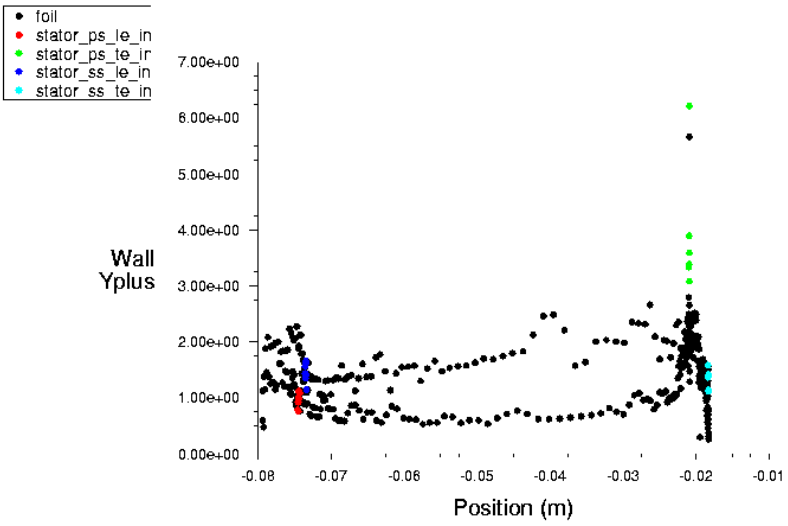

Figure 5.6: y^+ for stator

Specifically, for the non-reacting case we have from the energy balance (neglecting shear work, heat transfer and elevation change)[7]

$$q - w = \Delta h_0 \Rightarrow |w| = |\Delta h_0| = |\Delta h(T) + \Delta \frac{\vec{V}^2}{2}| \tag{5.6}$$

Thus, in order to produce zero net change in local temperature the required heat addition and fuel mass flow can be expressed as

$$-\Delta h(T) = q_{required} \Rightarrow \dot{m}_{fuel} = \dot{m} \frac{q_{required}}{HHV_{fuel}} = \dot{m} \frac{|-\Delta h(T)|}{HHV_{fuel}} =$$

$$\dot{m} \frac{h_{inlet} - h_{outlet}}{HHV_{fuel}} = 57.32 \frac{1,654 - 1,526}{47,841} = 0.154(\frac{kg}{s}) \tag{5.7}$$

where HHV is the higher heating value of the fuel.[8] Note, that this result is a minimum given heat addition will accelerate the flow and result in a lower local temperature (via an increase in the Mach number). It should also be restated that we are modeling the injection of Kerosene vapor (as opposed to liquid or droplet injection).

[7] Note that work calculated via the energy balance was in excellent agreement with the method employed in the previous expression.

[8] The heating value used is for that of Dodecane ($C_{12}H_{26}$) vapor.

5.3 REACTING FLOW (ARRHENIUS KINETICS/EDDY-DISSIPATION)

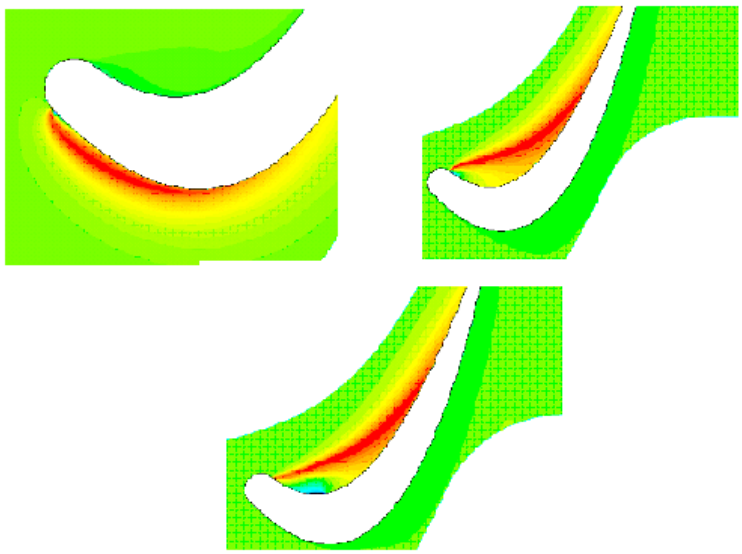

Figure 5.7: T profiles for rotor injection

Fuel was injected from seven locations: two at the leading and trailing edge of the stator as well as two leading edge and one mid-span injection point on the rotor. The results from the laminar combustion case as well as the eddy-dissipation model indicate that combustion is self-igniting and self-sustaining for all injection points. Figure 5.7 illustrates temperature contours for the rotor injection points (leading edge suction and pressure side injection along with pressure side recirculation zone injection (lower image)). Figure 5.8 displays the same for the stator injection points. For the purpose of demonstrating that fuel is indeed being consumed the mole fraction contours for water vapor y_{h_2O} are given in Figure 5.9 and clearly show the vapor component of the flow is minimized at the point of injection (approximately in the middle of the figure on the pressure side of the foil), whereupon y_{h_2O} increases to a maximum value within the recirculaton zone and wake. Diffusion into the freestream subsequently occurs thereafter.

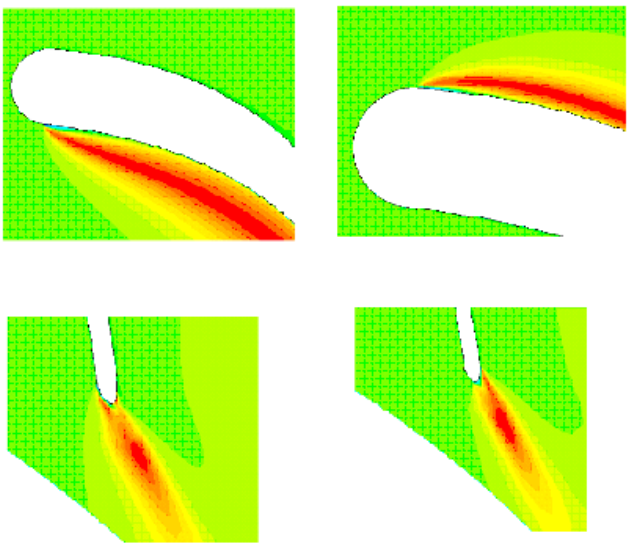

Figure 5.8: T for stator injection

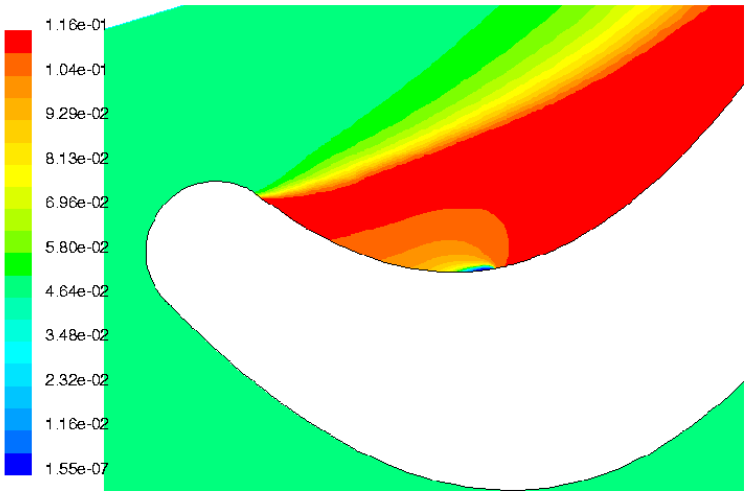

Figure 5.9: y_{H2O} for mid-rotor injection

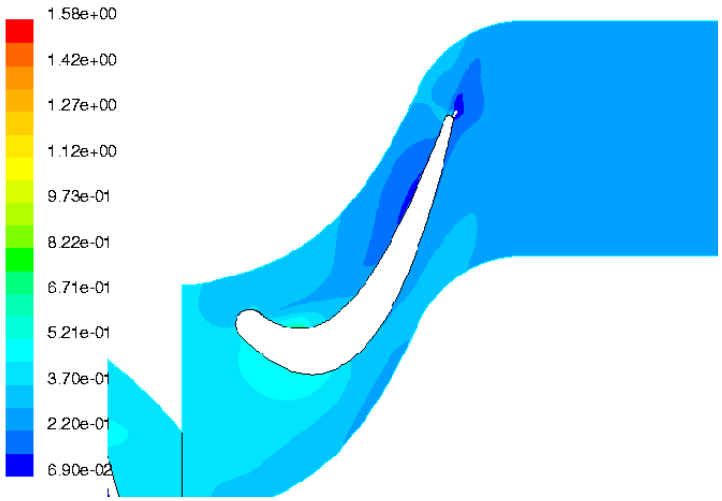

Figure 5.10: Ma for mid-rotor injection

The Mach number profiles are given in Figure 5.10. Two items of interest are the fact that the introduction of cold fuel at a temperature of $600^{\circ}K$ (compared with the main flow which is at approximately $1700^{\circ}K$) produces a high local Mach number about the point of injection. This is due simply to the fact that the local speed of sound is proportional to $T^{1/2}$. In addition, the combustion process tends to drive the Mach number (downstream of the injection point) towards the sonic-point. This should not be surprising since any heat addition process will, in general, drive the Mach number towards unity. Specifically, the exit Ma for injection and non-injection cases are 0.26 and 0.24. Finally, combustion is also demonstrated by examining the fuel concentrations over the computational domain. Specifically, Figure 5.11 illustrates the mole fraction of fuel $y_{C_{12}H_{23}}$. From the figure we can see that the fuel, after being injected, travels upstream of the main flow (the flow is locally moving clockwise in the recirculation zone) and subsequently dispersed and consumed within the recirculation zone. Various stage inlet and outlet flow quantities are given as in the non-reaction case.

Table 5.4: Inlet and exit flow properties for reacting flow case (rotor mid injection)

Sim. type	$v_{inlet}(m^3)$	$v_{outlet}(m^3)$	P_{inlet}(MPa)	P_{outlet}(MPa)	$T^{\circ}_{inlet}K$	$T^{\circ}_{outlet}K$	$\dot{m}$ (kg/m)
Unst.-ad.	0.13752	0.1881	3.465	2.50	1,696.4	1,692.1	56.3
Unst.-nonad.	0.1375	0.1844	3.465	2.50	1,696.4	1,658.8	56.7

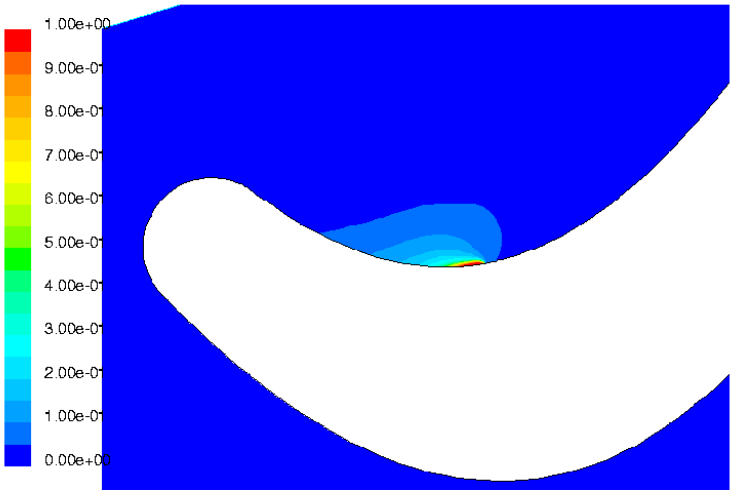

Figure 5.11: $y_{C_{12}H_{23}}$ for mid rotor injection

As we can see, the process is now essentially isothermal for the complete stage. In addition the mass flow rate of fuel $\dot{m}_{fuel}$ can be calculated via

$$\dot{m}_{fuel} = \Delta\dot{m}_{CO_2}\frac{m_{fuel}}{m_{CO_2}} = \dot{m}_{CO_2}\frac{N_{fuel}}{N_{CO_2}}\frac{MW_{fuel}}{MW_{CO_2}} \cong 0.31\ \dot{m}\ \Delta\chi_{CO2} \tag{5.8}$$

where the Δ's refer to the difference between stage inlet and outlet. From the previous we can calculate a process polytropic exponent n as in the non-reaction case as well as the fuel injection rate.

Table 5.5: Fuel mass flow $\dot{m}_{fuel}$ and polytropic exponent n (rotor mid injection)

Sim. type	n	$\dot{m}_{fuel}$ (kg/s)
Unst.-ad.	1.042	0.1733
Unst.-nonad.	1.108	0.1698

Eddy-Dissipation results were nearly identical to the laminar combustion cases in terms of peak flame temperature and flame structure (see Appendix F). Leading edge pressure and suction side injection bulk flow results were also similar to the mid-rotor pressure side injection and are given in Appendix F.

5.4 TURBULENT COMBUSTION (CONSERVED SCALAR) SIMULATIONS

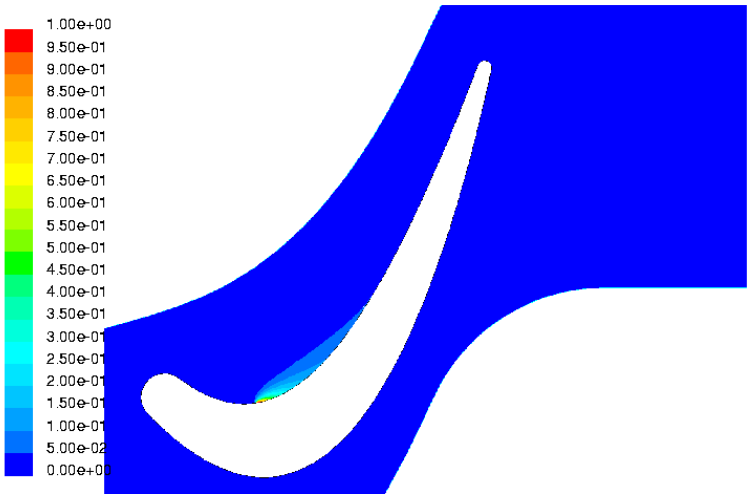

Figure 5.12: Conserved scalar f for mid rotor injection (adiabatic foil)

The results for the turbulent combustion simulations based on a conserved scalar approach are given as follows.[9] A contour plot showing the distribution for the scalar f is given in Figure 5.12 indicating (for mid pressure side injection) the introduction of fuel material on the pressure side of the foil. Conversely, Figure 5.13 shows the increase in χ_{H_2O} in the freestream. Temperature profiles are given in Figure 5.14 and show a substantially reduced peak flame temperature of about $2,010^\circ K$ as opposed to a value of approximately $2,700^\circ K$ for the laminar and eddy-viscosity case.[10] In fact, all rotor simulations yielded substantially lower peak combustion temperatures (see Appendix F). An additional point of interest to make is that the PDF calculation did not yield a pressure side separation as indicated by the pathlines shown in Figure 5.15. A possible explanation for this may be that the separation is weak, thus slight variations in property calculation methods may result in reattachment of the flow.[11]

[9] Fluid properties such as μ and k are assumed for the PDF method, thus the values of viscosity and thermal conductivity were set to their approximate values at mid-stage ($5.5(10^{-5})$ and $0.0093(w/m-K)$ respectively via the previous laminar combustion case).

[10] Laminar combustion simulations are known to chronically overpredict peak flame temperatures in turbulent flow. Thus, this result comes as no surprise.

[11] The PDF method assumes constant fluid properties μ, k, etc.

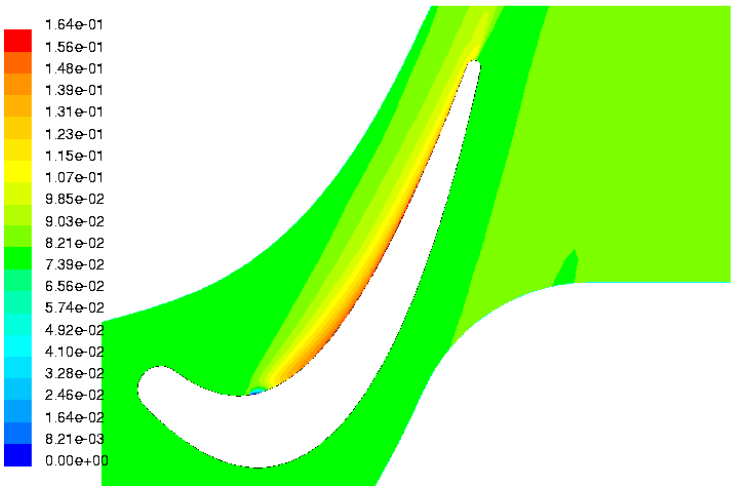

Figure 5.13: χ_{H_2O} for mid rotor injection (adiabatic foil)

5.5 STATOR SIMULATIONS

Given the similarity of the stator and rotor injection simulations only a few illustrative figures are given to demonstrate the presence of combustion. Specifically, Figures 5.17 and 5.16 display the static temperature rise associated with combustion on the stator foil region. It should be stated that diffuculties were encountered in arriving at consistent predictions between the stator and rotor PDF simulations. Specifically, the stator injection cases yielded a much higher peak combustion temperature (similar to the laminar and eddy-dissipation model) than those of the rotor. Recall that the results for rotor combustion yielded peak temperatures of approximately $2,000^{\circ}K$, while stator PDF combustion results gives a peak temperature of close to $2,700^{\circ}K$. In addition, the stage outlet temperatures were not consistent between stator and rotor injection nor was there a reasonable correlation between fuel injection and the overall stage temperature rise.

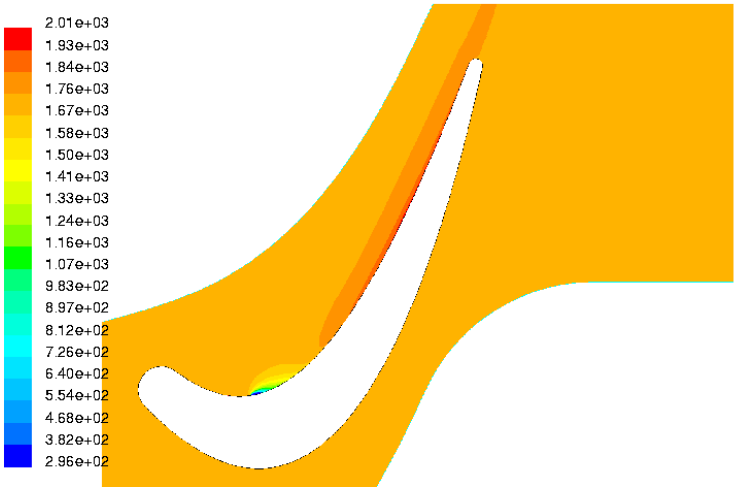

Figure 5.14: Temperature for mid rotor injection (adiabatic foil)

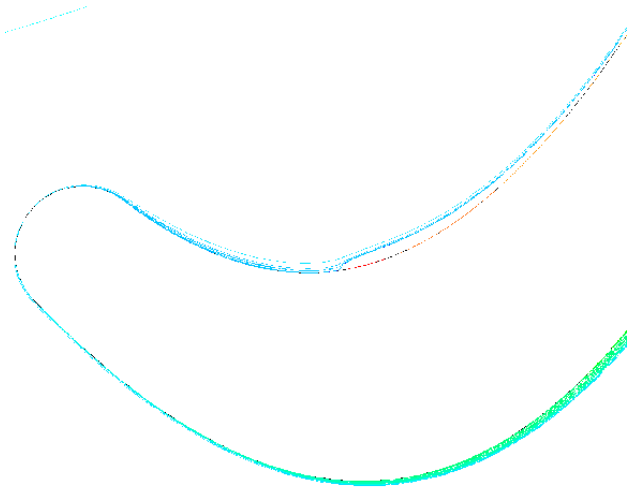

Figure 5.15: Pathlines for mid rotor injection (PDF adiabatic foil)

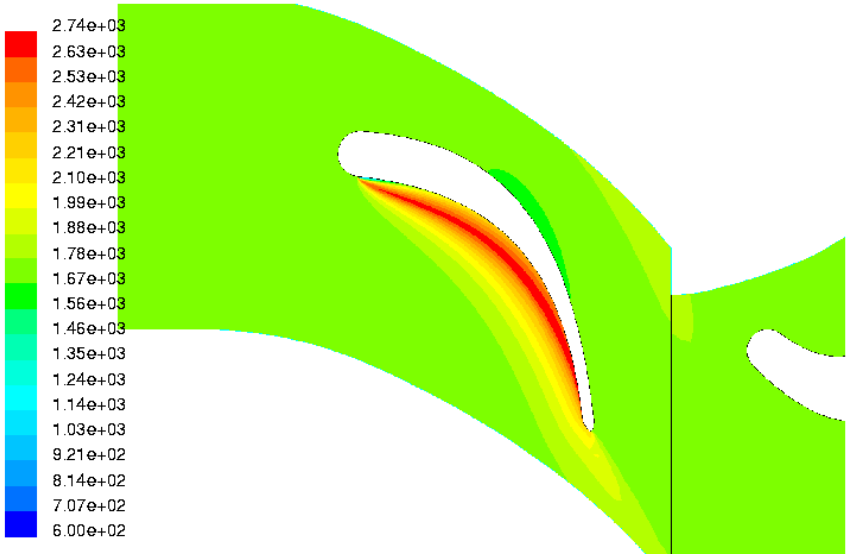

Figure 5.16: Temperature contours for laminar leading edge pressure side injection (leps) (adiabatic foil)

Figure 5.17: Temperature contours for eddy-dissipation trailing edge suction side injection (nonadiabatic foil)

Chapter 6

RESULTS AND DISCUSSION

Given that the results do not exclude the possibility of combustion in a turbine we can now turn our attention to some of the other questions at hand. Namely, *what are the benefits and drawbacks of the different combustion/injection schemes in terms of*

1. Deterioration of aerodynamic performance
2. Blade heat transfer
3. Transverse temperature variations (pattern factors)
4. Axial temperature variation (i.e. how isothermal is the combustion process).

6.1 PRESSURE DISTRIBUTIONS

Table 6.1: Net pressure force on rotor blade for different injection methods (laminar combustion)

Simulation type	$F^y_{pressure}$ (kN)
No Injection	23.82
Leading edge suct. side	23.59
Leading edge pres. side	23.92
Mid-span pres. side	24.15

Given the various locations for fuel injection it is of interest as to which fuel injection scheme results in the least disruption of the flow (in an aerodynamic sense). A first indication of the effect of injection location on aerodynamic performance is the net force on

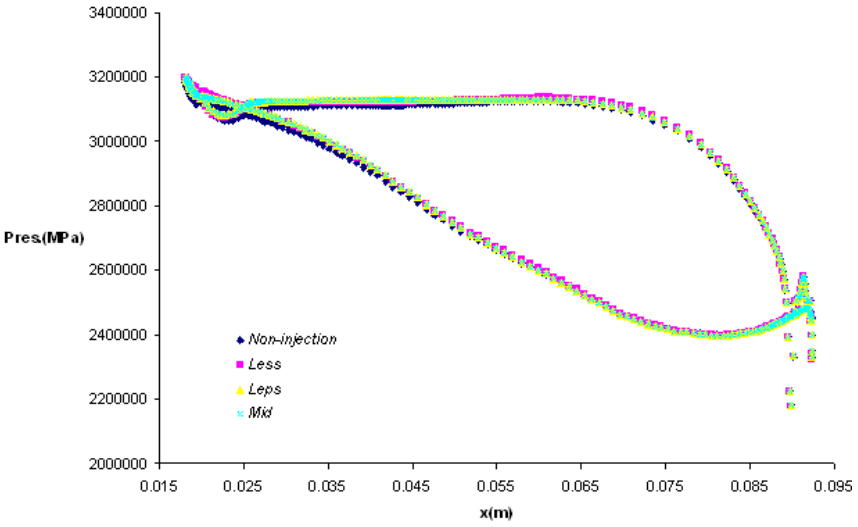

Figure 6.1: Rotor pressure distribution for various injection locations (laminary combustion)

the blade (Table 6.1).[1] From the table we can see that the choice of injection configuation has very little effect on blade force and hence work extraction (these force calculations were made over one full blade pass) although there would appear to be some minor advantage to pressure side injection as indicated by the slight higher blade force for pressure side fuel injection.[2] This relative invariance (at least for the temperature rises present in these simulations) can be seen by superimposing blade pressure distribution for the various injection schemes (Figure 6.1). From the figure we can see that indeed the pressure distributions are largely identical. However, a more illustrative plot is of the percentage deviation in pressure from the non-injection case as shown in Figure 6.2.[3] From the figure we see that the injection of fuel has the effect of reducing foil surface pressure (via the addition of heat accelerating the flow). Specifically, surface pressure for the combustion cases match those for non-combustion at two spatial locations: the leading edge (at the stagnation point (to the left)) and at the trailing edge where the flow ceases to turn and local static pressure is determined by the exit boundary condition (the same for all cases). However, immediately downstream of the leading edge stagnation point, pressure is less than the non-combustioning case (again due to the expansion of the hot

[1] These results were from the laminar combustion simulations.

[2] A FORTAN program was written to read, extract and combine pressure plot information from multiple files.

[3] Note that as in the blade force calculations, these profiles are time-averages over one blade pass.

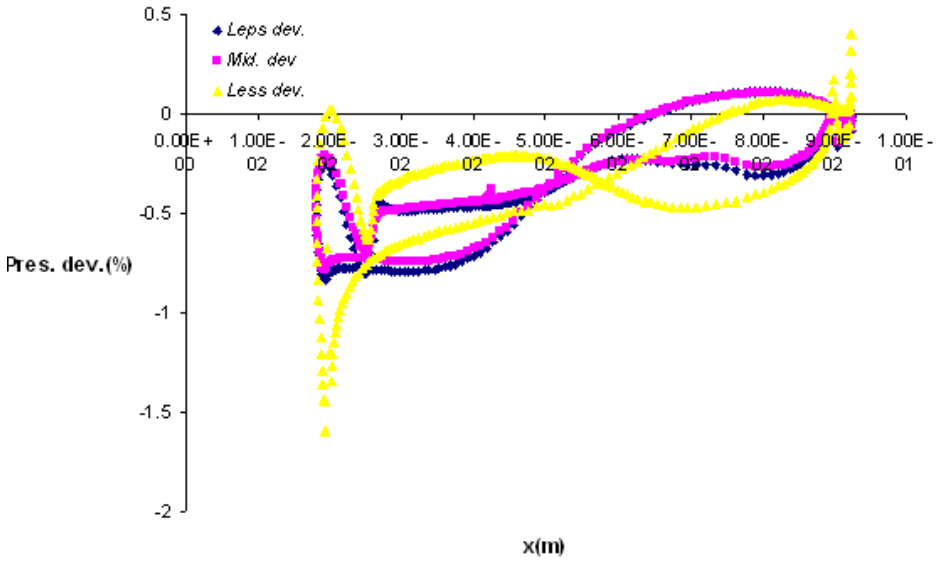

Figure 6.2: Rotor pressure variation for various injection locations

gases and acceleration of the flow). Of interest is the qualitative difference between the maximum pressure deviation in that the leading edge suction side injection case has the greatest (negative) deviation, indicative of strong acceleration near the point of injection (compared to pressure side injection where separation-induced mixing tends to moderate the temperature rise of the flow).[4] Hence, mixing due to the pressure side separation tends to moderate any differences between surface pressure distributions for the leading edge pressure side and mid-injection cases (both utilizing injection of the pressure side of the blade). This can be seen by noting that the leading edge and mid-injection cases exhibit almost identical pressure deviations from the non-combustion case.

6.2 HEAT TRANSFER

In assessing the respective merits and deficiencies of various injection schemes we are also interested in the potential impact of heat transfer on blade durability. Specifically, one would expect that given the enhanced mixing associated with the pressure side injection (due to the recirculation zone), heat transfer would be less pronounced on the pressure than on the suction side. This is indeed the case as illustrated via the plot of surface

[4]The figure can be viewed as follows: The leading edge (on the left) begins at an x distance of approximately 0.02(m). The curve of minimum (absolute) pressure deviation proceeding downstream represents the pressure side, while at the point of inflection the suction side exhibits the minimum (absolute) pressure deviation.

heat flux (Figure 6.3). Specifically, while the pressure side injection cases exhibit their maximum heat transfer at the trailing edge (resulting presumably from enhanced mixing at the trailing edge separation point (due to the thickness of the blade)), suction side combustion yields a much higher heat transfer rate forward of mid-span. This is due to the fact that on the pressure side gradients are much lower than on the suction side (which does not contain a separation bubble). Note, it is not approriate to refer to a "boundary layer" as such given that near the point of combustion heat is not being transferred from the freestream (or the blade) to the blade (or free-stream). Specifically, the maximum gas temperature must be attained *within* the boundary layer (not at the surface or the freestream). Also the acceleration of the flow on the suction side increases the convective transport (of energy), thus yielding a higher heat transfer rate on the suction side (the analogy for boundary layers here would be a relatively high heat transfer coefficient h on the suction side of the blade (in comparison to the pressure side)).

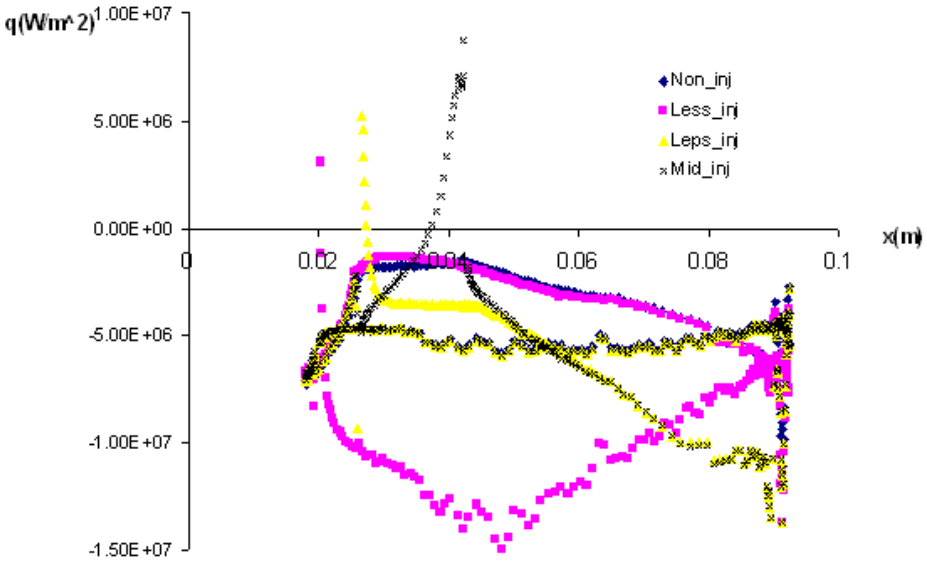

Figure 6.3: Heat transfer q'' for various injection schemes

6.3 PATTERN FACTORS

Of interest is not only heat transfer to the blades, but the effect of combustion on the foil wake temperature distibution.[5] Specfically, Figure 6.4 illustrates the cross-stream

[5]Temperature non-uniformity due to foil boundary-layer combustion will affect component durability downstream of the combustion zone (e.g. blades in the following stage).

temperature distribution just down-stream of the stator trailing edge. Hence, we define

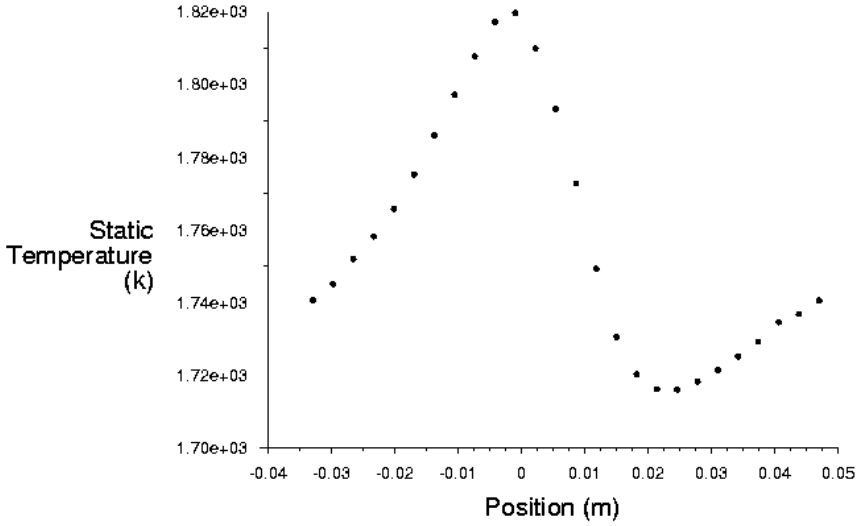

Figure 6.4: Cross-stream temperature distibution 1/4 cord down-stream of stator (adiabatic non-combustion)

two *pattern factors* as follows

$$\text{Pattern Factor} \equiv \frac{T_{max} - T_{mean}}{\Delta T_{foil}} \tag{6.1}$$

$$\overline{\text{Pattern Factor}} \equiv \frac{T_{max} - T_{min}}{\Delta T_{foil}} \tag{6.2}$$

where T_{mean} is the temperature profile mean value at the rotor exit plane (or stator exit if we are interested in pattern factors for the stator) approximately a quarter cord length downstream of the blade trailing edge. Note that temperature difference in the numerator is normalized via the quantity ΔT_{foil} which is taken to be the rotor or stator local temperature drop from leading to trailing edge for the non-reacting case.

The calculated pattern factors are given in Table 6.2

Table 6.2: Calculated pattern factors (laminar rotor adiabatic wall injection)

Injection location	PF	$\overline{PF}$
No Injection	0.05	0.10
LEPS Injection	0.34	0.61
Mid Injection	0.40	0.61
LESS Injection	0.24	0.44

These results indicate that not only does combustion on the foil increase the pattern factor (in comparison to the case without fuel injection), but combustion on the pressure side of the foil lends itself to higher pattern factors than combustion on the suction side. The reason for this can be readily seen by viewing a contour plot of static temperature about the rotor for the injectionless case (Figure 6.5). Specifically, we see that the ex-

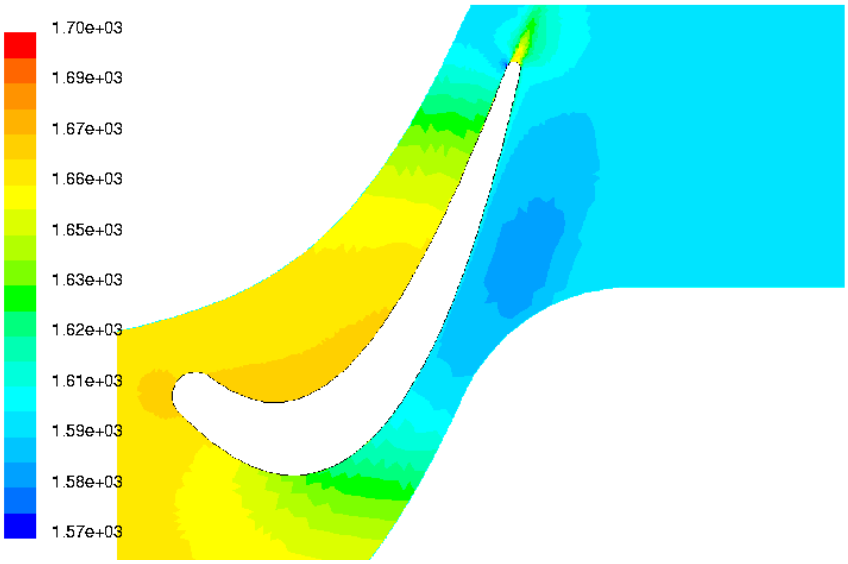

Figure 6.5: Temperature contours about rotor for non-injection case

pansion process for the flow takes place on the suction side, resulting in relatively high temperatures on the pressure side. As the flow proceeds downstream towards the trailing edge and beyond, there is recompression on the suction side, heat transfer and fluid mixing between the relatively hot pressure side flow and the cool suction side fluid. Thus, heat

addition on the pressure side would accentuate the temperature difference between the suction side and pressure side fluid, hence, increasing the value of the pattern factor.

Similarly, for the stator injection cases we have the result that injection further upstream (i.e. at the leading edge of the blade) is best for minimizing the pattern factor. This is reasonable since overall diffusion of the hot product gases into the freestream is enhanced by the longer travel distance. These results can be seen from Table 6.3.[6]

Table 6.3: Calculated pattern factors (laminar stator adiabatic wall injection)

Injection location	PF	$\overline{PF}$
non injection	0.142	0.285
less	1.42	2.43
leps	1.25	2.45
tess	3.65	5.51
teps	3.14	4.42

Unlike in the case of rotor injection (where work extraction is taking place by expansion on the suction side of the foil) we see no disadvantage in burning fuel on the pressure side in terms of lowering the pattern factor.

6.4 ISOTHERMAL COMBUSTION

Given that the goal is to determine the most advantageous scheme for instigating isothermal combustion, we continue by looking at the axial (x-direction) temperature distribution for the various injection schemes. Specifically, one would presume that given low enough Mach numbers, it would make sense to burn fuel at or near the point of work extraction (i.e. on the rotor). This apparently is the case as displayed in Figure 6.6. Specifically, we see that stator injection results in a (mass) flow averaged peak temperature of approximately $1,770^{\circ}K$ at mid-stage resulting in a temperature departure of about $100^{\circ}K$. In contrast, rotor injection results in a minimum temperature of approximately $1,670^{\circ}K$ (also at mid-stage) and a temperature departure (from the mean inlet) of only about $30^{\circ}K$; a significant improvement over the stator injection results. However, it should be noted that for high Mach number flows (where velocity is high and local temperatures are low at mid-stage) stator combustion may provide a more uniform axial temperature distribution.

[6]Note that the normalization temperature ΔT_{foil} is much smaller for the stator case. Hence, direct comparisons between rotor and stator pattern factors are meaningless.

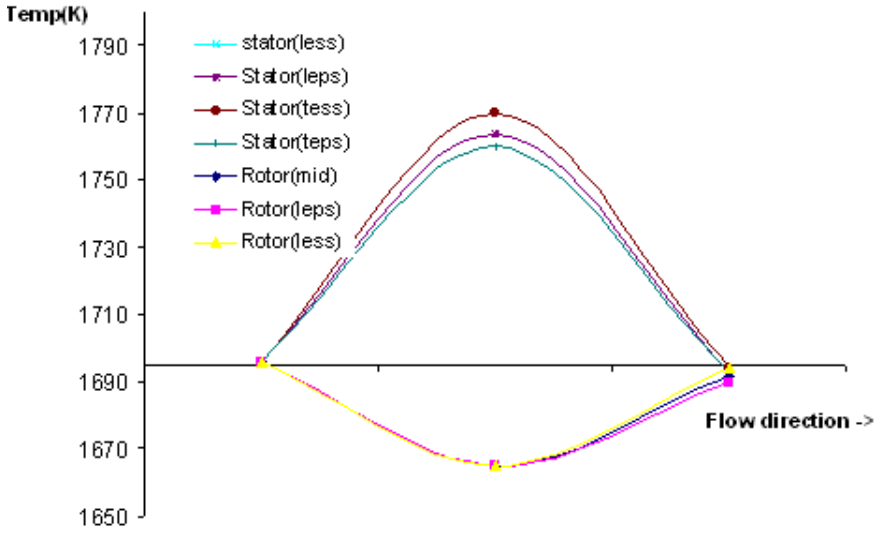

Figure 6.6: Axial local temperature distribution for various injection schemes

6.5 CYCLE ENHANCEMENTS

6.5.1 IDENTICAL OVERALL PRESSURE RATIOS

A suitable comparison can be made (see Figure 6.7) between the Hybrid cycle operating over the closed path $1 \rightarrow 2 \rightarrow 3' \rightarrow 3 \rightarrow 4 \rightarrow 1$, an intermediate cycle operating over $1 \rightarrow 2 \rightarrow 3' \rightarrow 3''' \rightarrow 4''' \rightarrow 1$ and the equivalent Brayton cycle $1 \rightarrow 2 \rightarrow 3' \rightarrow 3'' \rightarrow 4'' \rightarrow 1$, where the processes $1 \rightarrow 2$, $3'' \rightarrow 4''$, $3 \rightarrow 4$ and $3''' \rightarrow 4'''$ are assumed isentropic. In addition , simulation data exists for the paths $3' \rightarrow 3$, $3' \rightarrow 3'''$ and $3' \rightarrow 3''$ (corresponding to the combustion, and non-combustion cases respectively).[7] Hence, the expressions for net specific turbine work for the Brayton cycle is (assuming we can neglect compressible effects)

$$w_{net}^{Brayton} \simeq \frac{F_y|\vec{V}_{blade}|}{\dot{m}} + C_P^{average}(T_{3''} - T_{4''}) - w_{comp} \tag{6.3}$$

the hybrid cycle

$$w_{net}^{Hybrid} \simeq \frac{F_y|\vec{V}_{blade}|}{\dot{m}} + C_P^{average}(T_3 - T_4) - w_{comp} \tag{6.4}$$

[7] A reduced fuel injection simulation was conducted to give results for an intermediate non-isothermal heat addition case.

and for an intermediate heat addition cycle

$$w_{net}^{Intermediate} \simeq \frac{F_y|\vec{V}_{blade}|}{\dot{m}} + C_P^{average}(T_{3'''} - T_{4'''}) - w_{comp} \tag{6.5}$$

where w_{comp} is the isentropic compressor specific work $w_{1\to 2}$. In addition, thermal effi-

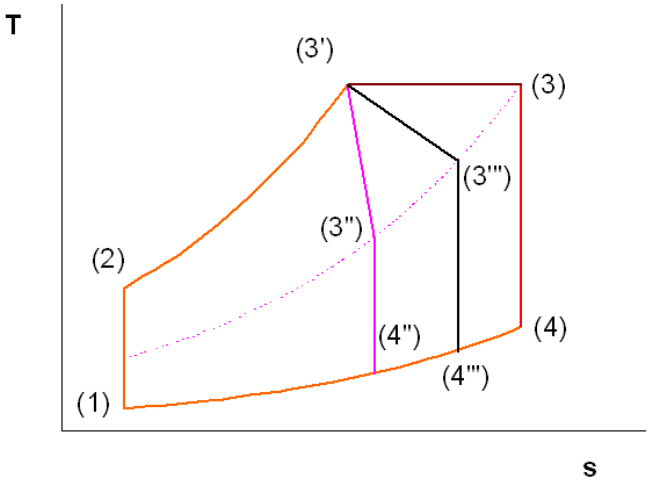

Figure 6.7: T-s diagram for cycle comparisons

ciency for the Brayton, Hybrid and Intermediate cycle can be expresses as (see Appendix C)

$$\eta_{Brayton} = \frac{w_{net}}{q_{in}} = \frac{w_{net}}{q_{2\to 3'}} \tag{6.6}$$

$$\eta_{Intermediate} = \frac{w_{net}}{q_{in}} = \frac{w_{net}}{q_{2\to 3'} + q_{3'\to 3'''}} \tag{6.7}$$

$$\eta_{Hybrid} = \frac{w_{net}}{q_{in}} = \frac{w_{net}}{q_{2\to 3'} + q_{3'\to 3}} \tag{6.8}$$

where $q_{2\to 3'}$ is the combustor heat addition for process $2 \to 3^{'}$, $q_{3'\to 3}$ is the *approximately* isothermal heat addition associated with the simulated process $3^{'} \to 3$ and $q_{3'\to 3}$ is the heat addition for a non-isothermal combustion process (reduced fuel injection) $3^{'} \to 3^{'''}$.[8] Calculating the above quantities assuming *pseudo* constant specific heats while neglecting Mach number effects yields the following net work and thermal efficiencies (Table 6.4)

[8] A separate simulation was conducted for this reduced fuel injection (non-isothermal) case (data is presented in Appendix F).

Table 6.4: Values for $\eta_{simulation}$, $\eta_{theoretical}$ and w_{net}

Simulation	$\eta_{simulation}$	$\eta_{theoretical}$	w_{net} (kJ/kg)
Brayton	0.607	0.623	636.9
Hybrid	0.579	0.612	691.3
Intermediate	0.588	–	660.8

Note, as expected, a machine utilizing isothermal combustion, when compared with a Brayton machine having identical overall pressure and temperature ratios, produces more work.

6.5.2 NON-CONSTANT OVERALL PRESSURE RATIO

If we instead not only hold the overall temperature ratio constant, but set the Hybrid cutoff pressure P_4 equal to that of the turbine inlet temperature of a Brayton cycle we see the enharent advantage of the Hybrid cycle. Specifically, the *psuedo* simulated Brayton cycle

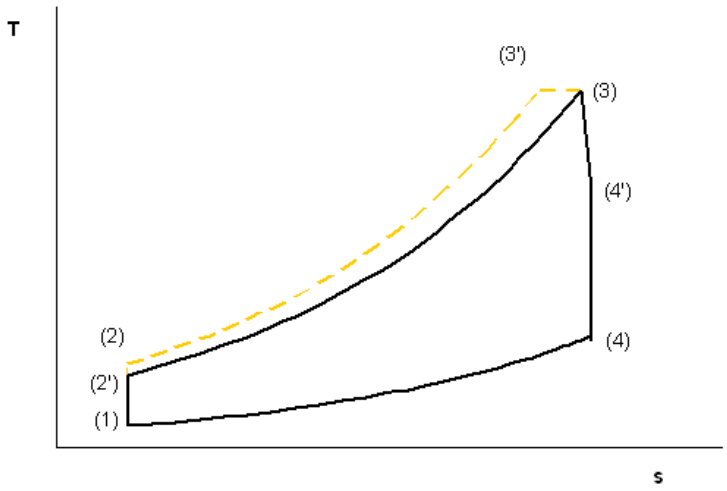

Figure 6.8: T-s diagram for Hybrid (yellow) and Brayton cycle (black) for equal peak temperatures and isothermal cutoff/Brayton turbine inlet pressures

$1 \to 2' \to 3 \to 4' \to 4 \to 1$ can be compared with the Hybrid equivalent $1 \to 2 \to 3' \to 3 \to 4' \to 4 \to 1$.[9] The calculated efficiency and specific net work for this high pressure

[9]Where the simulation results apply to the sub-processes $3' \to 3 \to 4'$ and $3 \to 4'$.

Hybird cycle (again based on *pseudo* simulation data) is 61% and 674(kJ/kg) respectively. Recall that the efficiency and specific net output for the equivalent Brayton cycle case are 60.7% and 636(kJ/kg). Hence, the Hybrid cycle indeed presents, under certain conditions, an absolute advantage in terms of efficiency and power over a Brayton machine. Thus, in the case of fixed overall temperature ratios the Hybrid cycle can produce more work at a higher efficiency than the corresponding equivalent Brayton cycle (as depicted in Figure 6.8).[10]

[10]Indeed via the expression for Brayton cycle specific output (1.2) we find that $\left.\frac{\partial W^*}{\partial \tau_c}\right|_{\tau_\lambda}$ takes on a value of -0.32 for values of τ_c and τ_λ corresponding to a hypothetical high-pressure Brayton cycle with pressure ratio π and a peak temperature of 46.57 and $1,700^\circ$K respectively. Hence, a high-pressure Brayton cycle will produce less work, but exhibit a higher thermal efficiency (found to be 65.2% via 1.1) than the comparable Hybrid or low-pressure Brayton machine. Thus, the advantage of the Hybrid cycle in producing more work *as well as* exhibiting a higher efficiency for increasing pressure ratios is demonstrated.

Chapter 7

CONCLUSION

7.1 SUMMARY

A number of simulations using a generic *turbine-like* geometry under *turbine-like* conditions has been performed using a single-step global reaction mechanism. The simulation results indicate that boundary layer combustion is self-igniting and self-sustaining under the representative flow conditions. The simulations indicate that heat transfer to the foil surfaces is mimimized when injection takes place in a recirculation zone. Pattern factors also appear to be minimized when combustion occurs on the suction side of the foil (for rotor injection only). In addition, pattern factors are minimized when injection takes place near the leading edge of the foil. The flow itself remains the most "isothermal" if combustion takes place at the surface of work extraction (on the rotor foil). Also, there appears to be little aerodynamic advantage or penalty associated with the different injection schemes (at least for the rates of heat addition exhibited by the simulations used in this study). Finally, after conducting a "pseudo-simulation" of a cycle incorporating isothermal combustion and comparing to the equivalent Brayton machine, we find that isothermal combustion yields, at the least, an increase in engine specific work and hence power. Specifically, given a fixed overall temperature ratio, isothermal combustion (even in the form of a Hybrid cycle) affords the opportunity to enhance output and efficiency over the "traditional" Brayton cycle.

7.2 RECOMMENDATIONS FOR FUTURE WORK

Although this study has answered some of the fundamental questions regarding the feasibility of isothermal combustion in turbines, a number of opportunities can, and should be pursued. These include, but are not limited, to the following:

1. Foil optimization study to assess (with improved accuracy) the extent to which boundary-layer combustion results in airfoil aerodynamic deterioration
2. Three dimensional simulations investigating the effect of swirl induced reaction rate enhancement in the case of isothermal combustion
3. Assesment of other reaction mechanisms such as multi-step (laminar/Eddy-Dissipation) global reactions
4. Assesment of the effect of radiative energy transfer on the previous results
5. Full turbine (multi-stage) simulations to verify performance improvements associated with isothermal combustion

Appendix A

HYBRID CYCLE PARAMETERS

To derive the Hybrid cycle efficiency and specific output we start by describing the new cycle as depicted in Figure A.1. Specifically, this cycle is composed of the following processes

1. Isentropic compression, $(1 \rightarrow 2' \rightarrow 2)$
2. Isobaric heat addition (in combustor), $(2 \rightarrow 3)$
3. Isothermal heat addition (heat addition in turbine), $(3 \rightarrow 4)$
4. Isentropic expansion (work extraction in turbine (no combustion)), $(4 \rightarrow 5)$
5. Isobaric heat rejection (to the ambient), $(5 \rightarrow 1)$

The expression for thermal efficiency η for this new hybrid cycle can be found, beginning with the general expression

$$\eta_{Hybrid} = \frac{w_{net}}{q_{in}} = 1 - \frac{q_{out}}{q_{in}} \tag{A.1}$$

where, noting the sequence of heat additions and rejections we have

$$\eta_{Hybrid} = 1 - \frac{q_{1\rightarrow 5}}{q_{2\rightarrow 3} + q_{3\rightarrow 4}} \tag{A.2}$$

where $q_{2\rightarrow 3}$, $q_{3\rightarrow 4}$ and $q_{1\rightarrow 5}$ are composed of internally reversible isobaric, isothermal and isobaric processes respectively. Thus, we arrive at

$$\eta_{Hybrid} = 1 - \frac{C_p \Delta T_{1\rightarrow 5}}{C_p \Delta T_{2\rightarrow 3} + T_3 \Delta s_{3\rightarrow 4}} \tag{A.3}$$

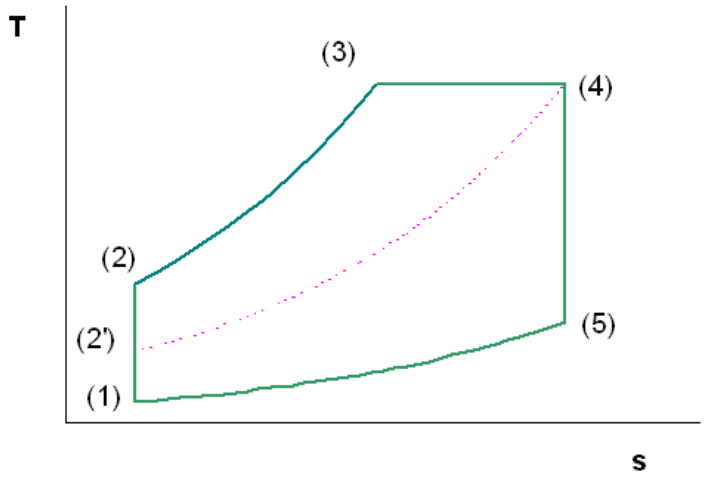

Figure A.1: T-s diagram for hybrid isothermal-Brayton cycle

For the isothermal heat addition process $3 \rightarrow 4$ we note

$$\Delta s_{3\rightarrow 4} = C_p ln(\frac{T_4}{T_3}) - Rln(\frac{P_4}{P_3}) =$$
$$-Rln(\frac{P_4}{P_3}) = -Rln(\frac{P_4/P_5}{P_3/P_5}) = -Rln(\frac{P_{2'}/P_1}{P_3/P_5}) \tag{A.4}$$

where for the isentropic process $1 \rightarrow 2^{'}$ we have $P_{2'}/P_1 = (T_{2'}/T_1)^{\gamma/(\gamma-1)}$. Furthermore, we can rewrite P_3/P_5 via the following

$$\frac{P_3}{P_5} = \frac{P_2}{P_1} = (\frac{T_2}{T_1})^{\gamma/(\gamma-1))} = \tau_c^{\gamma/(\gamma-1)} \tag{A.5}$$

where we are now re-introducing the notation $\tau_{c'} \equiv T_{2'}/T_1$, $\tau_\lambda \equiv T_3/T_1$ and $\tau_c \equiv T_2/T_1$. Hence, the isobar connecting state $2^{'}$ and 4 represent the isobaric heat addition for the equivalent Brayton cycle with peak temperature ratio τ_λ and compressor temperature ratio $\tau_{c'}$ and also serves to define an isothermal cutoff temperature $T_{4'}$. Combining the previous developments gives

$$\Delta s_{3\rightarrow 4} = -Rln((T_{2'}/T_1)/\tau_c)^{\gamma/(\gamma-1)} = -Rln(\frac{\tau_{c'}}{\tau_c})^{\gamma/(\gamma-1)} \tag{A.6}$$

Making substitutions and dividing by C_p yields

$$\eta_{Hybrid} = 1 - \frac{\Delta T_{1\rightarrow 5}}{\Delta T_{2\rightarrow 3} - \frac{RT_3}{C_p} ln(\frac{\tau_{c'}}{\tau_c})^{\gamma/(\gamma-1)}} =$$

$$1 - \frac{T_5 - T_1}{(T_3 - T_2) - \frac{RT_3}{C_p} ln(\frac{\tau_{c'}}{\tau_c})^{\gamma/(\gamma-1)}} \tag{A.7}$$

which can be almost completely expressed in terms of temperature ratios already defined

$$\begin{aligned} \eta_{Hybrid} &= 1 - \frac{\frac{T_5}{T_1} - 1}{\frac{T_3}{T_1} - \frac{T_2}{T_1} - \tau_\lambda \frac{\gamma-1}{\gamma} ln(\tau_c'/\tau_c)^{\gamma/(\gamma-1)}} \\ &= 1 - \frac{\frac{T_5}{T_1} - 1}{\tau_\lambda - \tau_c - \tau_\lambda ln(\tau_{c'}/\tau_c)} \end{aligned} \tag{A.8}$$

Finally, the temperature ratio T_5/T_1 can be found via the observation that $\Delta s_{1\to5} = \Delta s_{2\to4}$ which gives (noting that the two paths $1 \to 5$ and $2^{'} \to 4$ are isobaric)

$$C_p ln(\frac{T_5}{T_1}) = C_p ln(\frac{T_4}{T_{2'}}) \Rightarrow \frac{T_5}{T_1} = \frac{T_4}{T_{2'}} = \frac{T_4/T_1}{T_{2'}/T_1} = \frac{\tau_\lambda}{\tau_{c'}} \tag{A.9}$$

This yields our final general expression for the Hybrid cycle efficiency

$$\eta_{Hybrid} = 1 - \frac{\tau_\lambda/\tau_{c'} - 1}{\tau_\lambda - \tau_c - \tau_\lambda ln(\tau_{c'}/\tau_c)} \tag{A.10}$$

Note in the limit as $\tau_c \to \tau_{c'}$ we recover the cycle efficiency for the ideal Brayton cycle.

$$\begin{aligned} \eta_{Hybrid} &= 1 - \frac{{\tau_{c'}}^{-1}(\tau_\lambda - \tau_{c'})}{\tau_\lambda - \tau_c - \tau_\lambda ln(\tau_{c'}/\tau_c)} \overset{\tau_c \to \tau_{c'}}{=} \\ 1 &- \frac{\tau_c^{-1}(\tau_\lambda - \tau_c)}{\tau_\lambda - \tau_c} = 1 - {\tau_c}^{-1} = \eta_{Brayton} \end{aligned} \tag{A.11}$$

Likewise, in the limit as $\tau_c \to \tau_\lambda$ our combined cycle efficiency reduces to that of the isothermal cycle

$$\begin{aligned} \eta_{Hybrid} &= 1 - \frac{\frac{\tau_\lambda}{\tau_{c'}} - 1}{\tau_\lambda - \tau_c - \tau_\lambda ln(\tau_{c'}/\tau_c)} \\ \overset{\tau_c \to \tau_\lambda}{=} 1 &- \frac{\tau_\lambda({\tau_{c'}}^{-1} - \tau_\lambda^{-1})}{-\tau_\lambda ln(\tau_{c'}/\tau_\lambda)} = 1 - \frac{({\tau_c}^{-1} - \tau_\lambda^{-1})}{ln(\tau_\lambda/\tau_{c)}} = \eta_{Isothermal} \end{aligned} \tag{A.12}$$

where τ_c is equivalent to $\tau_{c'}$. As in the case of the ideal Brayton and Isothermal cycle a normalized work can also be calculated.

$$W^*_{Hybrid} \equiv \frac{w_{Hybrid}}{C_p T_1} = \frac{q_{2\to 3} + q_{3\to 4} - q_{5\to 1}}{C_p T_1} = \frac{C_p(T_3 - T_2) + T_3 \Delta s_{3\to 4} - C_p(T_5 - T_1)}{C_p T_1} \tag{A.13}$$

Using the previous expression for $\Delta s_{3\to 4}$ (A.4) and substituting our previously defined temperature ratios we find

$$W^*_{Hybrid} = \frac{T_3}{T_1} - \frac{T_2}{T_1} - \frac{T_3}{T_1} ln\frac{\tau_{c'}}{\tau_c} - \frac{T_5}{T_1} + 1 = 1 + \tau_\lambda - \tau_c - \tau_\lambda ln\frac{\tau_{c'}}{\tau_c} - \frac{\tau_\lambda}{\tau_{c'}} \tag{A.14}$$

or

$$W^*_{Hybrid} = 1 - \tau_c + \tau_\lambda(1 - 1/\tau_{c'} - ln\frac{\tau_{c'}}{\tau_c}) \tag{A.15}$$

Taking the limit as $\tau_c \to \tau_\lambda$ we find

$$W^*_{Hybrid} \overset{\tau_c \to \tau_\lambda}{=} 1 - \tau_c + \tau_\lambda(1 - {\tau_{c'}}^{-1} - ln\frac{\tau_{c'}}{\tau_\lambda}) = 1 - \frac{\tau_\lambda}{\tau_{c'}} - \tau_\lambda ln\frac{\tau_{c'}}{\tau_\lambda} = W^*_{Isothermal} \tag{A.16}$$

as expected. And taking the limit as $\tau_c \to \tau_c^{'}$ we also find that

$$W^{Norm}_{Hybrid} \overset{\tau_c \to \tau_{c'}}{=} 1 - \tau_c + \tau_\lambda - \frac{\tau_\lambda}{\tau_c} = W^*_{Brayton}$$

Appendix B

DIFFUSION VIA THE CHAPMAN-ENSKOG CORR.

The coefficient estimates to be used for $D_{i,j}$ in equation (4.5) are not readily available in tabular form for Oxygen or Nitrogen. However, data does exist for using the Chapman-Enskog correlation (derived via psuedo emperical methods) and consists of the following relationship.

$$D_{i,j} = 0.0266 \frac{T^{3/2}}{PMW_{i,j}^{1/2} \sigma_{i,j}^2 \Omega_D} \tag{B.1}$$

where

$$\sigma_{i,j} \equiv \frac{\sigma_i + \sigma_j}{2} \tag{B.2}$$

$$MW_{i,j} \equiv 2(MW_i^{-1} + MW_j^{-1})^{-1} \tag{B.3}$$

$$\Omega_D \equiv \frac{1.06}{T^{*0.156}} + \frac{0.193}{e^{0.45T^*}} + \frac{1.03}{e^{1.52T^*}} + \frac{1.76}{e^{3.89T^*}} \tag{B.4}$$

$$T* \equiv \frac{T}{((\epsilon_i/k_B)(\epsilon_j/k_B))^{1/2}} \tag{B.5}$$

where ϵ_i, ϵ_j, σ_i and σ_j are constants. The required physical constants are given in Table B.1 [1] along with intermediate and final calculated values relevant to $D_{i,j}$.

[1] Svehla, R.A., "Estimated viscosities and thermal conductivities of gases at high temperatures.", 4th Ed., McGraw-Hill, New York, 1987

Table B.1: Required data for calculation of binary diffusion coefficients $D_{i,j}$

Species i	species j	ϵ_i/k_B	ϵ_j/k_B	σ_i	σ_j	MW_i	MW_j	$D_{i,j}(10^{-5})$ (m^2/s)
O_2	Air	106.7	78.6	3.4	3.71	32.0	28.9	1.74
N_2	Air	71.4	78.6	3.79	3.71	28.0	28.9	1.70

Appendix C

CYCLE COMPARISONS

C.1 CONSTANT OVERALL PRESSURE RATIO

In order to utilize the results derived from the flow simulation for the purpose of comparing the isothermal to the Brayton cycle work output, etc., we proceed as follows. Restating the Brayton, combined Hybrid and an intermediate (non-isothermal) cycle as displayed in the Figure C.1 a comparison can be made between the Hybrid cycle operating over the closed path $1 \rightarrow 2 \rightarrow 3' \rightarrow 3 \rightarrow 4 \rightarrow 1$, the equivalent Brayton cycle $1 \rightarrow 2 \rightarrow 3' \rightarrow 3'' \rightarrow 4'' \rightarrow 1$ and an intermediate cycle $1 \rightarrow 2 \rightarrow 3' \rightarrow 3''' \rightarrow 4''' \rightarrow 1$. Note that the processes $1 \rightarrow 2$, $3'' \rightarrow 4''$, $3 \rightarrow 4$ and $3''' \rightarrow 4'''$ are assumed isentropic (i.e. reversible and adiabatic). Also, computational data exists for the paths $3' \rightarrow 3$, $3' \rightarrow 3'''$ and $3' \rightarrow 3''$ (corresponding to the combustion and non-combustion cases respectively). To compare cycle output and thermal efficiency we first characterize the Brayton cycle turbine work as the sum of the subprocess works for the turbine. Or

$$w_{turbine}^{Brayton} = w_{3' \rightarrow 3''} + w_{3'' \rightarrow 4''} = \frac{F_y |\vec{V}_{blade}|}{\dot{m}} + w_{3'' \rightarrow 4''}^{reversible} \tag{C.1}$$

where the first quantity on the right is calculated via simulation data and the last term is simply reversible boundary work for an assumed (internally) reversible expansion process $3'' \rightarrow 4''$. Likewise an expression for the turbine work for the Hybrid cycle is given by

$$w_{turbine}^{Hybrid} = w_{3' \rightarrow 3} + w_{3 \rightarrow 4} = \frac{F_y |\vec{V}_{blade}|}{\dot{m}} + w_{3 \rightarrow 4}^{reversible} \tag{C.2}$$

Also the expression for the intermediate injection case yields an expression for specific turbine work

$$w_{turbine}^{Intermediate} = w_{3' \rightarrow 3'''} + w_{3''' \rightarrow 4'''} = \frac{F_y |\vec{V}_{blade}|}{\dot{m}} + w_{3''' \rightarrow 4'''}^{reversible} \tag{C.3}$$

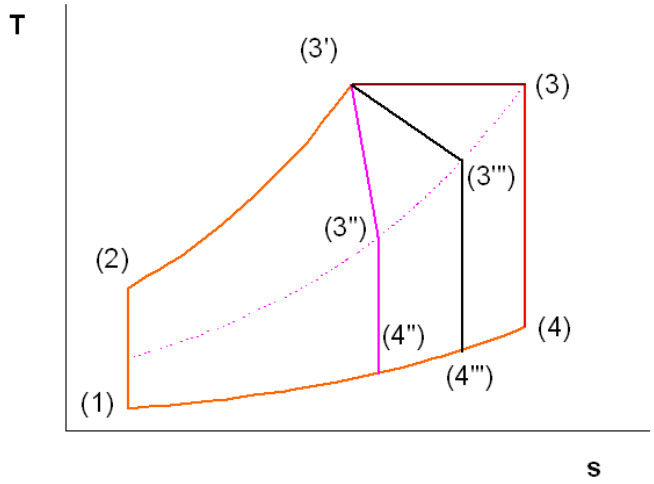

Figure C.1: T-s diagram for Hybrid/nonisothermal/Brayton cycle comparison

Next, an expression for reversible adiabatic boundary work is arrived at via the following development. For an open system undergoing an internally reversible process we have the following differential expressions for the energy and entropy balances (both on a per unit mass)

$$\delta q_{reversible} + \delta w_{reversible} = dh_0 \tag{C.4}$$

$$ds = \frac{\delta q}{T} + \delta s_{irr.} = \frac{\delta q}{T} \tag{C.5}$$

Combining these two expressions we have the following relationship

$$\delta w_{reversible} = dh_0 \tag{C.6}$$

Thus, the reversible adiabatic work can be expressed as

$$w_{reversible} = \Delta h_0 \simeq C_P^{average} \Delta T_0 \tag{C.7}$$

If we assume low Mach numbers (i.e. $T_0 \simeq T$) then the resulting expressions for total specific turbine work for the intermediate, isothermal and Brayton cycle are

$$w_{turbine}^{Brayton} \simeq \frac{F_y |\vec{V}_{blade}|}{\dot{m}} + C_P^{average}(T_{3''} - T_{4''}) \tag{C.8}$$

$$w_{turbine}^{Hybrid} \simeq \frac{F_y |\vec{V}_{blade}|}{\dot{m}} + C_P^{average}(T_3 - T_4) \tag{C.9}$$

$$w_{turbine}^{Intermediate} \simeq \frac{F_y|\vec{V}_{blade}|}{\dot{m}} + C_P^{average}(T_{3'''} - T_{4'''}) \tag{C.10}$$

ΔT for an isentropic process can be calculated by noting the following relationship between temperature and pressure (total or local) assuming constant specific heats

$$(\frac{T_2}{T_1})_{isentropic} = (\frac{P_2}{P_1})^{(\overline{\gamma}-1)/\overline{\gamma}} \tag{C.11}$$

where $\overline{\gamma}$ is some suitably chosen average value over the process.

In addition, to specific work we may also be interested in comparing thermal efficiency. We can begin by noting the definition of cycle efficiency where net work is the difference between turbine and compressor work (for, say a turboshaft engine)

$$\eta \equiv \frac{w_{net}}{q_{in}} = \frac{w_{turb} - w_{comp}}{q_{in}} \tag{C.12}$$

Or more specifically,

$$\eta_{Brayton} = \frac{w_{turb} - w_{comp}}{q_{in}} = \frac{w_{turb} - w_{comp}}{q_{2\to 3'}} \tag{C.13}$$

$$\eta_{Hybrid} = \frac{w_{turb} - w_{comp}}{q_{in}} = \frac{w_{turb} - w_{comp}}{q_{2\to 3'} + q_{3'\to 3}} \tag{C.14}$$

$$\eta_{Intermediate} = \frac{w_{turb} - w_{comp}}{q_{in}} = \frac{w_{turb} - w_{comp}}{q_{2\to 3'} + q_{3'\to 3'''}} \tag{C.15}$$

where

$$q_{2\to 3'} = \Delta h_{0(2\to 3')} \simeq \Delta h_{(2\to 3')} = \int_{T_2}^{T_{3'}} C_p(T)dT \tag{C.16}$$

Note that C_p in the preceding cycle analysis can be approximated by that of air (the combustion process results in a change in specific heat due to changes in chemical composition, but we choose to neglect this).[1] Specific heat (for air) as a function of temperature is given by

$$C_P(T) = 0.96 + 6.7(10^{-5})T + 1.65(10^{-7})T^2 - 6.75(10^{-11})T^3 \tag{C.17}$$

where the units are $(kJ/kg -^\circ K)$. Thus

$$q_{2\to 3'} \simeq \int_{T_2}^{T_{3'}} C_p(T)dT \simeq$$

$$0.96T\Big|_{T_{3'}}^{T_2} + 3.3(10^{-5})T^2\Big|_{T_{3'}}^{T_2} + 0.55(10^{-7})T^3\Big|_{T_{3'}}^{T_2} - 1.68(10^{-11})T^4\Big|_{T_{3'}}^{T_2} \tag{C.18}$$

[1] As a check the simulation mixture specific heat and calculated specific heat for air were compared and had the values 1.29 and $1.21(kJ/kg -^\circ K)$. Thus, with an error of about 6% we are justified in approximating the mixture by a single component fluid (air).

Now, the heat addition for the isothermal process $3^{'} \rightarrow 3$ can be approximated by using the upper heating value HHV for Kerosene.[2] Hence,

$$q_{3' \rightarrow 3} = \frac{\dot{m}_{fuel}}{\dot{m}} HHV \tag{C.19}$$

Finally, the compressor work can be estimated via the previous reversible work expression

$$w_{reversible} \simeq C_P^{average}(T_{0,2} - T_{0.1}) \tag{C.20}$$

or assuming low compressor inlet and outlet Mach numbers

$$w_{reversible} \simeq C_P^{average}(T_2 - T_1) \tag{C.21}$$

where the inlet pressure and temperature are that of the ambient ($10^5 MPa$ and $300^\circ K$).

Now, for computational purposes, quantities of interest to us are γ and hence C_p evaluated at T_1, T_2, $T_{3''}$, $T_{4''}$, $T_{3'''}$, $T_{4'''}$ and T_4, thus let us assume values for the previous temperatures and iterate the solutions as needed (see Table C.1 for all assumed relevant state temperatures).

Table C.1: Assumed state temperatures, C_p and γ

State	T	C_P	γ
1	300	0.99	1.40
2	800	1.08	1.35
4	800	1.08	1.35
$4^{''}$	800	1.08	1.35
$4^{'''}$	800	1.08	1.35

Thus, we can assign an average value for specific heat and γ over the required processes (see Table C.2 for all assumed path averaged relevant properties).

Table C.2: Assumed process averaged C_p and γ

Process	$\overline{C_P}$	$\overline{\gamma}$
$1 \rightarrow 2$	1.04	1.38

[2] Again we are assuming vapor injection (as opposed to droplet) where the upper heating value for Dodecane was used which is $47,841 (kJ/kg_{fuel})$.

Note that for certain states (namely) 3, $3^{'}$ $3^{''}$ and $3^{'''}$ we have simulated data for specific heat and γ. This information is presented in Table C.3.

Table C.3: Simulation C_p and γ

State	C_P	γ
3	1.31	1.28
$3^{'}$	1.30	1.29
$3^{''}$	1.31	1.28
$3^{'''}$	1.30	1.29

Thus, as in the previous case we can calculate an average value for specific heat and γ for relevant the processes $3 \rightarrow 4$, $3^{''} \rightarrow 4^{''}$ and $3^{'''} \rightarrow 4^{'''}$(given in Table C.4).

Table C.4: Assumed process averaged specific heats and γ

Process	$\overline{C_P}$	$\overline{\gamma}$
$3 \rightarrow 4$	1.19	1.32
$3^{''} \rightarrow 4^{''}$	1.20	1.32
$3^{'''} \rightarrow 4^{'''}$	1.19	1.32

For reversible adiabatic compression $1 \rightarrow 2$ we have

$$T_2 = T_1(\frac{P_2}{P_1})^{(\overline{\gamma}-1)/\overline{\gamma}} = 300(34.6)^{0.38/1.38} = 796.0^{\circ}K \tag{C.22}$$

(which is very close to our initial guess of $800^{\circ}K$). Thus, the compressor work via C.21 is given by

$$w_{compressor} \simeq C_P(T_2 - T_1) = 1.04(796 - 300) = 515.8(kJ/kg) \tag{C.23}$$

Next we determine the heat addition in the combustor (process $2 \rightarrow 3^{'}$), via (C.18) which gives a value for $q_{2 \rightarrow 3'}$ of $1,046.8(kJ/kg)$. In addition, we also have [3]

$$q_{3' \rightarrow 3} = \frac{\dot{m}_{fuel}}{\dot{m}} HHV = \frac{0.173}{56.3}(47,841) = 147.0(kJ/kg) \tag{C.24}$$

and

$$q_{3' \rightarrow 3'''} = \frac{\dot{m}_{fuel}}{\dot{m}} HHV = \frac{0.091}{56.89}(47,841) = 58.8(kJ/kg) \tag{C.25}$$

[3]The flow rates were selected from the mid-rotor injection simulaton

Finally, we must determine the turbine exit temperature for the simulated Brayton, Hybrid and Intermediate cycle via C.11 which gives

$$(\frac{T_{4''}}{T_{3''}}) = (\frac{P_{4''}}{P_{3''}})^{(\overline{\gamma}-1)/\overline{\gamma}} \Rightarrow T_{4''}^{Brayton} = 1,597.5(0.04)^{0.32/1.32} = 732.1^{\circ}K \quad \text{(C.26)}$$

$$(\frac{T_4}{T_3}) = (\frac{P_4}{P_3})^{(\overline{\gamma}-1)/\overline{\gamma}} \Rightarrow T_4^{Hybrid} = 1,690.7(0.04)^{0.32/1.32} = 774.7^{\circ}K \quad \text{(C.27)}$$

$$(\frac{T_{4'''}}{T_{3'''}}) = (\frac{P_{4'''}}{P_{3'''}})^{(\overline{\gamma}-1)/\overline{\gamma}} \Rightarrow T_{4'''}^{Intermediate} = 1,645.9(0.04)^{0.32/1.32} = 754.2.1^{\circ}K \quad \text{(C.28)}$$

Note that these results are close to the assumed values in Table C.1. Thus, from these results and utilizing (C.8), (C.9) and (C.10) we have the following

$$w_{turbine}^{Brayton} \simeq \frac{23.8(275)}{57.27} + 1.2(1,597.5 - 732.1) = 1152.7(kJ/kg) \quad \text{(C.29)}$$

$$w_{turbine}^{Hybrid} \simeq \frac{23.9(275)}{56.15} + 1.19(1,690.7 - 774.7) = 1207.1(kJ/kg) \quad \text{(C.30)}$$

$$w_{turbine}^{Intermediate} \simeq \frac{23.9(275)}{56.89} + 1.19(1,645.9 - 754.23) = 1176.6(kJ/kg) \quad \text{(C.31)}$$

Finally, using the general expression for thermal efficiency we have

$$\eta_{Brayton} = \frac{w_{turb} - w_{comp}}{q_{in}} = \frac{w_{turb} - w_{comp}}{q_{2\rightarrow 3'}} = \frac{1152.7 - 515.8}{1,046.8} = 0.607 \quad \text{(C.32)}$$

$$\eta_{Hybrid} = \frac{w_{turb} - w_{comp}}{q_{in}} = \frac{w_{turb} - w_{comp}}{q_{2\rightarrow 3'} + q_{3'\rightarrow 3}} = \frac{1207.1 - 515.8}{1,046.8 + 147.0} = 0.579 \quad (C.33)$$

$$\eta_{Intermediate} = \frac{w_{turb} - w_{comp}}{q_{in}} = \frac{w_{turb} - w_{comp}}{q_{2\rightarrow 3'} + q_{3'\rightarrow 3'''}} = \frac{1176.6 - 515.8}{1,046.8 + 76.5} = 0.588 \quad (C.34)$$

C.2 NON-CONSTANT PRESSURE RATIO

Simulation date exists for the paths $3' \rightarrow 3$ and $3 \rightarrow 4'$ in the form a high inlet pressure simulation with an exit pressure and temperature comforming to that of state 3, and the non-combustion simulations with an inlet state 3.[4] Note that all quantities relevant to

[4]See Appendix E for inlet and exit states.

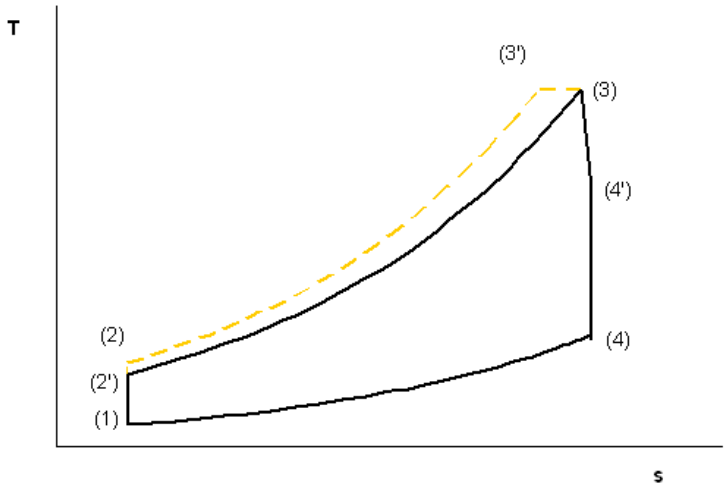

Figure C.2: T-s diagram for hybrid and Brayton cycle for equal peak temperatures and isothermal cutoff/turbine inlet pressures

process $4' \rightarrow 4$, $1 \rightarrow 2'$ and $4 \rightarrow 1$ have previously been calculated. Hence, the only remaining quantities to calculate are $w_{1\rightarrow 2}$, $q_{2\rightarrow 3'}$, $q_{3'\rightarrow 3}$ and $w_{3'\rightarrow 3}$. Specifically, assuming identical average process values for specific heat, etc. for $1 \rightarrow 2$ we have

$$T_2 = T_1(\frac{P_2}{P_1})^{(\overline{\gamma}-1)/\overline{\gamma}} = 300(46.57)^{0.38/1.38} = 864^\circ K \tag{C.35}$$

$$w_{compressor} \simeq C_P(T_2 - T_1) = 1.04(864 - 300) = 586(kJ/kg) \tag{C.36}$$

Using the integrated expression for heat addition C.18 we find a value of $972.2(kJ/kg)$ for $q_{2\rightarrow 3}$. The heat addition $q_{3'\rightarrow 3}$ is also given by

$$q_{3'\rightarrow 3} = \frac{\dot{m}_{fuel}}{\dot{m}} HHV = 47,841 \frac{0.201}{72.1} = 133.3(kJ/kg) \tag{C.37}$$

Hence, combining simulation date with the assumed isentropic expansion process $4 \rightarrow 5$ we have the expression for turbine specific work for the high pressure Hybrid case

$$w_{Turbine}^{HP-Hybrid} \simeq (\frac{F_y|\vec{V}_{blade}|}{\dot{m}})_{3'\rightarrow 3} + (\frac{F_y|\vec{V}_{blade}|}{\dot{m}})_{3\rightarrow 4'} + C_P^{average}(T_4' - T_4)$$
$$= 1,260(kJ/kg) \tag{C.38}$$

or in terms of net work

$$w_{net}^{HP-Hybrid} \simeq w_{Turbine} - w_{Comp.} = 674(kJ/kg) \tag{C.39}$$

The efficiency for the high pressrue Hybrid cycle is given by

$$\eta_{HP-Hybrid} = \frac{w_{net}}{q_{in}} = \frac{w_{net}}{q_{2\to 3'} + q_{3'\to 3}} = \frac{674}{972.2 + 133.3} = 0.6090.61 \tag{C.40}$$

Thus, the high pressure hybird cycle has an efficiency (based on *pseudo* simulation data) of 61% and specific net work of 674(kJ/kg).

Appendix D

PATTERN FACTORS

Of interest to us is the extent to which the flow is non-uniform in temperature just downstream of combustion. Indeed, for the case of rotor injection, an accompanying foil, such as a stator blade may reside just downstream. Thus, we define two *pattern factors* as

$$PF \equiv \frac{T_{max} - T_{mean}}{\Delta T_{stage}} \tag{D.1}$$

$$\overline{PF} \equiv \frac{T_{max} - T_{min}}{\Delta T_{stage}} \tag{D.2}$$

where ΔT_{stage} is the temperature change for the non-injection case.[1]

Table D.1: Required data for calculation of pattern factor (laminar rotor injection)

Injection location	$T^{\circ}_{max}K$	$T^{\circ}_{min}K$	$T^{\circ}_{mean}K$	$\Delta T^{\circ}_{stage}K$
No Injection	$1,601$	$1,594$	$1,597$	66
LEPS Injection	1.713	$1,672$	$1,690$	66
Mid Injection	$1,719$	$1,678$	$1,692$	66
LESS Injection	$1,711$	$1,681$	$1,694$	66

The chosen distance from the trailing edge (in the meridonial direction) is approximately one quarter of a cord length. The required quantites are given in Table D.1.[2]

[1] Note that a pattern factor for a turbine is traditionally defined where ΔT is over a stage, but in our case change in local temperature is (ideally) zero given that our aim is to achieve isothermal combustion. Hence, we use the non-combustion stage temperature drop to normalize the non-uniformity in flow temperature.

[2] Note that the average temperature used for T_{mean} was not the profile mean, but the stage outlet mean

Finally, the calculated pattern factors are given in Table D.2

Table D.2: Calculated pattern factors (laminar rotor injection)

Injection location	PF	$\overline{PF}$
No Injection	0.05	0.10
LEPS Injection	0.34	0.61
Mid Injection	0.40	0.61
LESS Injection	0.24	0.44

Similarly, we have the required data for the stator injection cases.

Table D.3: Required date for calculation of pattern factor (laminar stator injection)

Injection location	$T^{\circ}_{max}K$	$T^{\circ}_{min}K$	$T^{\circ}_{mean}K$	$\Delta T^{\circ}_{stage}K$
No Injection	$1,669$	$1,659$	$1,664$	35.0
LESS Injection	$1,812$	$1,730$	$1,762$	35.0
LEPS Injection	$1,808$	$1,722$	$1,764$	35.0
LESS Injection	$1,898$	$1,898$	$1,1770$	35.0
LEPS Injection	$1,870$	$1,870$	$1,760$	35.0

Table D.4: Calculated pattern factors (laminar stator adiabatic wall injection)

Injection location	PF	$\overline{PF}$
non injection	0.142	0.285
less	1.42	2.43
leps	1.25	2.45
tess	3.65	5.51
teps	3.14	4.42

flow temperature. Given that no turning or work extraction is present after the flow proceeds downstream of the rotor, average local temperature should remain essentually constant.

Appendix E

BOUNDARY CONDITIONS

The boundary conditions for all simulations are provided in Table E.1

Table E.1: Simulation boundary conditions

Quantity	Boundary value
P^0_{inlet}	3.5 MPa (4.4 MPa for high pressure case)
P_{outlet}	2.5 MPa (3.5 MPa for high pressure case)
T^0_{inlet}	$1,700° K$
T_{outlet} (backflow only)	$1,700° K$
$T_{injection}$	$600° K$
Tu_{inlet}	5 %
Tu_{outlet} (backflow only)	5 %
$Tu_{injection}$	10 %
$H_{D(injection)}$	0.001 (m)
$H_{D(inlet)}$	0.1 (m)
$H_{D(outlet)}$	0.1 (m)
$T_{surface}$ (non-addiabatic surface)	$1,000° K$
$\dot{m}_{fuel}$	variable (0.175(kg/s) target), (injection normal to boundary)
V_y rotor blade	275 m/s
$\chi^{fuel}_{injection}$	1
$\chi^{N_2}_{inlet}$	0.771
$\chi^{O_2}_{inlet}$	0.122
$\chi^{H_2O}_{inlet}$	0.031
$\chi^{CO_2}_{inlet}$	0.076

Appendix F

SIMULATION DATA

F.1 BULK FLOW QUANTITIES

F.1.1 ROTOR INJECTION

Table F.1: Inlet and exit flow properties for reacting flow case (rotor less injection)

Sim. type	$\rho_{inlet}(m^3)$	$\rho_{outlet}(m^3)$	P_{inlet}(MPa)	P_{outlet}(MPa)	$T^{\circ}_{inlet}K$	$T^{\circ}_{outlet}K$	$\dot{m_{in}}$ (kg/m)
Unst.-ad LAM.	7.27	5.29	3.46	2.50	1,696	1,694	56.1
Unst.-ad ED.	7.27	5.28	3.46	2.50	1,696	1,701	56.0
Unst.-ad PDF.	6.10	5.81	3.45	2.50	1,700	1,791	60.6
Unst.-nonad.LAM	7.27	5.41	3.46	2.50	1,696	1,660	56.4
Unst.-nonad.ED	7.27	5.39	3.46	2.50	1,696	1,653	56.3
Unst.-nonad. PDF	6.10	5.96	3.45	2.50	1,700	1,742	61.2

Table F.2: Inlet and exit flow properties for reacting flow case (rotor mid injection)

Sim. type	$\rho_{inlet}(m^3)$	$\rho_{outlet}(m^3)$	P_{inlet}(MPa)	P_{outlet}(MPa)	$T^{\circ}_{inlet}K$	$T^{\circ}_{outlet}K$	$\dot{m_{in}}$ (kg/m)
Unst.-ad LAM.	7.27	5.31	3.46	2.50	1,696	1,692	56.3
Unst.-ad ED.	7.27	5.32	3.46	2.50	1,696	1,690	56.0
Unst.-ad PDF.	6.10	5.77	3.45	2.50	1,700	1,805	60.2
Unst.-nonad.LAM	7.27	5.42	3.46	2.50	1,696	1,658	56.7
Unst.-nonad.ED	7.27	5.43	3.46	2.50	1,696	1,652	56.4
Unst.-nonad. PDF	6.10	5.90	3.45	2.50	1,700	1,766	60.7

Table F.3: Inlet and exit flow properties for reacting flow case (rotor leps injection)

Sim. type	$\rho_{inlet}(m^3)$	$\rho_{outlet}(m^3)$	P_{inlet}(MPa)	P_{outlet}(MPa)	$T^{\circ}_{inlet}K$	$T^{\circ}_{outlet}K$	$\dot{m_{in}}$ (kg/m)
Unst.-ad LAM.	7.27	5.32	3.46	2.50	1,696	1,690	56.1
Unst.-ad ED.	7.27	5.30	3.46	2.50	1,695	1,690	56.1
Unst.-ad PDF.	6.10	5.77	3.45	2.50	1,700	1,800	60.3
Unst.-nonad.LAM	7.27	5.43	3.46	2.50	1,696	1,656	56.4
Unst.-nonad.ED	7.27	5.46	3.46	2.50	1,696	1,663	56.5
Unst.-nonad. PDF	6.10	5.91	3.45	2.50	1,700	1,761	60.8

F.2 STATOR INJECTION

Table F.4: Inlet and exit flow properties for reacting flow case (stator less injection)

Sim. type	$\rho_{inlet}(m^3)$	$\rho_{outlet}(m^3)$	P_{inlet}(MPa)	P_{outlet}(MPa)	$T^{\circ}_{inlet}K$	$T^{\circ}_{outlet}K$	$\dot{m_{in}}$ (kg/m)
Unst.-ad LAM.	7.27	5.30	3.46	2.50	1,696	1,695	55.0
Unst.-ad ED.	7.27	5.30	3.46	2.50	1,696	1,694	55.1
Unst.-ad PDF.	6.10	5.88	3.45	2.50	1,700	1,760	60.6
Unst.-nonad.LAM	7.27	5.41	3.46	2.50	1,696	1,663	55.4
Unst.-nonad.ED	7.27	5.41	3.46	2.50	1,696	1,662	55.5
Unst.-nonad. PDF	6.10	5.93	3.45	2.50	1,700	1,742	58.4

Table F.5: Inlet and exit flow properties for reacting flow case (stator leps injection)

Sim. type	$\rho_{inlet}(m^3)$	$\rho_{outlet}(m^3)$	P_{inlet}(MPa)	P_{outlet}(MPa)	$T^{\circ}_{inlet}K$	$T^{\circ}_{outlet}K$	$\dot{m_{in}}$ (kg/m)
Unst.-ad LAM.	7.27	5.31	3.46	2.50	1,696	1,693	55.3
Unst.-ad ED.	7.27	5.31	3.46	2.50	1,696	1,693	55.3
Unst.-ad PDF.	6.10	5.78	3.45	2.50	1,700	1,786	58.4
Unst.-nonad.LAM	7.27	5.40	3.46	2.50	1,696	1,662	55.7
Unst.-nonad.ED	7.27	5.41	3.46	2.50	1,696	1,660	56.6
Unst.-nonad. PDF	6.10	5.90	3.45	2.50	1,700	1,734	62.1

Table F.6: Inlet and exit flow properties for reacting flow case (stator tess injection)

Sim. type	$\rho_{inlet}(m^3)$	$\rho_{outlet}(m^3)$	P_{inlet}(MPa)	P_{outlet}(MPa)	$T^{\circ}_{inlet}K$	$T^{\circ}_{outlet}K$	$\dot{m_{in}}$ (kg/m)
Unst.-ad LAM.	7.27	5.30	3.46	2.50	1,696	1,694	55.8
Unst.-ad ED.	7.27	5.35	3.46	2.50	1,696	1,697	56.0
Unst.-ad PDF.	6.10	6.0	3.45	2.50	1,700	1,720	59.9
Unst.-nonad.LAM	7.27	5.36	3.46	2.50	1,696	1,668	56.4
Unst.-nonad.ED	7.27	5.42	3.46	2.50	1,696	1,658	56.1
Unst.-nonad. PDF	6.10	5.87	3.45	2.50	1,700	1,768	61.6

Table F.7: Inlet and exit flow properties for reacting flow case (stator teps injection)

Sim. type	$\rho_{inlet}(m^3)$	$\rho_{outlet}(m^3)$	P_{inlet}(MPa)	P_{outlet}(MPa)	$T^{\circ}_{inlet}K$	$T^{\circ}_{outlet}K$	$\dot{m_{in}}$ (kg/m)
Unst.-ad LAM.	7.27	5.31	3.46	2.50	1,696	1,693	55.3
Unst.-ad ED.	7.27	5.31	3.47	2.50	1,696	1,691	55.7
Unst.-ad PDF.	6.10	5.77	3.45	2.50	1,700	1,798	60.5
Unst.-nonad.LAM	7.27	5.39	3.46	2.50	1,696	1,666	55.6
Unst.-nonad.ED	7.27	5.40	3.46	2.50	1,696	1,666	55.8
Unst.-nonad. PDF	6.10	5.90	3.45	2.50	1,700	1,759	60.8

F.3 OTHER QUANTITIES OF INTEREST

F.3.1 ROTOR

Table F.8: Injection rates, peak temperatures, etc (rotor less injection)

Sim. type	$\Delta\chi_{CO_2}$	$\dot{m}_{fuel}$	$T_{peak}\ ^\circ K$
Unst.-ad LAM.	0.0101	0.176	2,698
Unst.-ad ED.	0.0106	0.184	2,726
Unst.-ad PDF.	0.0065	0.122	1,994
Unst.-nonad.LAM	0.0101	0.177	–
Unst.-nonad.ED	0.0105	0.183	–
Unst.-nonad. PDF	0.0065	0.123	–

Table F.9: Injection rates, peak temperatures, etc (rotor mid injection)

Sim. type	$\Delta\chi_{CO_2}$	$\dot{m}_{fuel}$	$T_{peak}\ ^\circ K$
Unst.-ad LAM.	0.099	0.173	2,692
Unst.-ad ED.	0.0099	0.171	2,704
Unst.-ad PDF.	0.0077	0.144	2,013
Unst.-nonad.LAM	0.0082	0.169	–
Unst.-nonad.ED	0.0095	0.183	–
Unst.-nonad. PDF	0.0074	0.123	–

Table F.10: Injection rates, peak temperatures, etc (rotor leps injection)

Sim. type	$\Delta\chi_{CO_2}$	$\dot{m}_{fuel}$	$T_{peak}\ ^\circ K$
Unst.-ad LAM.	0.099	0.172	2,691
Unst.-ad ED.	0.0105	0.182	2,704
Unst.-ad PDF.	0.0055	0.103	2,013
Unst.-nonad.LAM	0.097	0.171	–
Unst.-nonad.ED	0.0103	0.180	–
Unst.-nonad. PDF	0.0064	0.120	–

F.3.2 STATOR

Table F.11: Injection rates, peak temperatures, etc. (stator less injection)

Sim. type	$\Delta\chi_{CO_2}$	$\dot{m}_{fuel}$	$T_{peak}\ ^{\circ}K$
Unst.-ad LAM.	0.0103	0.175	$2,702$
Unst.-ad ED.	0.0102	0.174	$2,733$
Unst.-ad PDF.	0.0020	0.037	$1,994$
Unst.-nonad.LAM	0.0103	0.176	–
Unst.-nonad.ED	0.0098	0.168	–
Unst.-nonad. PDF	0.005	0.090	–

Table F.12: Injection rates, peak temperatures, etc (stator leps injection)

Sim. type	$\Delta\chi_{CO_2}$	$\dot{m}_{fuel}$	$T_{peak}\ ^{\circ}K$
Unst.-ad LAM.	0.0102	0.174	$2,741$
Unst.-ad ED.	0.0101	0.173	$2,757$
Unst.-ad PDF.	0.0095	0.171	$2,610$
Unst.-nonad.LAM	0.0102	0.176	–
Unst.-nonad.ED	0.0102	0.178	–
Unst.-nonad. PDF	0.007	0.134	–

Table F.13: Injection rates, peak temperatures, etc (stator tess injection)

Sim. type	$\Delta\chi_{CO_2}$	$\dot{m}_{fuel}$	$T_{peak}\ ^{\circ}K$
Unst.-ad LAM.	0.0107	0.185	$2,627$
Unst.-ad ED.	0.0114	0.197	$2,411$
Unst.-ad PDF.	0.0074	0.137	$2,020$
Unst.-nonad.LAM	0.0110	0.192	–
Unst.-nonad.ED	0.0092	0.160	–
Unst.-nonad. PDF	0.0011	0.021	–

Table F.14: Injection rates, peak temperatures, etc (stator teps injection)

Sim. type	$\Delta\chi_{CO_2}$	$\dot{m}_{fuel}$	$T_{peak}\ ^\circ K$
Unst.-ad LAM.	0.0103	0.176	2,722
Unst.-ad ED.	0.0097	0.167	2,720
Unst.-ad PDF.	0.009	0.168	2,061
Unst.-nonad.LAM	0.0105	0.181	–
Unst.-nonad.ED	0.0102	0.176	–
Unst.-nonad. PDF	0.0010	0.02	–

F.4 REDUCED INJECTION RATE CASE

Table F.15: Inlet and exit flow properties for reacting flow case (reduced mid-injection)

Sim. type	$\rho_{inlet}(m^3)$	$\rho_{outlet}(m^3)$	P_{inlet}(MPa)	P_{outlet}(MPa)	$T^\circ_{inlet}K$	$T^\circ_{outlet}K$	$\dot{m}_{in}\ (kg/m)$
Unst.-ad LAM.	7.22	5.46	3.46	2.50	1,696	1,646	55.6
Unst.-nonad LAM.	7.26	5.56	3.46	2.50	1,696	1,615	55.9

Table F.16: Injection rates, peak temperatures, etc (reduced mid-injection)

Sim. type	$\Delta\chi_{CO_2}$	$\dot{m}_{fuel}$
Unst.-ad LAM.	0.0053	0.093
Unst.-onoad LAM.	0.0051	0.090

F.5 INCREASED PRESSURE RATIO CASE

Table F.17: Inlet and exit flow properties for reacting flow case (high pressure mid-injection)

Sim. type	$\rho_{inlet}(m^3)$	$\rho_{outlet}(m^3)$	P_{inlet}(MPa)	P_{outlet}(MPa)	$T^\circ_{inlet}K$	$T^\circ_{outlet}K$	$\dot{m}_{in}\ (kg/m)$
Unst.-ad LAM.	9.69	7.33	4.66	3.50	1,696	1,697.3	72.1

Table F.18: Injection rates, peak temperatures, etc (high pressure mid-injection)

Sim. type	$\Delta\chi_{CO_2}$	$\dot{m}_{fuel}$	F_y kN
Unst.-ad LAM.	0.0920	0.201	27.5

Bibliography

[1] S.P. Lukachko, D.R. Kirk, I.A. Wailt *Turbine Durability Impact of High Fuel-Air Ratio Combustors Part I:Potential for Intra-Turbine Oxidation of Partially Reacted Fuel* ASME-Turbo Expo, GT-2002-30077, 2002

[2] R. Andriani, F. Gamma, U. Ghezzi and E. Infante. *Design Proposals for Constant Temperature Turbine Engine for Propulsion System*, AIAA, 2001

[3] K.N.R. Ramohalli. *Isothermal Combustion for Improved Efficiencies*, AIAA-87-1999, 1987

[4] F. Liu and W.A. Sirignano. *Turbojet and Turbofan Engine Performance Increases Through Turbine Burners* AIAA-2000-0741, 2000, pages 1-25

[5] W.A. Sirignano, J.P. Delplanque and F.Liu. *Selected Challenges in Jet and Rocket Engine Combustion Research*, AIAA-97-2701, 1997, Pages 1-22

[6] S. Nasir, A.K. Agrawal, I. McGregor and L. Tuchinskiy. *Characteristics of Confined Diffusion Flames Stabilization over Porous Plates in a Flow Channel*

[7] A.K. Agrawal and Shakeel Nasir. *Non-catalytic Porous Combustion for Turbine Burner Applications*, ..., 2000

[8] T.A. Rohmat, H. Katoh, T. Obara, T. Yoshihashi and S. Ohyagi. *Diffusion Flame Stabilized on a Porous Plate in a Parallel Airstream* , AIAA Vol. 36, No. 11, Nov. 1998, Pages 1945-55

[9] A. Ramachandra, B.N. Raghunandan *Investigation on the Stability and Extinction of a Laminar Diffusion Flame Over a Porous Flat Plate*

[10] M.G. Owens, S. Tehranian, C. Segal and V.A. Vinogradov. *Flame-Holding Configurations for Kerosene Combustion in a Mach 1.8 Airflow*, Journal of Propulsion and Power, Vol. 14, No. 4, July-August 1998, Pages 456-61

[11] R.W. Schefer, N. Namazian and J. Kelly *Velocity Measurements in a Turbulent Non-premixed Bluff-Body Stabilized Flame*, AIAA-88-0532

[12] J.R. Roy *Bluff-Body Stabilized Flame Calculation with the $\kappa - \zeta$ Two Equation Turbulence Model*, AIAA-98-0252

[13] M.S. Anand, S.B. Pope and H.C. Mongia *PDF Calculations for Swirling Flows*, AIAA-93-0106

[14] C.L. Hackert, J.L. Ellzey, O.A. Ezekoye *Combustion and Heat Transfer in Model Two-Dimensional Porous Burners*, Combustion and Flame 116:177-91, 1999

[15] J. Lee and D. Fricher *A Numerical Study of Reacting flow inside Combustors using a Two-equation model of Turbulence and an Eddy- dissipation model for Turbulent Chemistry*, AIAA, 1997

[16] K. Chen and J. Shuen. *A Coupled Multi-Block Solution Procedure for Spray Combustion in Complex Geometries*, AIAA-93-0108

[17] J.L. Xia, G. Yadigaroglu, Y.S. Liu, J. Schmidli and B.L. Smith *Numerical and Experimental Study of Swirling Flow in a Model Combustor*, Int. J. Heat Mass Transfer Vol41, No.11, Pages 1485-97

[18] J. Zelina, J. Ehret, R.D. Hancak, *Ultra-Compact Combustor Technology Using High Swirl for Enhanced Burning Rate*, AIAA 2002-3725

[19] G.D. Lewis, *Centrifugal-Force Effects on Combustion* 14^{th} Symposium (International) on Combustion, The Combustion Institute, pp.413-19, 1973

[20] Metghalchi and Keck, *Burning Velocities of Mixtures of Air with Methanol, Isooctane and Indolene at High Pressures Temperatures*, Combustion and Flame, 48: 191-210

VITA

Matthew Rice, born in Portland, Oregon to Thomas and Phyllis Rice, received his B.A. in Economics from Reed College. Spending a brief time at Portland State as a physics undergraduate and then at Columbia University, Mr. Rice joined the Virgina Tech community in 2001. His activites during that time included internships at NASA Glenn Research Center and Pratt & Whitney as well as an instructorship at Virginia Tech. After completing an internship at Pratt & Whitney, Mr. Rice plans to begin a Ph.D program at King's College London at the Experimental and Computational Laboratory for the Analysis of Turbulence in the fall of 2004.